**Title**
FOUR-BODY STRANGE PARTICLE PRODUCTION IN pp COLLISIONS AT 6 BeV/c



**Author**
Klein, Stanley Lewis.

**Publication Date**
1968-09-01

UCRL-18306

cy. 2



# University of California

# Ernest O. Lawrence Radiation Laboratory

FOUR-BODY STRANGE PARTICLE PRODUCTION
IN pp COLLISIONS AT 6 BeV/c

Stanley Lewis Klein
(Ph. D. Thesis)

September 1968



Berkeley, California

E, P

UCRL-18306
cy. 2

## DISCLAIMER

UCRL-18306

UNIVERSITY OF CALIFORNIA

Lawrence Radiation Laboratory
Berkeley, California

AEC Contract No. W-7405-eng-48

# FOUR-BODY STRANGE PARTICLE PRODUCTION IN pp COLLISIONS AT 6 BeV/c

Stanley Lewis Klein

Ph. D. Thesis

September 1968

FOUR-BODY STRANGE PARTICLE PRODUCTION IN pp COLLISIONS AT 6 BeV/c

Contents

# FOUR-BODY STRANGE PARTICLE PRODUCTION IN pp COLLISIONS AT 6 BeV/c

Stanley Lewis Klein

Lawrence Radiation Laboratory
University of California
Berkeley, California

## ABSTRACT

An exposure of the LRL 72-in. liquid-hydrogen bubble chamber to 6 BeV/c protons has yielded some 3000 examples of production of strange particles in four-body final states. Cross sections for the reactions $pp \to \Lambda K^{o} p\pi^{+}$, $pp \to \Lambda K^{+} p\pi^{o}$, and $pp \to \Lambda K^{+} n\pi^{+}$ are 64 ± 6 μb, 39 ± 6 μb, and 43 ± 4 μb, respectively. The resonances K*(890), N*(1236), and Y*(1385) are produced with cross sections

$$\sigma(p\Lambda K^{*+}) = 9 \pm 3 \ \mu b$$
$$\sigma(\Lambda K^{o} N^{*++}) = 23 \pm 3 \ \mu b$$
$$\sigma(\Lambda K^{+} N^{*+}) = 4 \pm 2 \ \mu b$$
$$\sigma(pK^{o} Y^{*+}) = 11 \pm 2 \ \mu b$$
$$\sigma(pK^{+} Y^{*o}) = 7 \pm 1 \ \mu b$$
$$\sigma(nK^{+} Y^{*+}) = 15 \pm 2 \ \mu b$$

In addition, the quasi-two-body reaction $pp \to NN^{*}(1950)$, $N^{*} \to Y^{*}K$ is observed. Except for the low $K\pi$ effective mass region, the data are found to be in good agreement with a pion exchange model.

# I. INTRODUCTION

The inelastic proton-proton interaction has been studied most extensively in zero-strangeness reactions.[1-20] Those results indicate that resonance production is dominant and that the reactions can often be interpreted as examples of pseudo-two-body production. Variations of single pion exchange models have been generally successful in interpreting these data. Until recently, the strange particle data have been too sparse for any detailed analysis. The three-body strange particle final states have been investigated and the reported results indicate that pion exchange is probably an important mechanism in their production.[11,21-26] The four-body strange states have been only incompletely or qualitatively studied.[11, 21,23,26] It is interesting, therefore, to examine these states in more detail and determine to what extent the production mechanisms are like those of the non-strange and the strange three-body reactions.

We present results for the reactions

$$pp \rightarrow \Lambda p K^{o} \pi^{+} \quad \text{(a)}$$

$$\Lambda p K^{+} \pi^{o} \quad \text{(b)}$$

$$\Lambda n K^{+} \pi^{+} \quad \text{(c)}$$

We find Y*(1385) resonance production in all three final states and N*(1236) and K*(890) in (a) and (b). A low mass enhancement in the Y*K system is observed in all reactions and has been interpreted as N*(1950) production proceeding via pion exchange. In Section II we discuss the experimental techniques we have employed with emphasis on the difficulties presented by reactions with an unobserved neutral particle. In Section III the method of determining the cross sections is given.

Section IV contains a discussion of the general features of the final states and the method of fitting used to determine resonance cross sections. A more detailed discussion of the properties of the Y*K enhancement is presented. In Section V we examine the agreement of the data with a pion-exchange model and in Section VI a simple test of $SU_3$ is applied to check the consistency of our interpretation of the Y*K enhancement as N*(1950).

## II. Experimental Techniques

### A. Beam

The results presented in this thesis are from the analysis of some 550,000 pictures taken during an exposure of the Alvarez 72" liquid hydrogen bubble chamber to 6 BeV/c protons. These protons were produced in a target 3/8 in. high, 1/4 in. wide, 1/2 in. long oriented at $7^{\circ}$ with respect to the external proton beam of the Bevatron and were transported to the chamber using the arrangement shown in Fig. 1. The focal properties of the beam at the front of the uranium collimator were determined by the "C" and "H" bending magnets and the first quadrupole doublet. The "C" magnet required considerable shimming in order to reduce spatial variation of the field to less than 0.2%. The bending magnets achieved a momentum dispersion of 1 in. per 1% $\Delta P/P$, and the quadrupole yielded vertical and horizontal magnifications of about 0.5 and 1, respectively. A slit, of dimensions 1/2 in. vertically and 1/4 in. horizontally, through the 12 in. thick uranium collimator resulted then in a momentum definition of $\pm$ 0.12%. The other quadrupole doublet was run with both sections defocussing horizontally to produce a more diffuse beam in the chamber. The two "H" magnets after the slit were both needed for proper steerage of the beam through the fringe field into the chamber. In the first running period, during which about half the pictures were taken, a polyethylene target was fixed in position in the beam. This target was valuable in the tuning since elastically scattered protons were easily identified with counters located directly in front of the slit. During the remainder of the run a copper target was fixed at a distance 3/4 in. from the normal external beam position and the beam deflected onto it

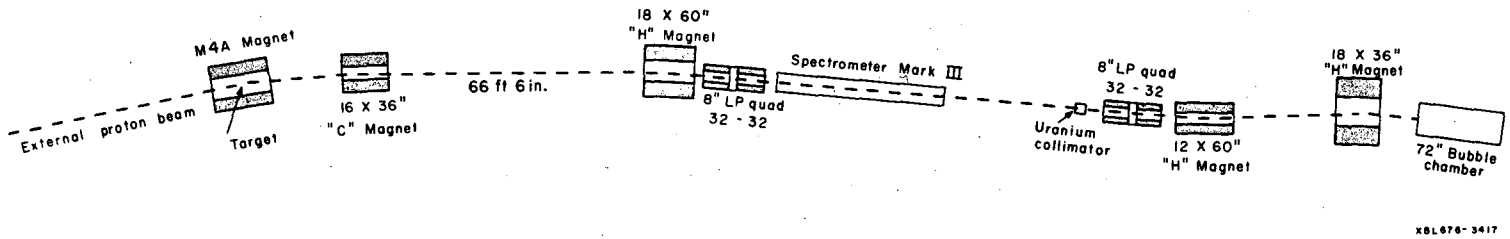


Fig. 1. Schematic of beam transport system.

by a magnet pulsed on for ~ 500 μsec. Thus, independent intensity control was achieved with the remainder of the beam available for other experimenters. Beam intensities of ~ $10^{11}$ protons per pulse and ~ $5\times10^{10}$ protons per pulse were required for the first and second targeting schemes respectively. Although the average number of particles in the main channel varied from 20 to 40 per pulse, the number entering the bubble chamber was held nearly fixed at 11 with a fluctuation of about 2. This stability was obtained with the use of a pulsed parallel plate electromagnetic separator operated with a 4-in. gap and a 150 kV between the plates. When the required number of tracks were registered by counters in front of the chamber, a spark gap in parallel with the plates was discharged in about 2 μsec. The spectrometer's magnetic field then deflected the remaining particles 3/4 in. vertically off the slit into the uranium collimator. Contamination from single pion production is expected to be small and estimated to be less than 0.1%. This value was the result of a measurement made in a similar beam using a Cerenkov counter to distinguish pions from protons. Heavy particle contamination is expected to be even smaller and these contaminations were neglected as a source of background in the analysis.

## B. Scanning and Processing of Events

All of the film was scanned once and approximately three-fourths of it was re-scanned. The only topologies which were used in the analysis were all two-pronged events with either one or two neutral V's visible. All events were measured with either Franckenstein or Vanguard measuring machines and fitted using the PANAL-PACKAGE analysis programs. A small sub-sample of events was also processed with the TVGP-SQUAW system to check for possible biases in the fitting procedure. The identification of events in the two cases was almost invariably the same.

We have chosen to study events which were identified as examples of reactions:

a) $pp \rightarrow \Lambda K^{o} p\pi^{+}$

b) $pp \rightarrow \Lambda K^{+} p\pi^{o}$

c) $pp \rightarrow \Lambda K^{+} n\pi^{+}$

Examples of the reaction $pp \rightarrow \Sigma^{o} K^{o} p\pi^{+}$ were not included in the analysis due to the small number of events and rather serious biases. A fit to either b) or c) was accepted if the $V^{o}$ fitted the 3c $\Lambda$ hypothesis and if the 1c fit for the production hypothesis had a $\chi^{2}$ less than 5.0. For reaction a), events with two visible $V^{o}$ decays were accepted if the corresponding 4c fit to the production hypothesis had a confidence level greater than 1/2%. In all cases, the predicted bubble densities for the two charged tracks at the production vertex were required to be compatible with those observed. Even after repeated remeasurements some events failed to fit any production hypothesis consistent with the observed bubble densities. For approximately half of the film, a

detailed study was carried out to understand these events. For the subset of this sample where unambiguous identification of the tracks was possible, we always found the corresponding missing mass to be in agreement with the production of two neutral particles. For the remaining events, where no unique identification of the charged tracks was possible, we invariably found at least one assignment for the tracks consistent with the observed bubble densities and with the production of two neutrals. Therefore, we have assigned events which failed to fit to the category of two or more unobserved neutrals. Further evidence for the validity of this procedure is given below.

Besides those events with no fits, some were found to be ambiguous between two hypotheses. Except for a negligible number, all ambiguities were between different production hypotheses involving the same observed neutral. Except for ambiguities between the 4c fit $\Lambda K^{o} p\pi^{+}$ and the 2c fit $\Sigma^{o} K^{o} p\pi^{+}$, cases of ambiguity between different constraint classes were assigned to the hypothesis of higher constraint. When the hypothesis of higher constraint was a 4c fit, this procedure was probably correct; however, for those events ambiguous between the 2c fit, $\Sigma^{o} pK^{+}$, and the 1c fit, $\Lambda pK^{+}\pi^{o}$, the chance for misassignment was very much more likely. Fortunately, this type of ambiguity only occurs for the "$\pi^{o}$" final state. In Table I we give the observed number of events for each of the various categories we have discussed.

Before describing the way in which the ambiguous sample was included in the analysis, the obvious kind of correction to the data should be discussed. We find the proper lifetime distributions for both $\Lambda$'s and

Table I. Event totals and cross sections for pp four-body reactions containing a $\Lambda$ at 6 GeV/c

| Category | Observed No. of events | Corrected No. of events [A] | Cross section ($\mu$b) |
|---|---|---|---|
| $\Lambda pK^{o}\pi^{+}$ | 959 | 990 | 64 ± 6 |
| $\Sigma^{o}pK^{o}\pi^{+}$ | 160 | 164 | 11 ± 2 |
| $\Lambda pK^{+}\pi^{o}$ | 492 | 531 | 39 ± 6 |
| $\Lambda nK^{+}\pi^{+}$ | 554 | 614 | 43 ± 4 |
| $\Lambda pK^{o}\pi^{+}$-$\Sigma pK^{o}\pi^{+}$ | 59 | 42 | |
| $\Lambda pK^{o}\pi^{+}$-$\Lambda pK^{+}\pi^{o}$ | 71 | 71 | |
| $\Lambda pK^{o}\pi^{+}$-$\Lambda nK^{+}\pi^{+}$ | 41 | 36 | |
| $\Lambda pK^{+}\pi^{o}$-$\Lambda K^{+}p\pi^{o}$ | 20 | 19 | |
| $\Lambda nK^{+}\pi^{+}$-$\Lambda n\pi^{+}K^{+}$ | 50 | 55 | |
| $\Lambda$ + 2 prong + two or more missing neutrals | 1148 | 1275 | |

A. These are the corrected numbers of events after minimum length and projected opening angle cuts and corresponding weightings have been applied to the data.

$K^o$'s to be depleted in the region $\frac{t}{\tau} < 0.2$. These depletions are assumed to be a result of the inability to detect $V^o$ decays occurring close to the production vertex. A minimum length cutoff of 1.2 cm and a corresponding weighting were applied to the sample to correct for this effect. The corrected number of events then agreed with that expected. The details of this and also a projected opening angle correction are given in Appendix A. Evidence for the bias against $\Lambda$'s with small projected opening angle was found in the doubly differential solid angle distribution of the lambda decay proton. We define $\hat{z}$, the polar axis, along the direction of the $\Lambda$, and measure the azimuthal angle $\phi$ of the decay proton from the plane containing $\hat{z}$ and $\hat{G}$, where $\hat{G}$ is a fixed vector in the bubble chamber which points along the magnetic field toward the top glass. After Lorentz transformation along $\hat{z}$ into the rest frame of the lambda, we expect the solid angle distribution of the decay proton to be isotropic, i.e.,

$$\frac{d^2N}{d\cos\theta\, d\phi} = \text{constant} ,$$

since we have effectively averaged over all azimuthal production configurations and since there can be no component of polarization along the lambda momentum. The experimental distribution in fact shows depletions exactly where they would be expected if a bias against small projected opening angle existed. The $\phi$ projection of this distribution for all $\Lambda$'s with length greater than 1.2 cm is shown in Fig. 2. We have found a $3^o$ minimum projected opening angle cut with the corresponding weighting adequate to correct for the depletions. The final weight for an event is then the product of the two weights we have discussed. The corrected

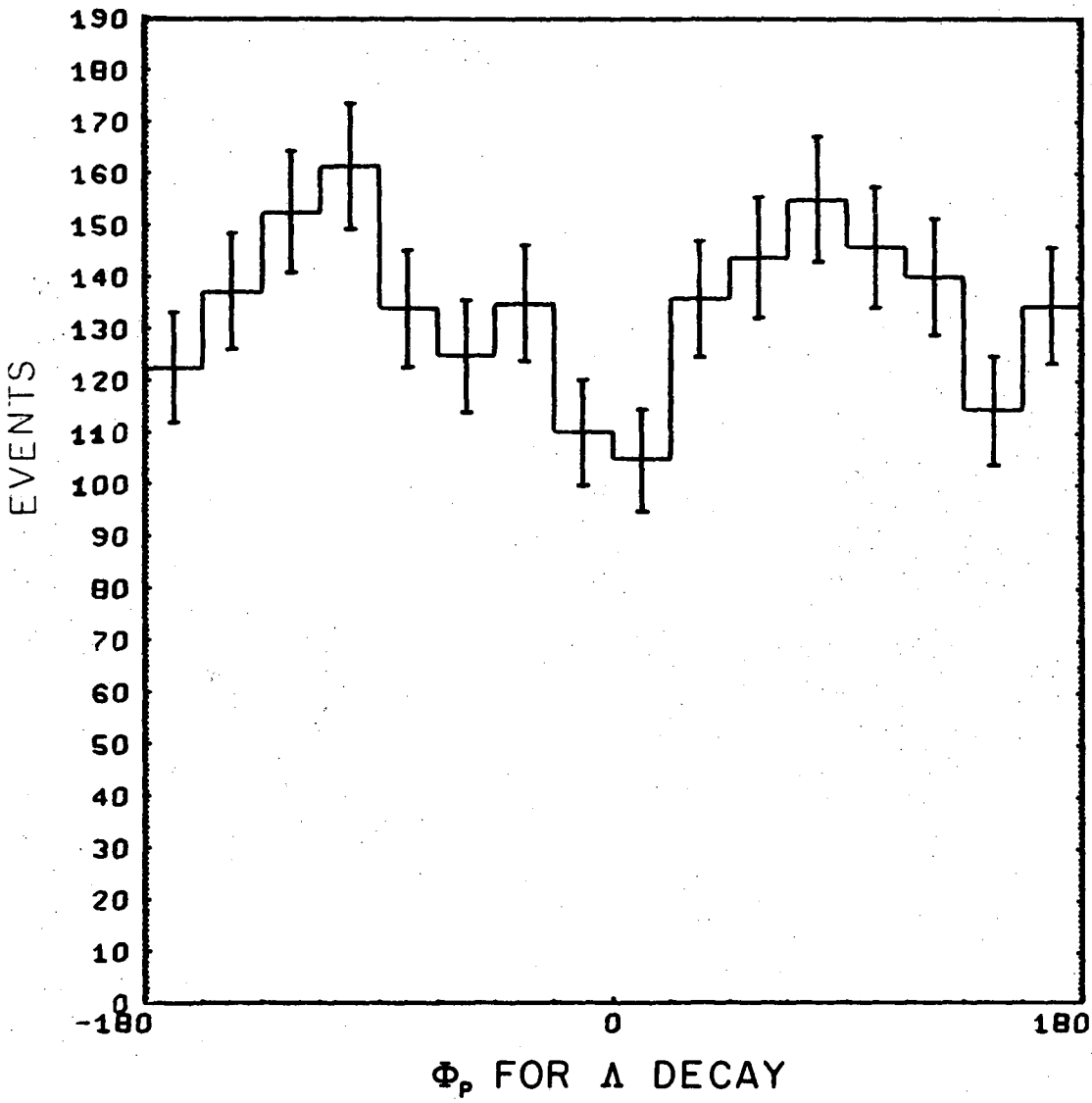


XBL 688-1471

Fig. 2. Azimuthal distribution of the decay proton for all $\Lambda$'s with neutral track length greater than 1.2 cm.

numbers of events for each of the categories mentioned above are also given in Table I. The average weights for the length and projected opening angle corrections are 1.11 and 1.23 respectively. The distribution of final weights for the $\Lambda$'s is found to be narrower than either distribution of the two individual weights. The reason for this is that the two efficiences behave oppositely as a function of momentum. We have also studied the $K^o$ decay distribution, although there are few events compared to the number of $\Lambda$'s. The polar decay angle distribution was found deficient in the region $\cos\theta \approx 90^o$, indicating that decays of very slow $K^o$'s were probably missed by the scanners. The expected branching ratios of 1/4/2 for $(\Lambda)K^o p\pi^+/\Lambda(K^o)p\pi^+/\Lambda K^o p\pi^+$ also indicated this bias. A careful examination of about 40% of the events fitted as examples of $pp \rightarrow \Lambda(K^o)p\pi^+$ with $K^o$ momentum less than 500 MeV/c confirmed our suspicion. The branching ratios for these events after the discovery of the missed $K^o$ decay then was in good agreement with that expected. No further attempt was made to correct for this bias since only about 30 events were completely missing from the total sample of about 1000 events and no differential bias was indicated.

## C. SOURCES OF CONTAMINATION

The unique center-of-mass reflection symmetry of proton-proton collisions may be exploited to determine evidences for possible biases in the data. Since the reactions we analyze are peripheral, angular correlations involving the final state baryons are expected to be the most sensitive to this test. Before examining the final states used in the analysis, we present evidence in Fig. 3 that our criteria for the assignment of events to the category of two missing neutrals discussed above was correct. We plot the distribution of the cosine of the production angle for the lambda in the overall center of mass using weighted events. The reference direction is defined by the beam proton. The events in the plot consist of about half of the entire sample of events in the missing neutrals category. The normalized curve is a simple hand-drawn fit to the data and is included only to indicate the agreement with the center-of-mass symmetry. We now consider in Fig. 4 the production angular distribution for the lambdas in all of the other categories of Table I. The asymmetry between the backward and forward hemispheres is probably not statistical, but is the result of either an exclusion of good events or an inclusion of faked events. Since we have already argued that the former is not the case, we conclude that some faked fits are included in the sample. If this is true, we expect that they are from five-body events having special configurations that fit the four-body hypotheses. The only three-body reaction, $pp \rightarrow \Lambda p K^+$, is not expected to be a source of contamination since it is easily identified and the fit is highly constrained.[22] The final state $\Lambda K^+ \pi^+ n$ appears to be the most seriously contaminated state judging from

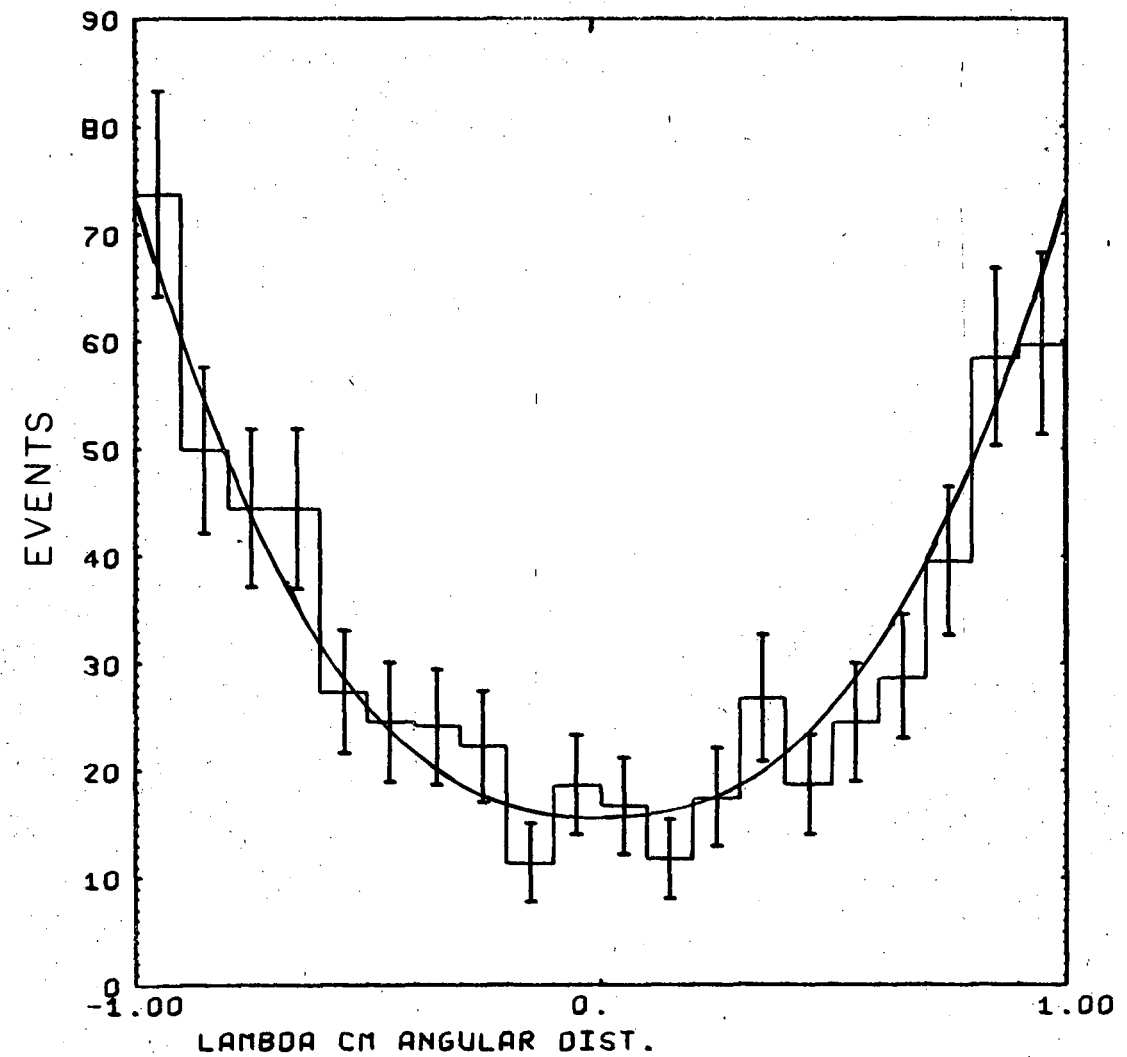


XBL 687-1416

Fig. 3. Production angular distribution of the Λ in the overall center of mass for events with two or more missing neutral particles.

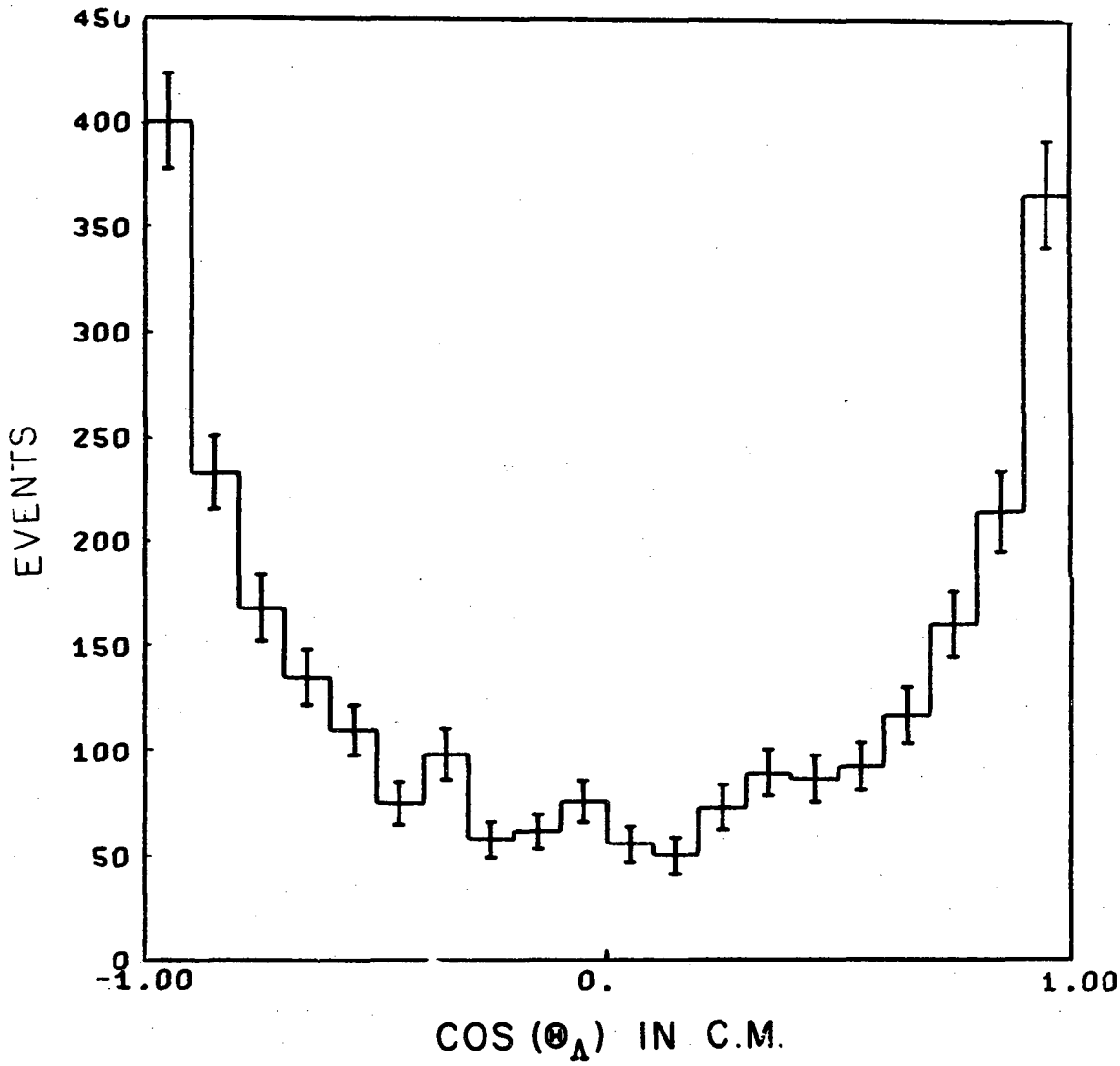


XBL 688-1470

Fig. 4. Production angular distribution of the Λ in the overall center of mass for all four-body events with a visible Λ in the final state.

the asymmetric lambda production angular distribution shown in Fig. 5. In that figure we do not include the events ambiguous with the $\Lambda p\pi^+K^o$ final state although they have the same asymmetric character as the unambiguous ones. Further more, we find the contamination to be almost exclusively confined to a quadrant in the center of mass defined by $\cos\theta_\Lambda < 0$ and $\cos\theta_n < 0$. Here as above the angles of the lambda and neutron are measured relative to the beam proton. The population of 60 events for the reflection symmetric quadrant where both baryons are in the forward direction is about half that of the contaminated quadrant. The other two quadrants contain almost equal populations of 360 and 370 events. The only five-body state which is likely to simulate $\Lambda K^+\pi^+(n)$ and be compatible with the observed bubble densities if $\Lambda p\pi^+(K^o\pi^o)$. Fortunately, about 150 examples of this reaction have been fitted where both the $K^o$ and $\Lambda$ decays are observed. We have reprocessed all of these known five-body events after removing the $K^o$ entirely. The fraction of these events which then fitted the $\Lambda K^+\pi^+(n)$ hypothesis and were consistent with the bubble densities indicated that the contamination could be solely accounted for by this effect. Furthermore, except for 3 out of 27 events, this fake sample populated only that quadrant in the center of mass which initially revealed the contamination. These pseudo events showed no other significant "differential bias," i.e., they were rather uniformly distributed in all of the effective mass and angular distributions. Therefore, for the $\Lambda K^+\pi^+n$ final state, only the cross section needs to be corrected. In addition to those five-body events which after removal of the $K^o$ fitted the $\Lambda K^+\pi^+n$ hypothesis, a smaller number fitted the $\Lambda K^+p\pi^o$ hypothesis. This sample was statisically insufficient

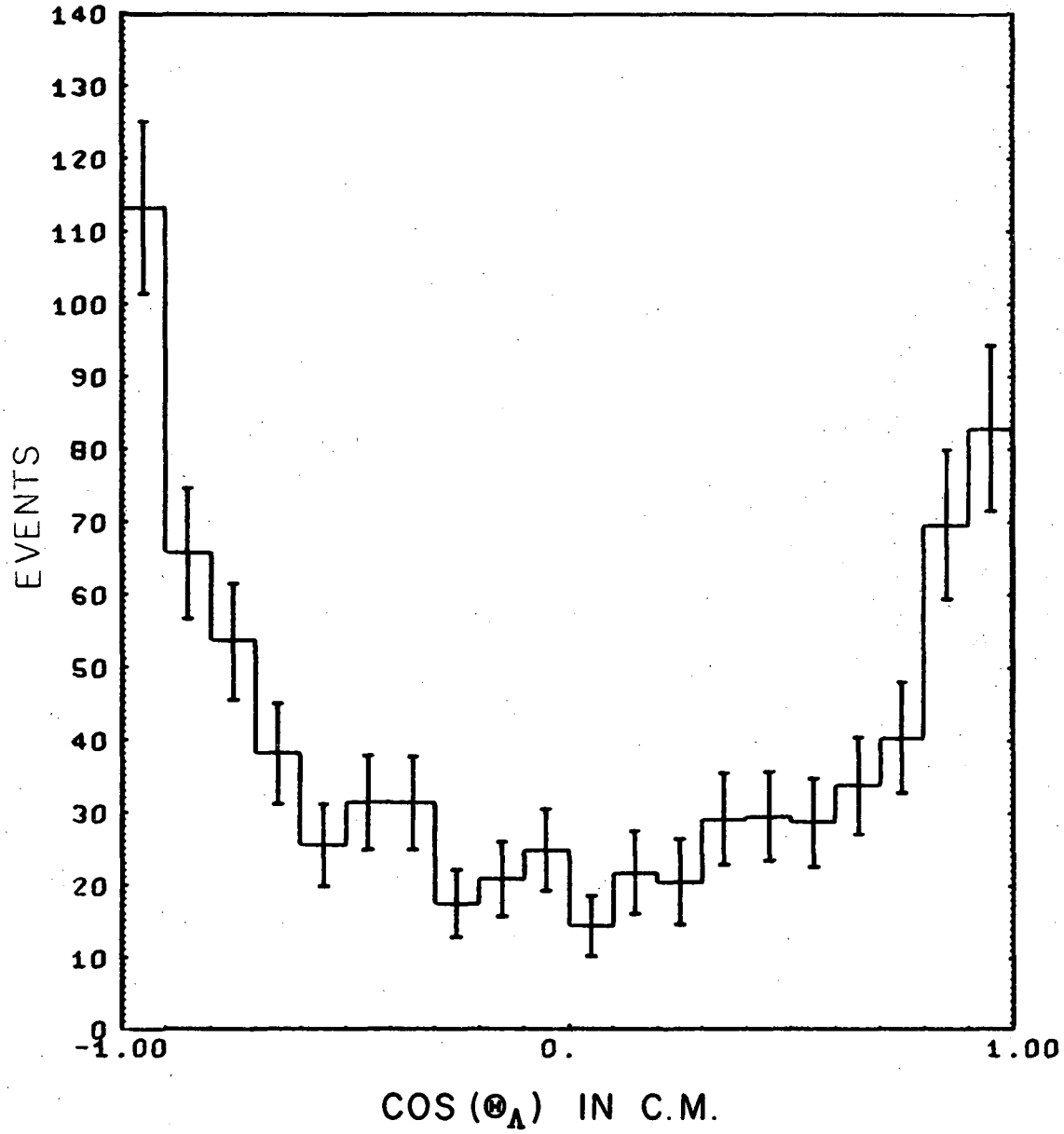


XBL 688-1472

Fig. 5. Production angular distribution of the Λ in the overall center of mass for examples of the reaction $pp \rightarrow \Lambda nK^+\pi^+$.

for studying the differential biases. Besides this source and the three-body $\Sigma^o$ ambiguity mentioned in Section IIB, we expect the $\Lambda K^+ p\pi^o$ and the $\Lambda K^+ n\pi^+$ events to be contaminated by true $\Sigma^o$ events. Unfortunately, we do not know the $\Sigma^o$ cross sections for these two states and hence cannot know the magnitude of this effect. However, an upper limit can be estimated. If it is assumed that the relative production rate of $\Sigma^o$ and $\Lambda$ for each of these two four-body $K^+$ states is the same as in the final states $\Sigma^o K^o p\pi^+$ and $\Lambda K^o p\pi^+$ and that their production mechanisms are similar, then the $\Sigma^o$ contamination in these $K^+$ states is expected to be less than 8%. This number is based on the assumption that all of the ambiguities between $\Lambda K^o p\pi^+$ and $\Sigma^o K^o p\pi^+$ belong to the latter category, and is hence likely to be an over-estimate. In fact, judging from the center of mass production angular distribution, it is more probable that most of those events are truly $\Lambda$ events since the $\Lambda$ production angular distribution for the $K^o$ state is depleted in the backward hemisphere and the ambiguous events would help to correct this asymmetry. However, from our study of the n final state, we expect the five-body reaction $pp \rightarrow \Lambda p K^+(\pi^o\pi^o)$ to be a source of contamination in the $\Lambda p\pi^+(K^o)$ events. This would affect the symmetry of the production angular distributions and hence we feel we are unable to reliably assign ambiguous events using only the symmetry criterion. Other methods of investigating the ambiguous events, such as studying the scatter plot of missing mass for one hypothesis vs. missing mass for the other hypothesis, have failed to indicate any preference for assigning them. For these reasons, we have decided that the most reasonable procedure to follow is to include an ambiguous event in both categories with a weighting factor of 1/2,

although no significant changes are observed if we vary the factor from 0 to 1. Besides estimating the size of the five-body contamination, we have also included the ambiguous event weighting procedure as a source of error in the cross section calculations. The biases we have discussed are all relatively small compared to the total numbers and we estimate the $\Lambda p K^+ \pi^o$ final state to be the most seriously affected and place an upper limit of 15% on this undesirable background.

## III. CROSS SECTION DETERMINATION

From the definition of cross section, the number of interactions into channel i, $N_i$, taking place in a length dx is given by:

$$dN_i = N(x)D\sigma_i dx$$

where $N(x)$ is the number of beam particles at x, D is the number density of targets per $cm^3$, and $\sigma_i$ is the corresponding cross section for the particular process. Since

$$\sum_i dN_i = - dN$$

it follows that

$$\sum_i \sigma_i = \sigma_T$$

and

$$N(x) = N(x = 0)\, e^{-D\sigma_T x}$$

where $\sigma_T$ is the total cross section. Hence, the total number of interactions over a length L into channel i is given by

$$N_i = \frac{\sigma_i}{\sigma_T} N(x = 0)\, (1 - e^{-D\sigma_T L}) .$$

Experimentally we do not measure $N(x = 0)$ but rather $N(x = L)$, the number of beam tracks which enter and leave the fiducial volume without interacting. Therefore,

$$\sigma_i = \sigma_T \frac{N_i}{N(x = L)} \frac{1}{(e^{D\sigma_T L} - 1)} .$$

In practice, some tracks counted as beam tracks have elastically scattered somewhere in the fiducial volume with small momentum transfer to the

target. Let $N_S$ be the number of interactions of this type, and $N^{OBS}$ be the number actually counted, then

$$N^{OBS} = N(x = L) + N_S .$$

But $N_S$ is given by

$$N_S = N(x = L) \frac{\sigma_S}{\sigma_T} (e^{D\sigma_T L} - 1)$$

so

$$N^{OBS} = N(x = L) \left[ 1 + \frac{\sigma_S}{\sigma_T} (e^{D\sigma_T L} - 1) \right] .$$

Solving this equation for $N(x = L)$ and substituting into the equation above for $\sigma_i$ we obtain:

$$\sigma_i = \sigma_T \frac{N_i}{N^{OBS}} \left[ \frac{1}{(e^{D\sigma_T L} - 1)} + \frac{\sigma_S}{\sigma_T} \right] .$$

We estimate that recoil protons with momentum $< 100$ MeV/c are not observed and we use $\sigma_S = 1.6$ mb.[27]

We have counted tracks in about 1,000 frames evenly spaced throughout the film and find

$$N^{OBS} = 5{,}090{,}000 \pm 150{,}000 .$$

The uncertainty given is not the statistical error but rather the average deviation of several measurements of $N^{OBS}$.

Using a fiducial length $L = 125$ cm., and $\sigma_T = 40.6$ mb[28] and $D = (0.361 \pm 0.007)\ 10^{23}/cm^3$ we obtain

$$\sigma_i = N_i\ (.0401 \pm .0014)\ \mu b/event .$$

The number $N_i$ is the sum of the weights for the events in channel i. From Poisson statistics, the uncertainty in $N_i$ is

$$\sqrt{\sum_j w_j^2}$$

where $w_j$ is the weight for the $j^{th}$ event. In all of our histograms with error bars, the same method of calculating the uncertainty is used.

The cross sections are also corrected for the scanning efficiency. In two independent scans, we found efficiencies of $0.80 \pm 0.03$ and $0.82 \pm 0.03$ resulting in a combined efficiency of $0.96 \pm 0.02$.

# IV. RESONANCE PRODUCTION

## A. General Features

Since the three final states $\Lambda K^{o}p\pi^{+}$, $\Lambda K^{+}p\pi^{o}$, and $\Lambda K^{+}n\pi^{+}$ each contain the same hadrons differing only in their charges, we expect the dynamical mechanisms of their production to be related. With few exceptions, we indeed find the same general behavior in the data for each state. Therefore, we discuss the three final states simultaneously.

All of the expected pionic resonances, namely Y*(1385), K*(890), and N*(1236) are observed. We also find evidence in all channels for peripheral production of $N^{*}_{3/2}(1950)$ and subsequent decay into Y*K. Our analysis of this pseudo-two-body state is somewhat lengthy and is given separately in Section B. We also observe low mass enhancements in each $\Lambda K$ mass spectrum. These enhancements could be associated with any of three I=1/2 resonances, but since our data are insufficient for an adequate study we account for these enhancements only in a phenomenological way in Section V using a pion exchange model.

In order to estimate amounts of the pionic resonances produced, we have fitted the data for each final state to a sum of pure phase space plus resonant phase spaces. Although certain features of the data are certainly in disagreement with the simplifying assumptions of isotropic production and decay of the resonances, we nevertheless are able to reliably estimate the amounts of N*, K*, and Y* production. These amounts obtained by fitting to our phase space model are in excellent agreement with the corresponding calculation done for a pion-exchange model where the overall agreement with the data is quite good.

In the model for four-body production where no correlation of the final state with the initial state is included, five independent variables are necessary to specify the final state. For each final state we have fitted the experimental density in this five-dimension space to an incoherent sum of N-1 different resonant processes and one pure phase space process.

$$f(\alpha,x) = \sum_{j=1}^{N} \alpha_j |M_j(x)|^2 \rho(x) \quad .$$

Here the $\alpha_j$ are the relative intensities of the different processes being fitted, x denotes the set of five independent variables, the $|M_j|^2$ are the corresponding Lorentz invariant matrix elements squared, and $\rho(x)$ is the phase space density. So that the $\alpha_j$ corresponds to relative intensities, we require:

$$\int |M_j(x)|^2 \rho(x) dx_1 .. dx_5 = 1 \text{ for each } j$$

and

$$\alpha_N = 1 - \sum_{j=1}^{N-1} \alpha_j \quad .$$

These conditions also insure the normalization of the distribution function:

$$\int f(\alpha,x) dx = 1 \quad .$$

The likelihood function is then given by

$$L = \Pi_i f(\alpha,x^i)^{w_i}$$

where i enumerates the events and $w_i$ is the weight for the $i^{th}$ event. The function which we actually maximize is the log of the likelihood function:

$$H(\alpha) = \ln L = \sum_i w_i \ln \sum_j \alpha_j |M_j(x^i)|^2 \quad .$$

Notice we have dropped the term $\sum_i \ln \rho(x^i) \cdot w_i$ which is independent of the $\alpha_j$. This results in an extremely important simplification, since in the most general case this term contains over 100 factors if the five variables are all chosen to be effective masses[29] and it would be very time consuming to evaluate all of these factors for every event. Although the normalization integrals also involve $\rho$, each can be easily evaluated numerically by transforming to an appropriate set of variables in which the expression for $\rho$ becomes trivial.

The forms of the $|M_j|^2$ we use are

for the pure phase space process $|M_N|^2 = \text{const}$

for N*(1236), K*(890), and Y*(1385) resonances

$$|M_j|^2 = \text{const} \frac{m^2}{p} \frac{\Gamma(m)}{(m^2-m_o^2)^2 + m_o^2 \Gamma^2(m)}$$

where m is the invariant mass of the resonant pair of particles and p is the momentum of either one in the rest frame of m. We use the same width in the denominator as in the numerator since all of the resonances are nearly 100% elastic. The constants are determined by the normalization conditions above. For N*(1236) and Y*(1385) we use:

$$\frac{\Gamma(m)}{\Gamma(m_o)} = \left(\frac{p}{p_o}\right)^3 \left(\frac{m_o}{m}\right) \frac{(E_B+m_B)}{(E_B^o+m_B)}$$

where $E_B$ is the energy of the baryon in the resonance rest system, $m_B$ is the mass of the baryon and $p_o$ and $E_B^o$ are the values of p and $E_B$ at the

nominal resonance mass, $m_o$. For K* (890) we use

$$\frac{\Gamma(m)}{\Gamma(m_o)} = \left(\frac{p}{p_o}\right)^3 \left(\frac{m_o}{m}\right)^2 .$$

Before giving the results of our fits, we briefly describe an independent method of fitting to the same model which was done as a check. Instead of fitting all resonances simultaneously, we have made fits to the individual resonant effective masses. For example, to determine the relative intensity of N* we fit to

$$\frac{d\sigma}{dm_{N\pi}} = \alpha_1 \phi_{K^*}(m_{N\pi}) + \alpha_2 \phi_{Y^*}(m_{N\pi}) + \alpha_3 \phi_{N^*}(m_{N\pi}) + (1-\alpha_1-\alpha_2-\alpha_3)\phi_{PS}(m_{N\pi}) .$$

Each normalized $\phi$ was calculated by numerical integration of the appropriate resonance cross section and is the background contribution for that process in the $N\pi$ mass distribution. The parameters $\alpha_2$ and $\alpha_3$ are held fixed at some reasonable value and $\alpha_1$ is determined from the likelihood fit to the $N\pi$ mass distribution. Once $\alpha_1$ is found, we fit the $\Lambda\pi$ mass distribution and vary only $\alpha_2$, holding $\alpha_1$ fixed at the value determined in the fit to the $N\pi$ mass and $\alpha_3$ fixed at some reasonable value. The $K\pi$ mass distribution is then fitted in the same way and the whole process is then repeated. After one iteration, the values for the $\alpha_j$ converged on exactly the same values obtained from the simultaneous fit to the overall density! The actual mechanics of this second method of fitting are far easier than the first and require considerably less programming effort. We have chosen this latter method for fitting the various pion exchange processes which we describe below in Section V.

We give in Table II the results of our fits for the resonance relative intensities and the corresponding cross sections. The errors given for the relative intensity do not strictly correspond to one stan-

Table II. Resonance cross sections for $pp \rightarrow \Lambda NK\pi$ at 6 BeV/c.

| | Y*(1385) | N*(1236) | K*(890) | Background |
|---|---|---|---|---|
| $\Lambda pK^{o}\pi^{+}$ | | | | |
| Relative Fraction | 0.18±0.02 | 0.36±0.04 | 0.10±0.03 | 0.36±0.04 |
| Cross section (μb) | 11±2 | 23±3 | 6±2 | 23±3 |
| $\Lambda pK^{+}\pi^{o}$ | | | | |
| Relative Fraction | 0.19±0.03 | 0.10±0.04 | 0.04±0.02 | 0.67±0.04 |
| Cross section (μb) | 7±1 | 4±2 | 2±1 | 26±4 |
| $\Lambda nK^{+}\pi^{+}$ | | | | |
| Relative Fraction | 0.34±0.02 | 0.0 ±0.03 | -- | 0.66±0.03 |
| Cross section (μb) | 15±2 | 0±1 | -- | 29±3 |

dard deviation since the parameters are correlated, but only indicate the degree of precision with which we determine the various relative intensities.

Since the initial p-p state is pure I=1, we obtain a prediction for the branching ratios of N*(1236). Isotopic spin invariance also predicts a ratio of 2/1 for K*$^+$(890) decay into $K^0\pi^+/K^+\pi^0$ although no similar relations for Y*(1385) exist. The resonance cross sections are seen to be in reasonable agreement with the predicted ratios of 9/2/1 for $\Lambda K^0 N^{*++}(p\pi^+)/\Lambda K^+ N^{*+}(p\pi^0)/\Lambda K^+ N^{*+}(n\pi^+)$ and 2/1 for $K^{*+}(K^0\pi^+)/K^{*+}(K^+\pi^0)$.

In Figs. 6 through 14 we display the various $N\pi$, $\Lambda\pi$, and $K\pi$ mass squared spectra used in the fitting. (We include the $K^+\pi^+$ mass$^2$ distribution for completeness.) The curves are the phase space model predictions using the amounts determined in our fits. Except for the $K^0\pi^+$ and $K^+\pi^0$ mass$^2$ distributions, the agreement is reasonable. The enhancements seen in the low $(K\pi)^+$ mass region correspond to a mass of about 725 MeV/c$^2$ and a width of about 70 MeV/c$^2$. There have been similar enhancements observed in different experiments, but interpretation of them as evidence for a bonafide resonance has been generally unaccepted since the enhancement is often not seen where it would be expected and the width seems to vary considerably.[34] The possibility that the effects we see are dynamically correlated with N*(1236) or Y*(1385) production is difficult to test since phase space alone simultaneously favors low $N\pi$, low $\Lambda\pi$, and low $K\pi$ masses.[29] However, the lack of any enhancement in the $K^+\pi^+$ mass$^2$ distribution for the $\Lambda K^+\pi^+ n$ state where Y*(1385) production is strongest tends to rule out Y*(1385) as a cause. It may be important that the $K\pi$ enhancement is largest in the state where N*(1236) production is dominant and is absent in the state where no N*(1236) is observed, although these facts may rather be only a consequence of the

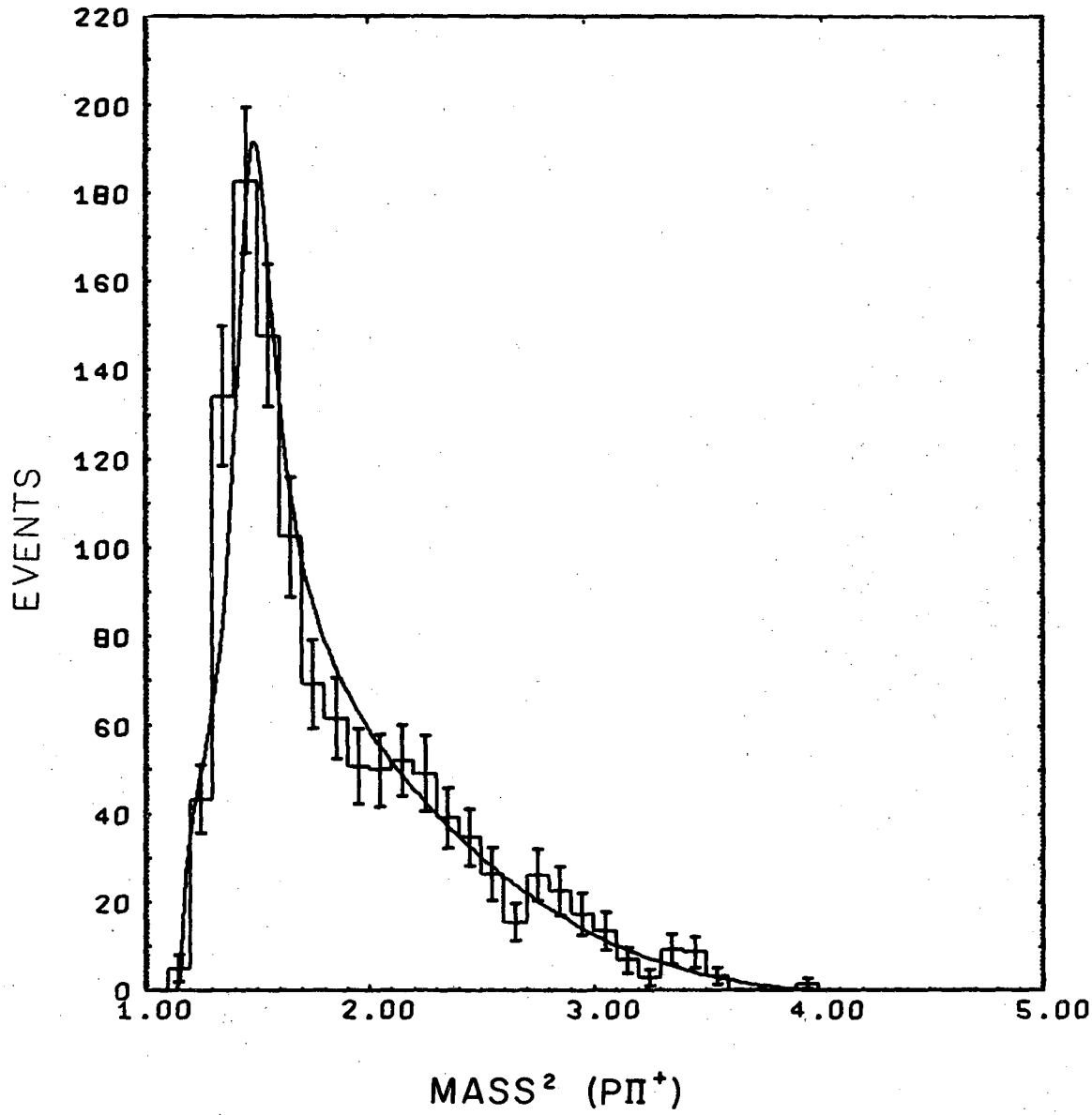


XBL 688-1479

Fig. 6. Effective mass squared distribution of $p\pi^+$ for the reaction $pp \rightarrow \Lambda pK^0\pi^+$ (1170 events). The curve is for a phase space model described in the text.

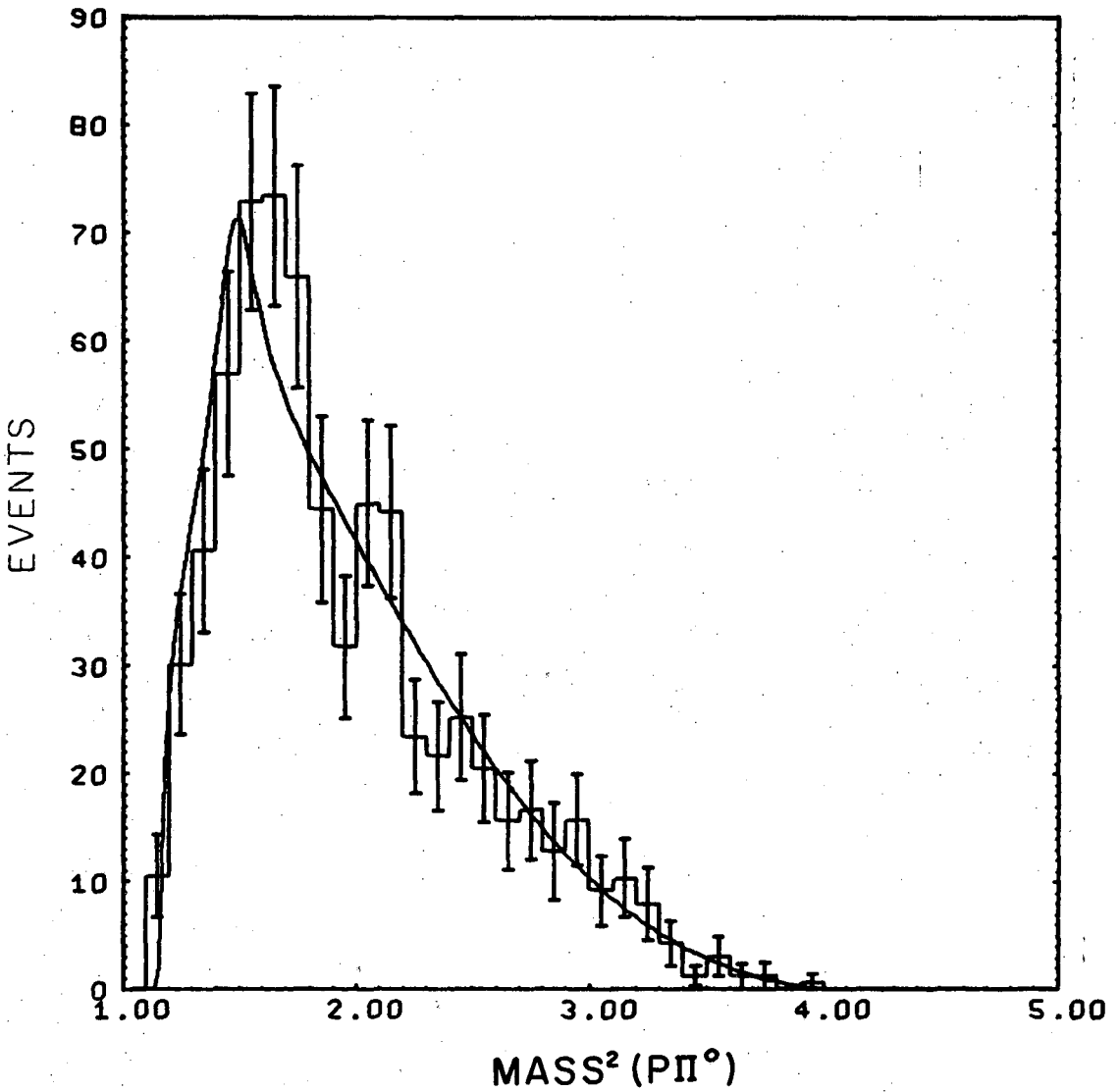


XBL 688-1480

Fig. 7. Effective mass squared distribution of $p\pi^o$ for examples of the reaction $pp \rightarrow \Lambda pK^+\pi^o$ (708 events). The curve is for a phase space model described in the text.

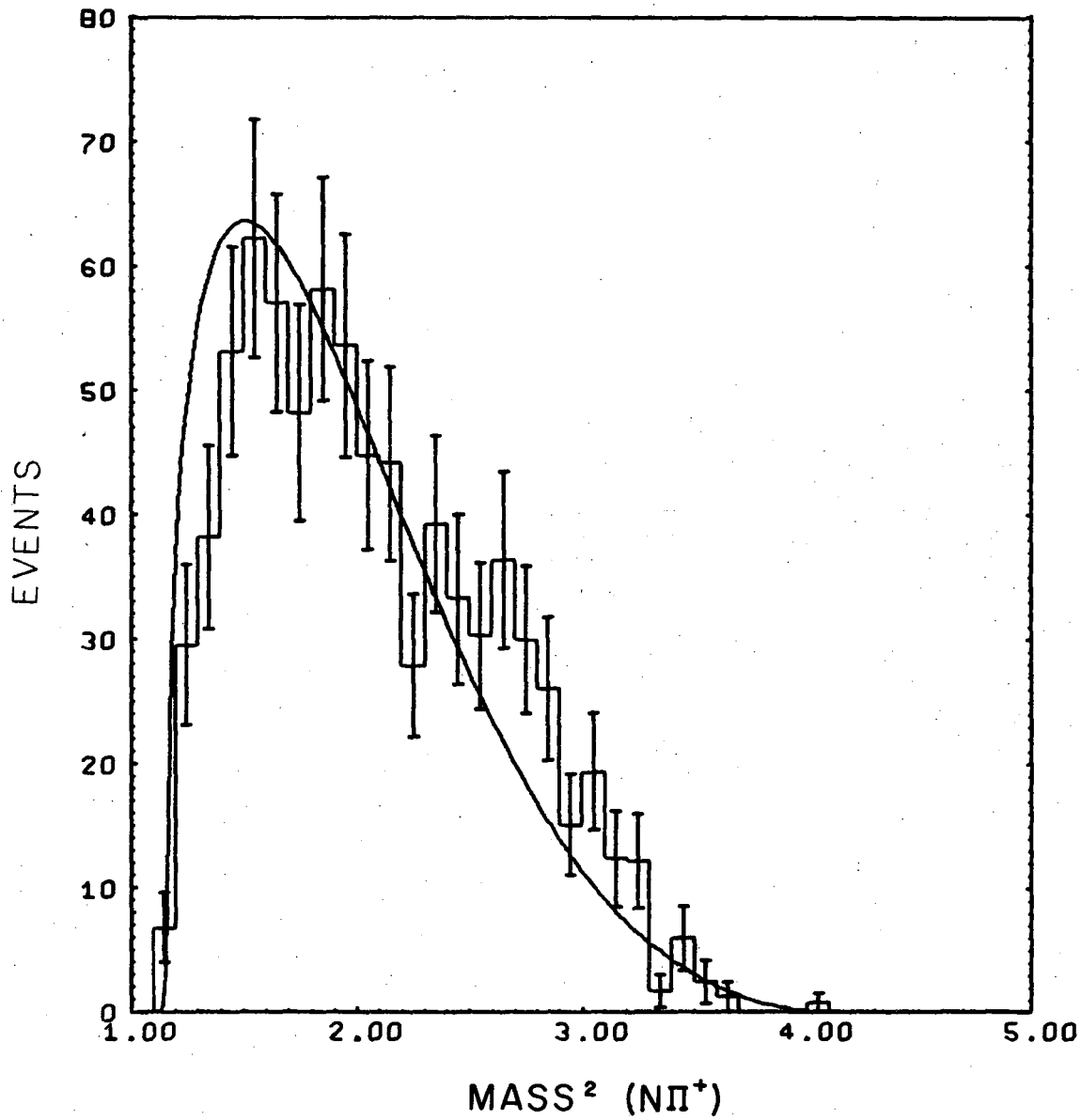


XBL 688-1481

Fig. 8. Effective mass squared distribution of $\Lambda\pi^+$ for the examples of the reaction $pp \rightarrow \Lambda pK^0\pi^+$ (1170 events). The curve is for a phase space model described in the text.

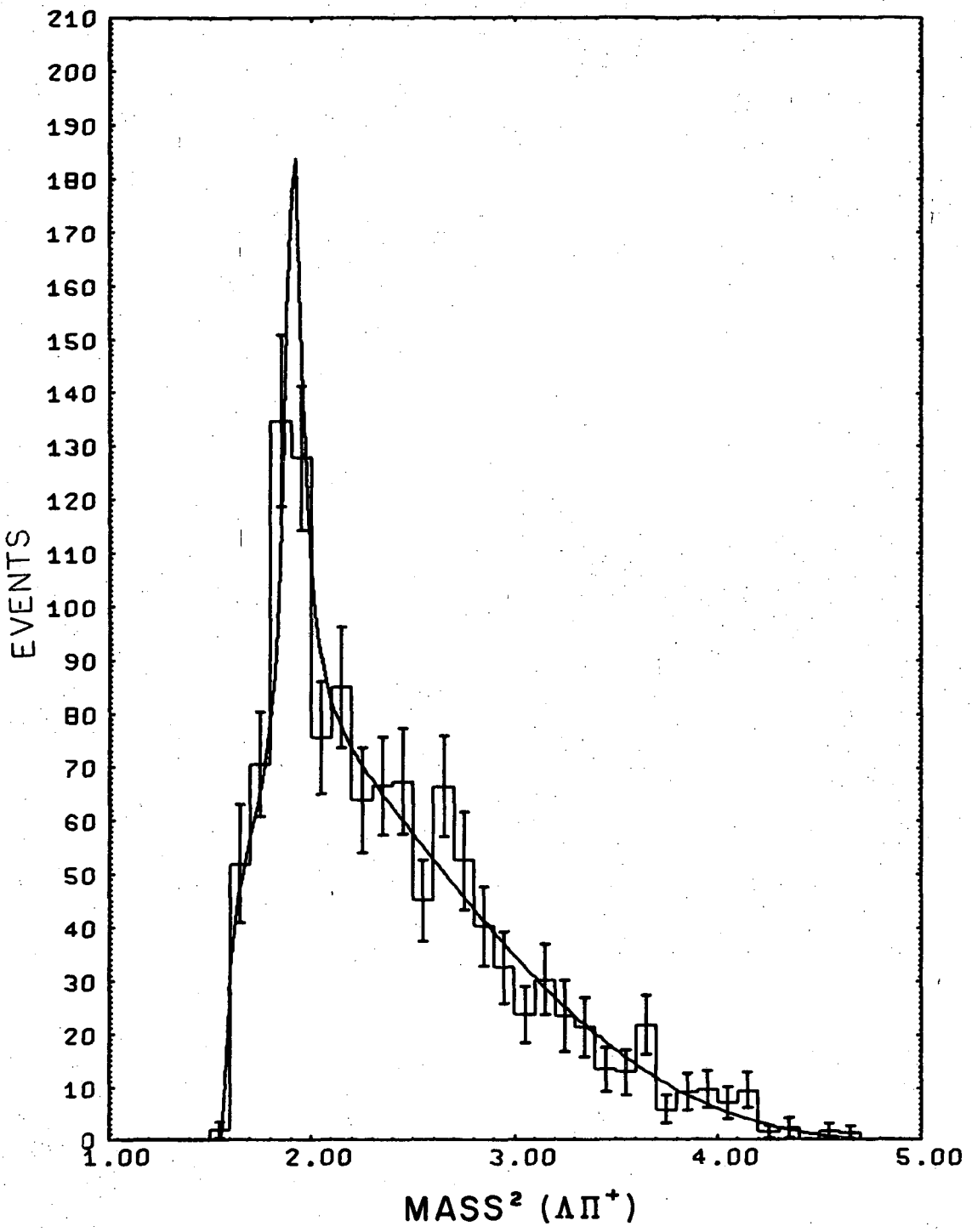


XBL 688-1474

Fig. 9. Effective mass squared distribution of $\Lambda\pi^+$ for examples of the reaction $pp \rightarrow \Lambda pK^o\pi^+$ (1170 events). The curve is for a phase space model described in the text.

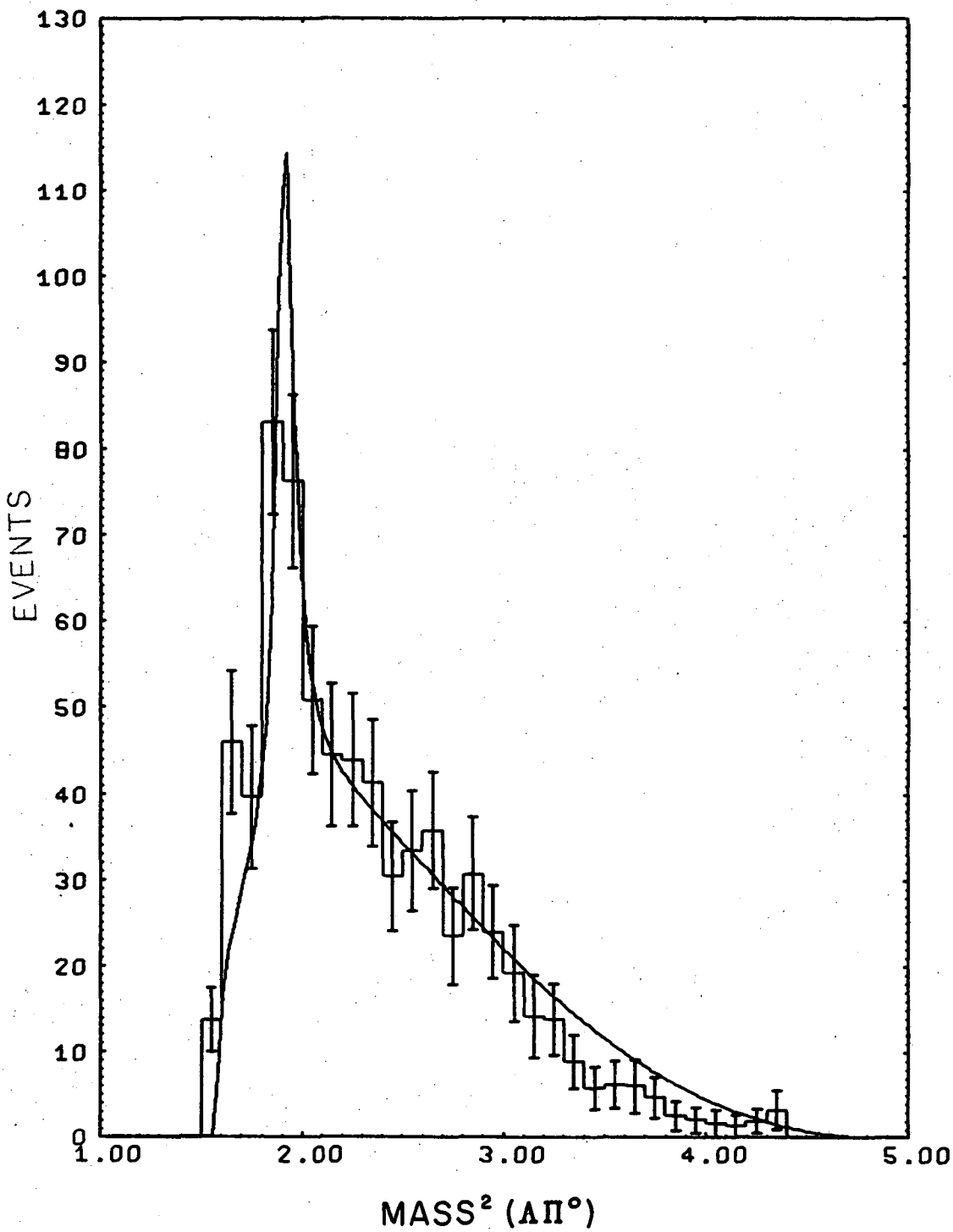


XBL 688-1473

Fig. 10. Effective mass squared distribution of $\Lambda\pi^0$ for examples of the reaction $pp \rightarrow \Lambda pK^+\pi^0$ (708 events). The curve is for a phase space model described in the text.

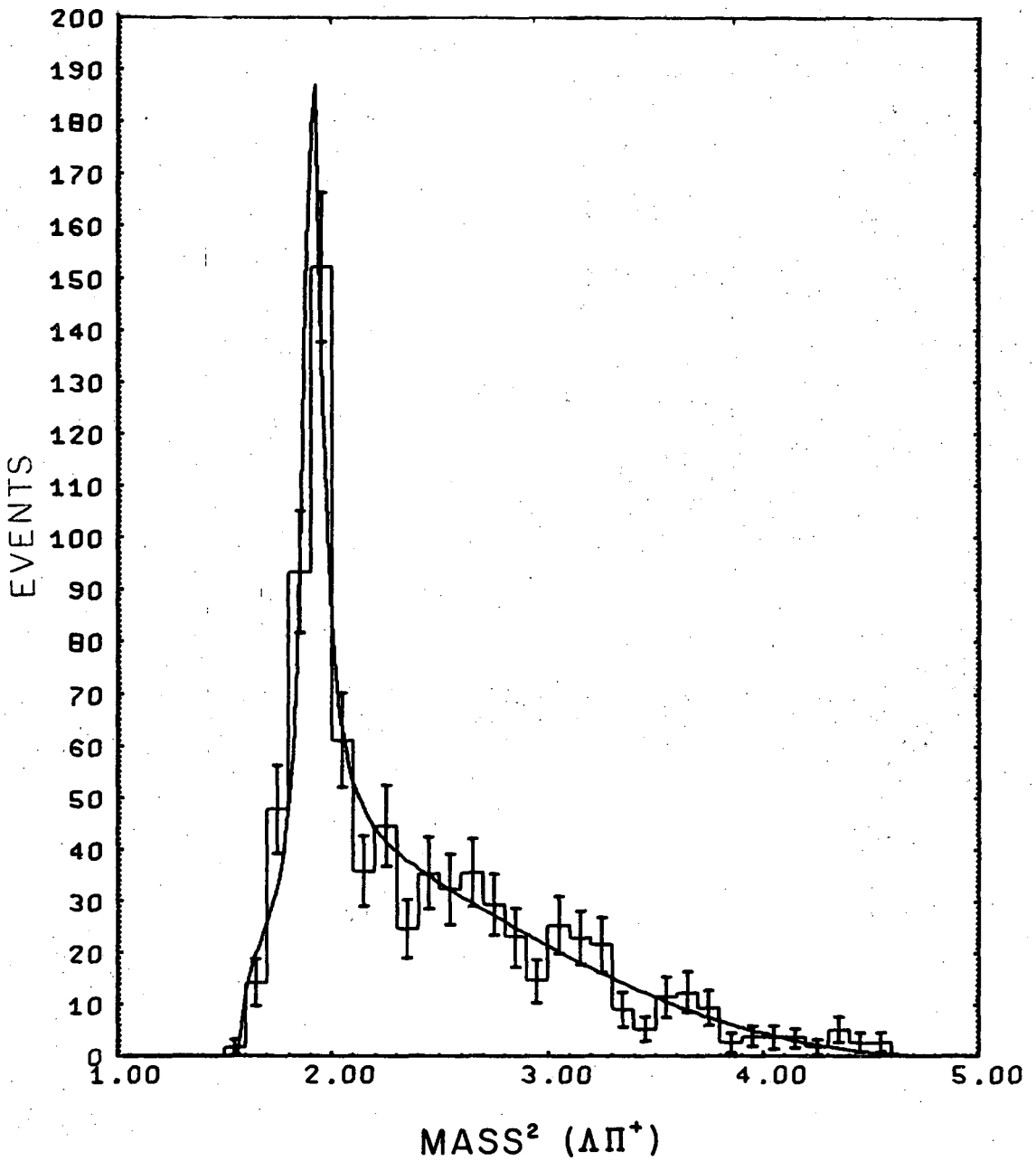


XBL 688-1475

Fig. 11. Effective mass squared distribution of $\Lambda\pi^+$ for examples of the reaction $pp \rightarrow \Lambda nK^+\pi^+$ (791 events). The curve is for a phase space model described in the text.

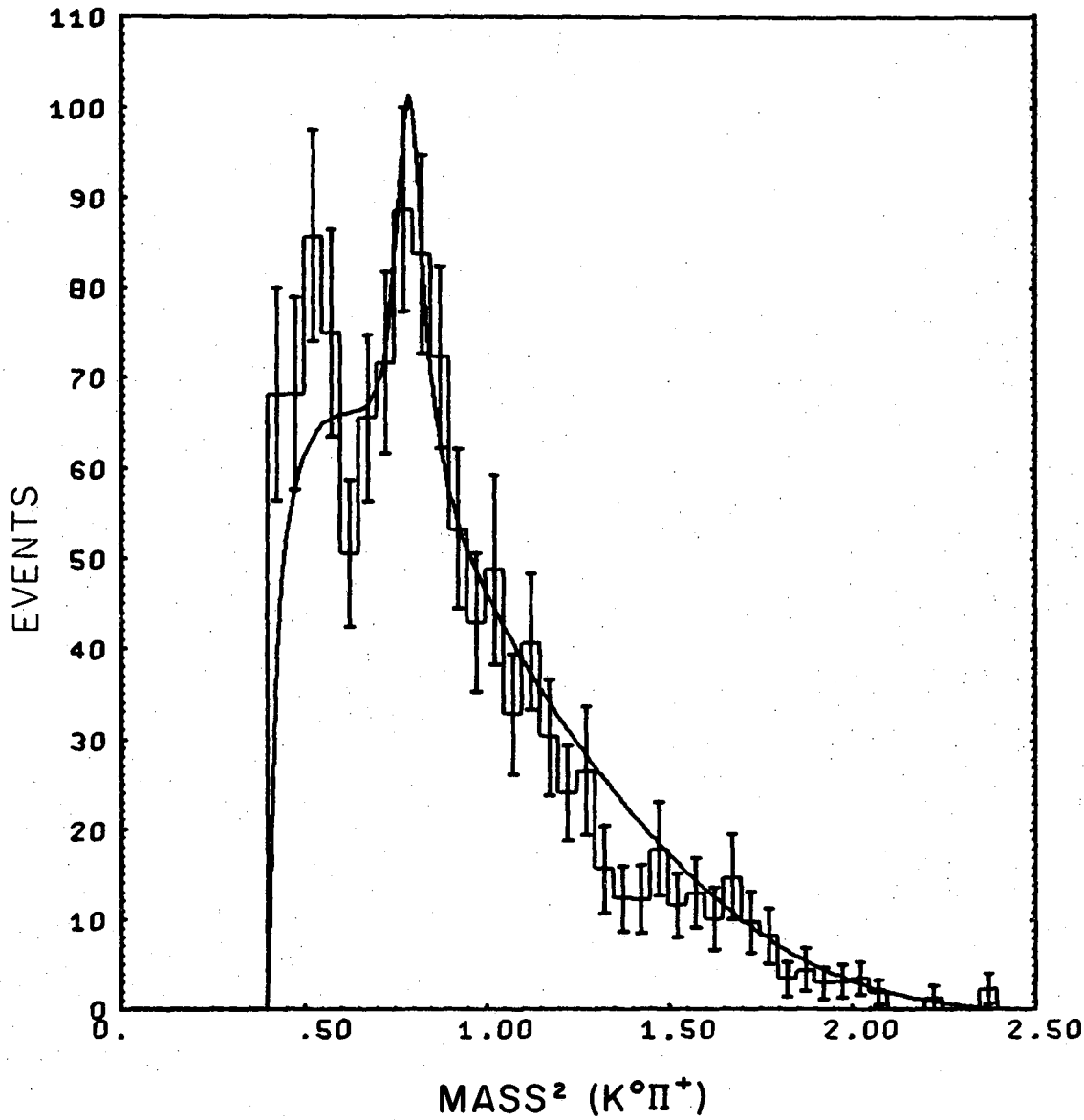


XBL 688-1478

Fig. 12. Effective mass squared distribution of $K^{o}\pi^{+}$ for examples of the reaction $pp \rightarrow \Lambda pK^{o}\pi^{+}$ (1170 events). The curve is for a phase space model described in the text.

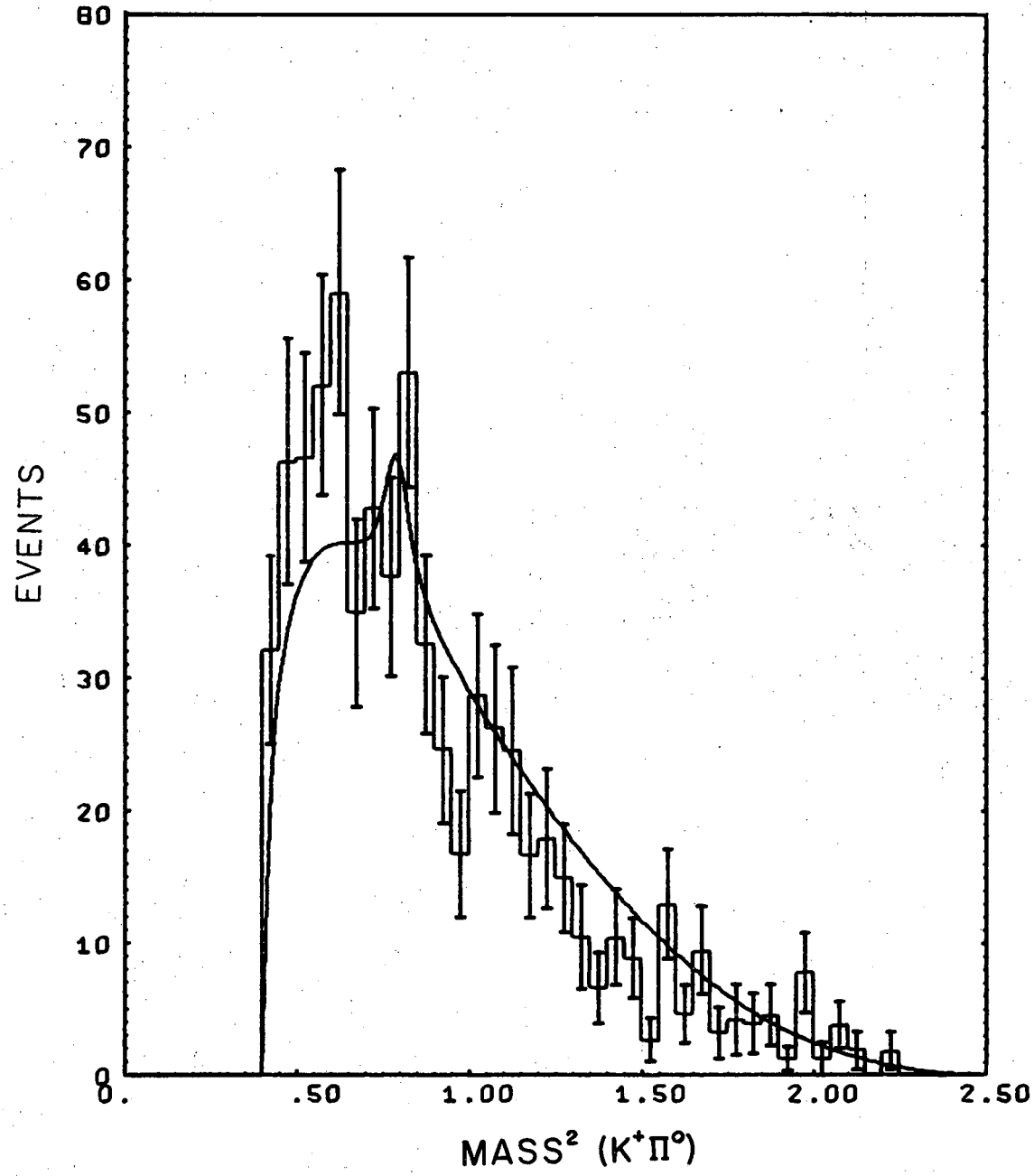


XBL 688-1477

Fig. 13. Effective mass squared distribution of $K^+\pi^o$ for examples of the reaction $pp \rightarrow \Lambda pK^+\pi^o$ (708 events). The curve is for a phase space model described in the text.

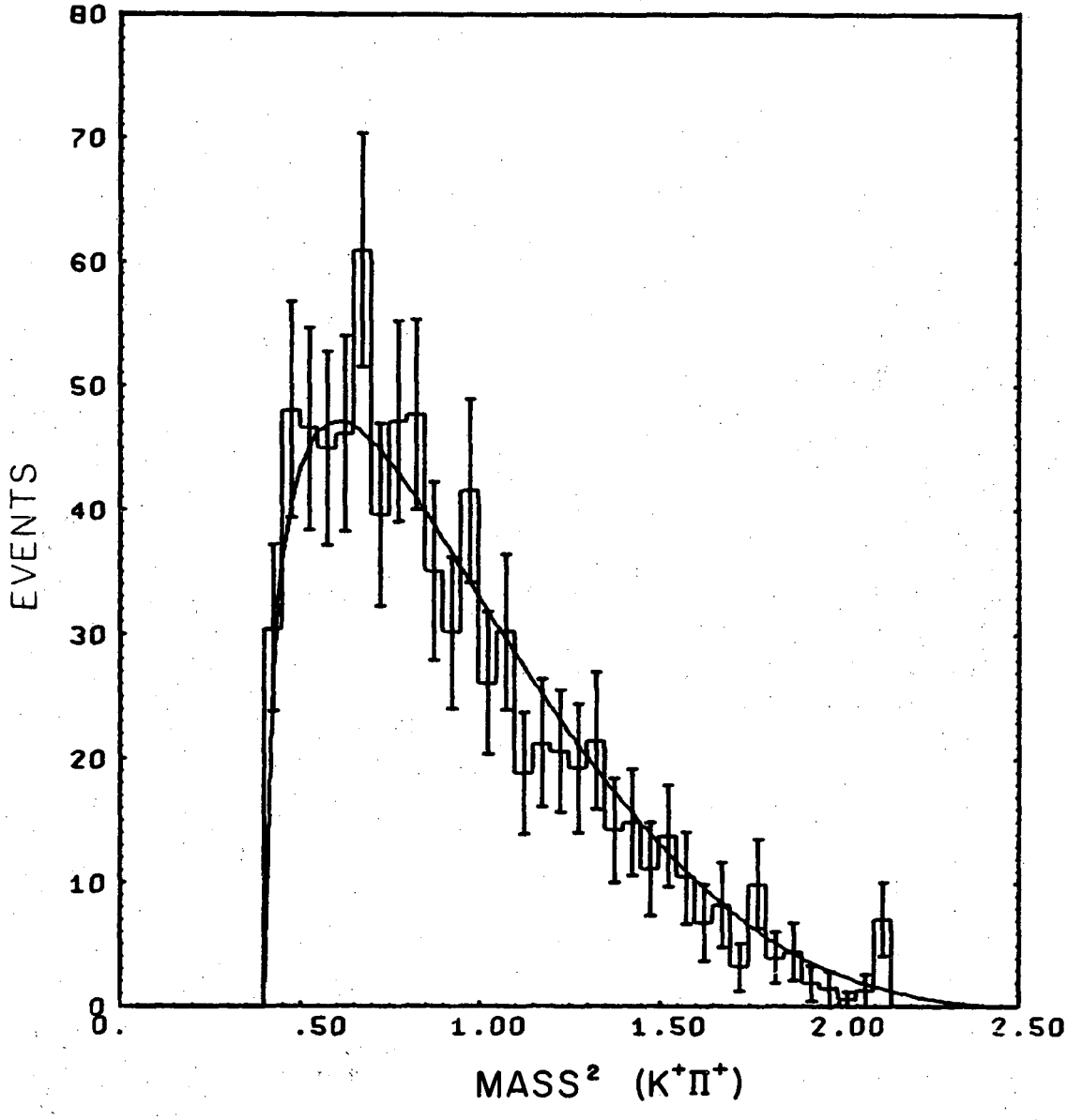


XBL 688-1476

Fig. 14. Effective mass squared distribution of $K^+\pi^+$ for examples of the reaction $pp \rightarrow \Lambda nK^+\pi^+$ (791 events). The curve is for a phase space model described in the text.

I=1/2 $K\pi$ interaction. The corresponding pion exchange predictions for the $K^{o}\pi^{+}$ and $K^{+}\pi^{o}$ mass distributions (displayed in Figs. 30 and 44, respectively) also fail to indicate any peaking in the low $K\pi$ mass region.

Although the $K\pi$, $N\pi$, and $\Lambda\pi$ effective mass distributions are in rather good agreement with our simple phase space model, there are other distributions which are not. Besides the angular distributions, which are hardly expected to agree, the $\Lambda N$ effective mass distributions seem to be the worst. In Fig. 15 we display the $\Lambda p$ effective mass for the $\Lambda p K^{o}\pi^{+}$ final state as an example. The normalized curve is again the prediction of the phase space model. This lack of agreement is an indication that we need a more sophisticated model in which the angular correlations of the final state particles are included. In Section V we describe such a model and find that pion exchange is successful in describing almost all aspects of our data.

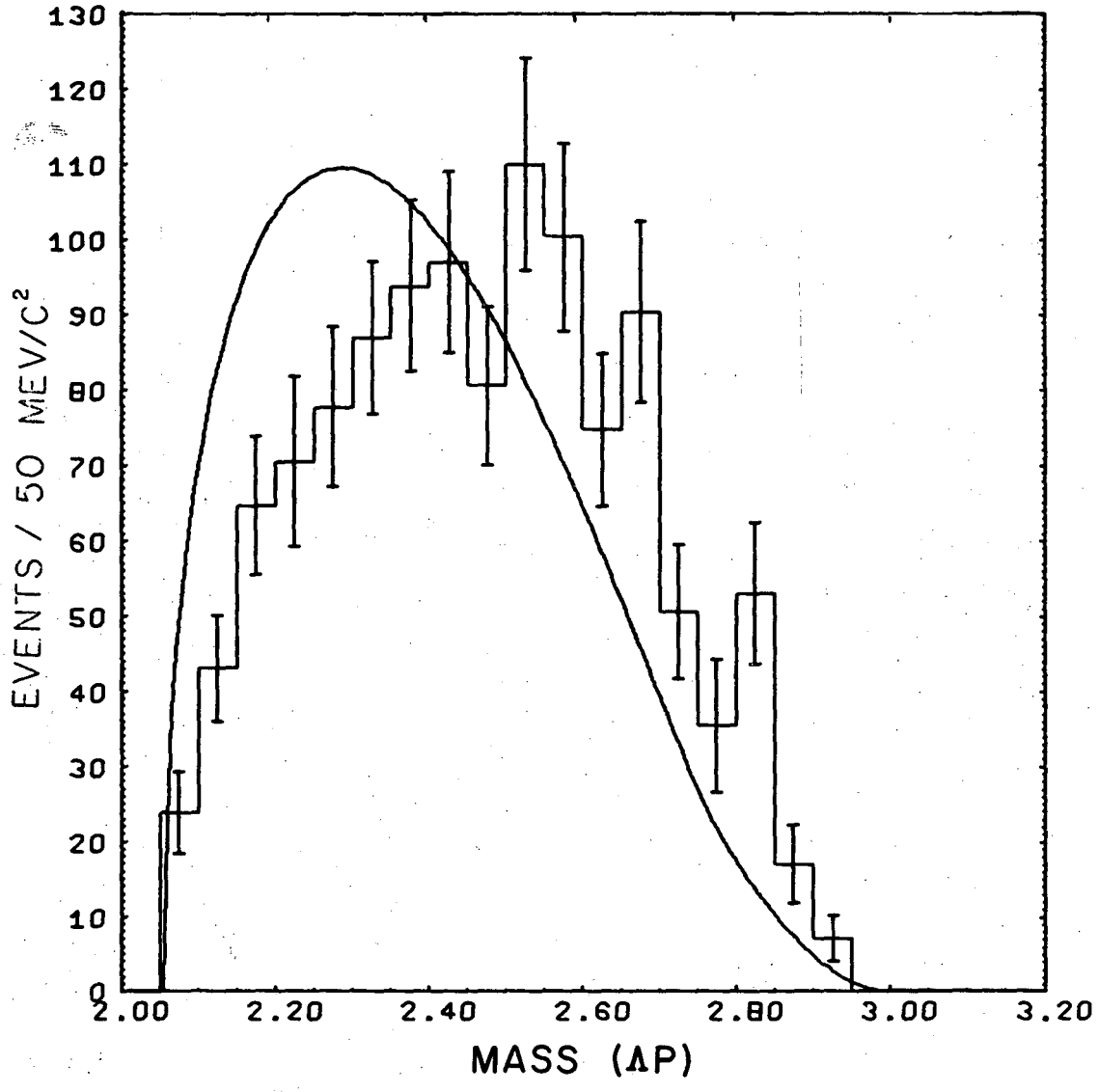


XBL 688-1482

Fig. 15. Effective mass distribution of Λp for examples of the reaction $pp \rightarrow \Lambda p K^{o} \pi^{+}$ (1170 events). The curve is for a phase space model described in the text.

B. Y*K Decay of N*(1950)

An enhancement in the $\Lambda K\pi$ mass spectrum at about 2040 MeV/$c^2$ is seen in each of the three channels we analyze, although the effect is largest in the $\Lambda nK^+\pi^+$ final state. Since we interpret this enhancement as an I=3/2 resonance, the $\Lambda\pi^+K^+$ system is best suited for further study. This system has Iz=3/2 and there is no background from K*(890) production and essentially none from N*(1236). Therefore, the subsequent discussion will be restricted to the $\Lambda nK^+\pi^+$ channel.[30] The $\Lambda K^+\pi^+$ mass distribution is given in the unshaded histogram of Fig. 16 along with a background curve which is calculated as a mixture of 82 percent non-resonant phase space and 18 percent $nY^{*+}K^+$ resonant background. The normalization for this curve and the fraction of Y* are determined from the events with $M(\Lambda\pi^+K^+) > 2.3$ BeV/$c^2$. To provide a more pure sample, exploiting the peripheral character of the production of the resonance, we select events with $|\cos\theta_n| \geq 0.9$, where $\theta_n$ is the angle between the neutron and the beam proton in the overall center of mass. The consequent $\Lambda\pi^+K^+$ mass spectrum for these events is presented in the shaded histogram of Fig. 16; the peak at 2040 MeV/$c^2$ is clearly enhanced.

The corresponding $\Lambda\pi^+$ effective mass spectra for the sample before and after the neutron angle selection are shown in the unshaded and shaded histograms of Fig. 17 , respectively. We see that in the region of Y*(1385) there is particularly little background after the neutron angle selection. Hence, by imposing the additional requirements that the $\Lambda\pi^+$ mass be within the Y*(1385) region, $M(\Lambda\pi^+) = 1385 \pm 35$ MeV/$c^2$, we obtain a nearly pure

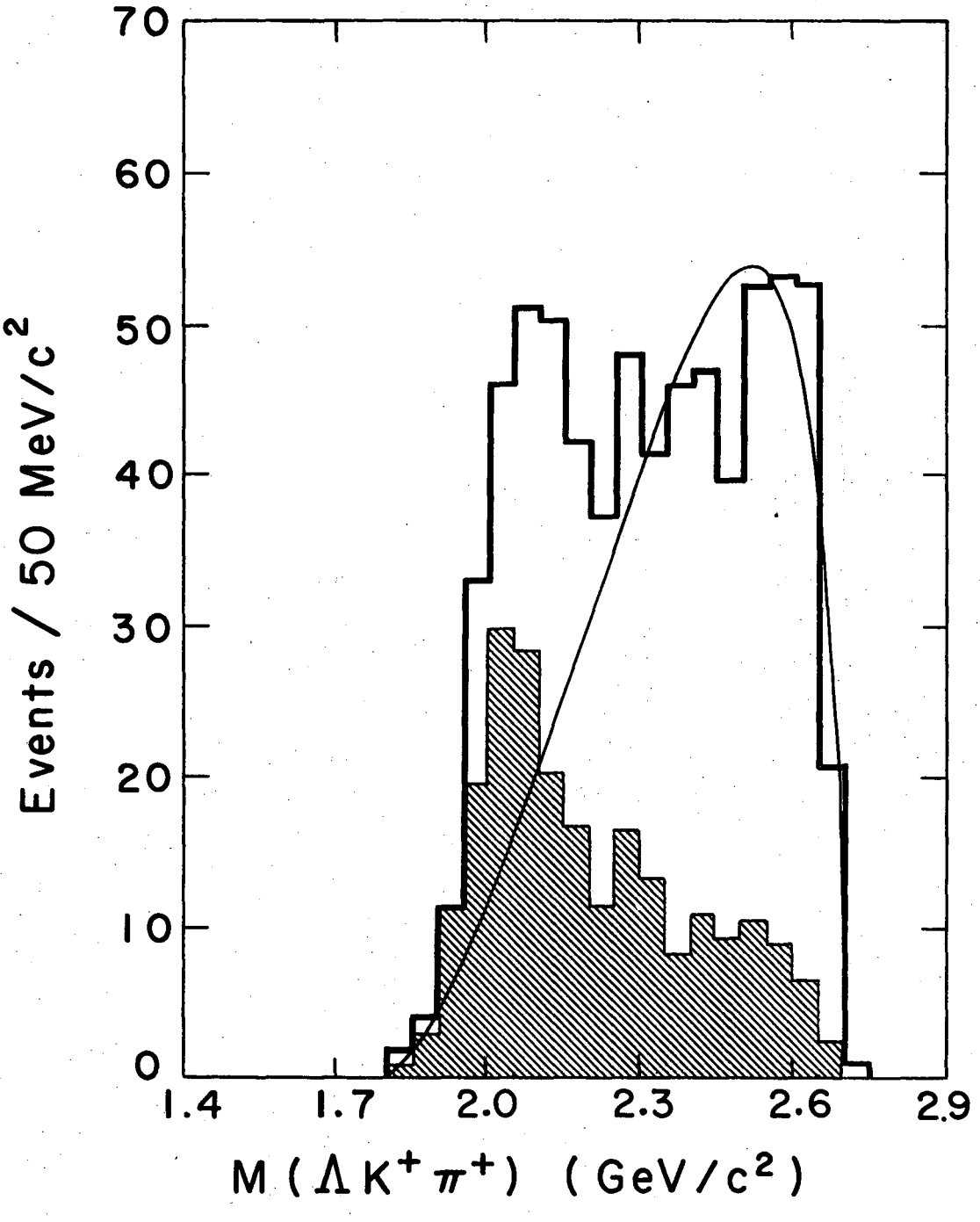


XBL6712-5987

Fig. 16. Effective mass distribution of $\Lambda\pi^+K^+$ for examples of the reaction $pp \rightarrow \Lambda nK^+\pi^+$. The unshaded histogram is for the total sample. (680 events) The shaded histogram corresponds to the requirement that the cosine of the production angle of the neutron be greater than 0.9. (225 events)

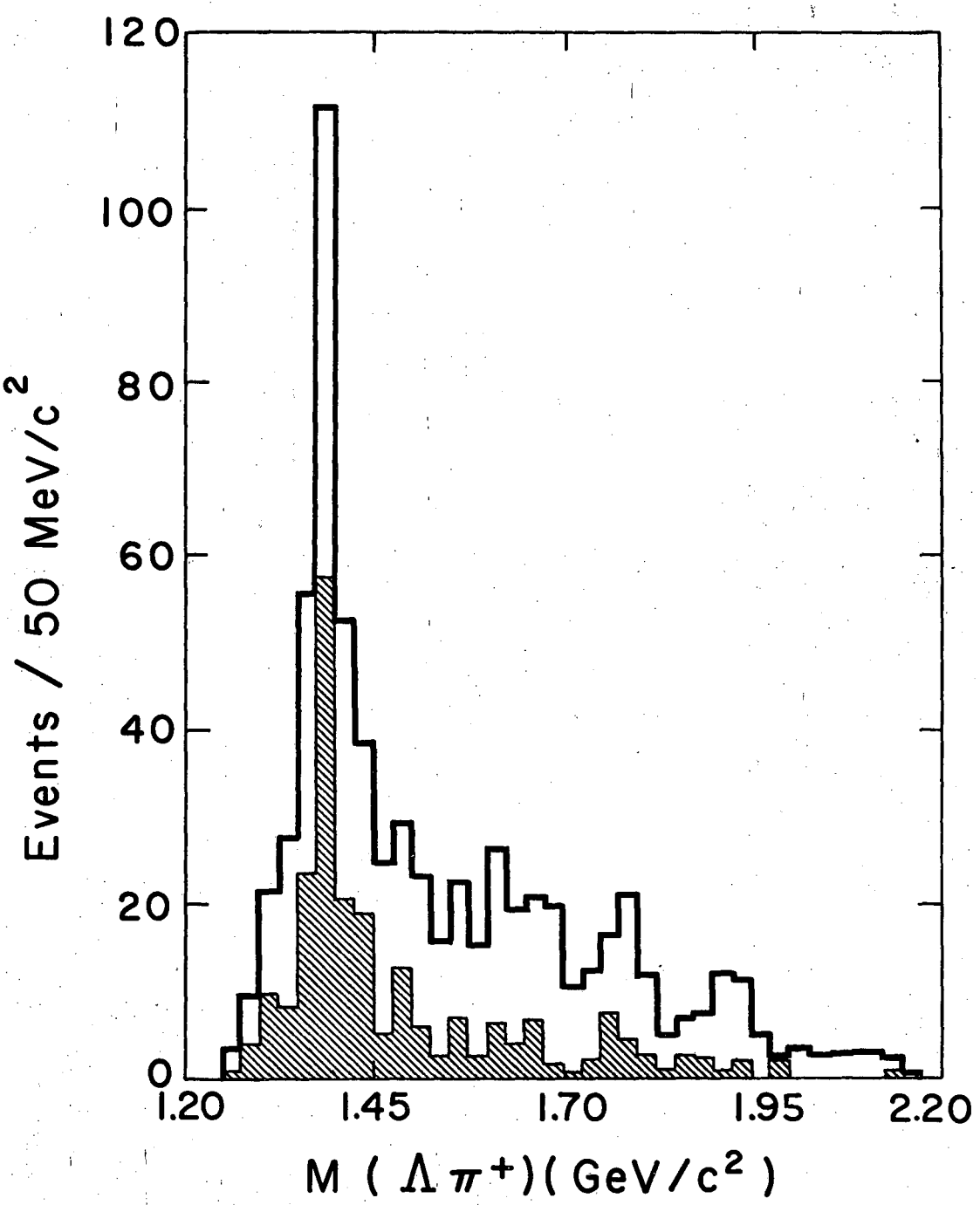


XBL678-3781-A

Fig. 17. Effective mass distribution of $\Lambda\pi^+$ for examples of the reaction $pp \rightarrow \Lambda nK^+\pi^+$. The unshaded histogram is for the total sample. (680 events) The shaded histogram corresponds to the requirement that the cosine of the production angle of the neutron be greater than 0.9. (225 events)

peripheral sample of $pp \rightarrow nY^{*+}K^{+}$. The $Y^{*+}K^{+}$ mass spectrum obtained in this way is given in Fig. 18 . The two selections we have imposed have yielded a sample quite free of background, yet the magnitude of the peak has decreased very little.

We have indicated above that the enhancement we observe is peripherally produced. Of course, another way to see this is in the distribution of the four-momentum transfer to the Y*K system. This $\Delta^2$ distribution , shown in Fig. 19, is for the sample of events with only the selection on $M(\Lambda\pi^{+})$ mentioned above. In order to see if the peripheral nature of Y* production alone could produce an enhancement in the Y*K system, we have parameterized the cross section according to

$$\frac{d^2\sigma}{dm^2 d\Delta^2} = \text{const} \frac{\Delta^2}{(\Delta^2+m_\pi^2)^2} \frac{p}{m} e^{-\alpha\Delta^2}$$

where $\Delta^2$ = four-momentum transfer to the Y*K system,

$m$ = effective mass of Y*K,

$p$ = momentum of the Y* in Y*K center of mass.

The value of $\alpha$ needed to fit the $\Delta^2$ distribution is $0.5 \pm 0.5$ $(\text{BeV/c})^{-2}$. Events were then generated by a Monte Carlo method and the same two selections were imposed on them as on the data. The resultant reflection of this "peripheral phase space" in the Y*K mass spectrum is shown as the smooth curve of Fig. 18. The agreement is very poor and we conclude that a non-resonant phase space which successfully fits the production angular distribution of Y*K is insufficient to account for the enhancement in the Y*K mass spectrum.

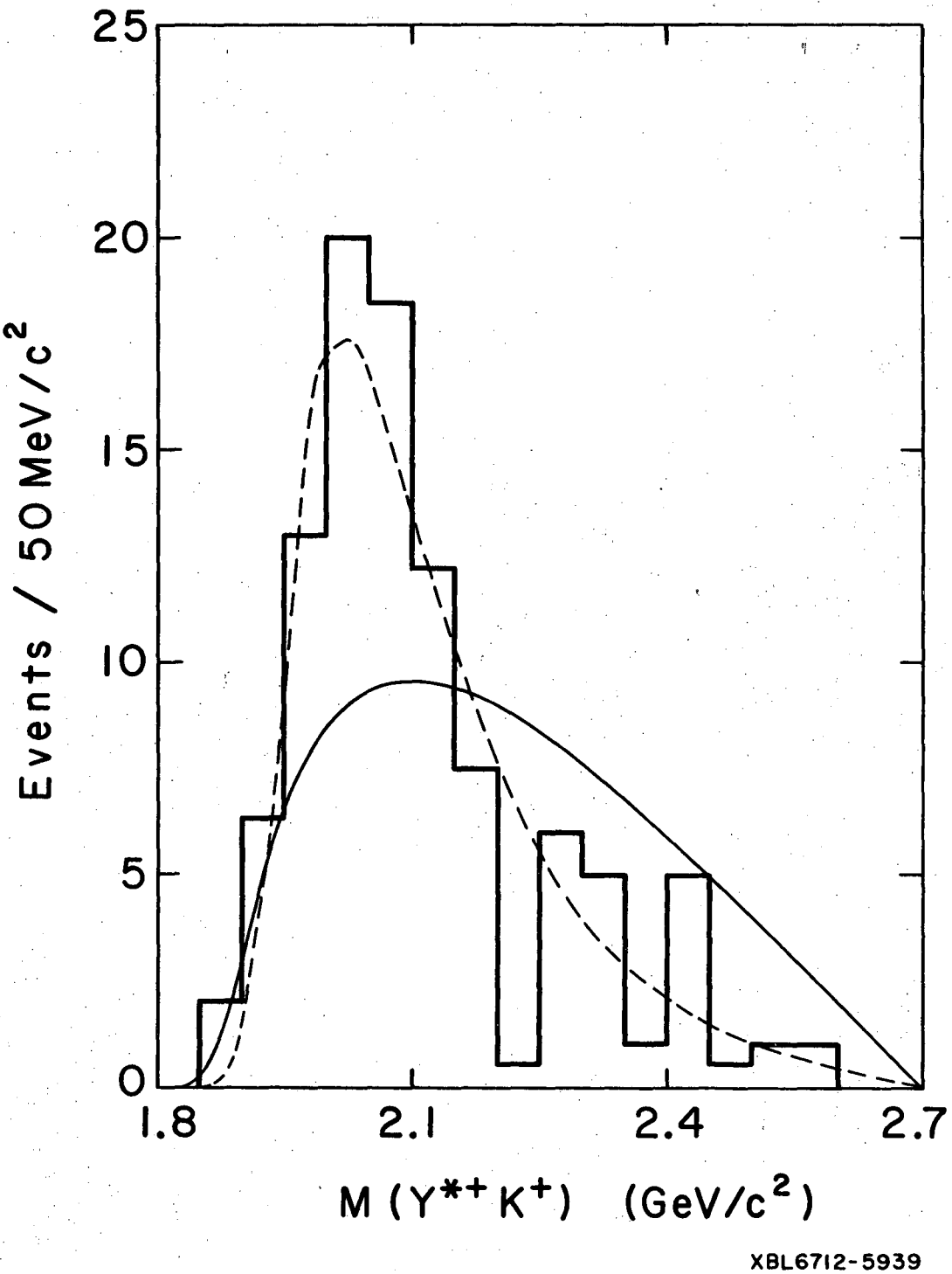


Fig. 18. Effective mass distribution of $Y^{*+}K^{+}$ for examples of the reaction $pp \rightarrow Y^{*+}K^{+}n$ with the requirement that $|\cos \theta_n| \geq 0.0$. (100 events) The curves are discussed in the text.

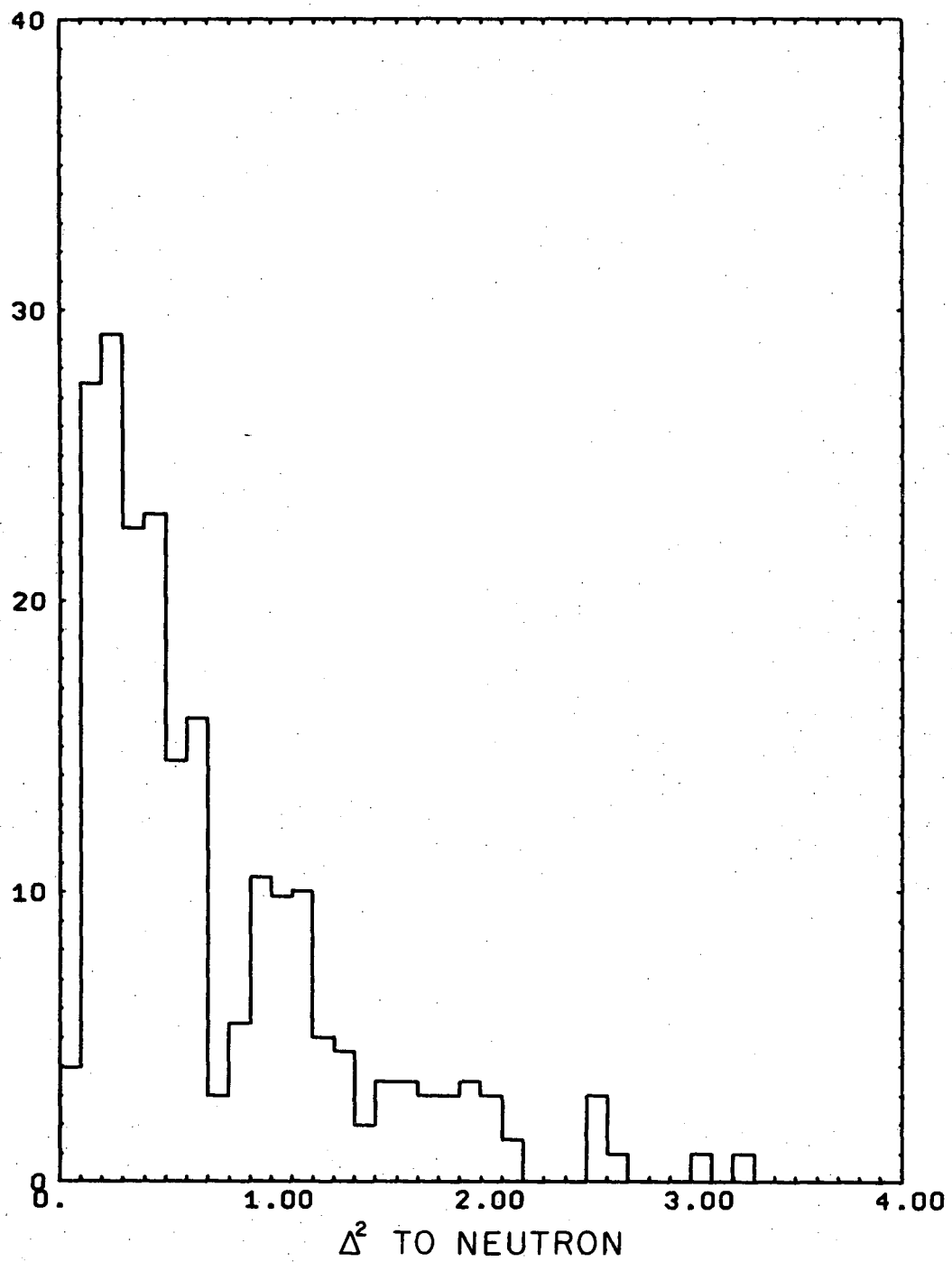


XBL 679-4937

Fig. 19. Distribution of the four-momentum transfer to the neutron for examples of the reaction $pp \rightarrow Y^{*+}K^{+}n$.

We have fitted the Y*K mass spectrum to a sum of resonance and peripheral phase space. For the resonant cross section, we replace the phase space factor $\frac{p}{m}$ in the above equation by

$$\frac{m\Gamma(m)}{(m^2-m_o^2)^2 + m_o^2\,\Gamma_t^2(m)}$$

where $m_o$ nominal resonance mass,

$\Gamma(m)$ = energy-dependent partial width for Y*K decay,

$\Gamma_t(m) = \Gamma_{el}(m) + \Gamma_{in}(m)$ is the total energy-dependent width, the sum of the elastic and total inelastic widths.

We parameterize the energy dependence of the widths by a form first published by Glashow and Rosenfeld[31]

$$m\Gamma(m) \propto \frac{p}{m}\left(\frac{p^2}{p^2+b^2}\right)^{\ell}$$

where p = momentum of Y* in the resonance center of mass

$\ell$ = decay angular momentum. The parameter b is a measure of the inverse of the interaction radius.

Because of the large number of free parameters and the rather small number of events, we are unable to give a precise determination of the resonance parameters. We describe the variation of $\chi^2$ for a fit to the experimental Y*K mass histogram of Fig. 18. We vary the amount of resonance, the nominal resonance mass $m_o$, the total width at resonance, $\Gamma_t(m_o)$, the decay angular momentum $\ell$, and the inverse of the interaction radius b. Except for the case $\ell$=3, where we obtain a satisfactory fit using a mass and width consistent with N*(1950), we assume that $\Gamma_t(m)$ is dominated by the one decay mode N*(1236)$\pi$. For N*(1950) the elastic-

ity is known to be about 0.5, so we use half $N\pi$ and half $N^*(1236)\pi$ decay in the calculation of $\Gamma_t(m)$ in that case. Since the region of mass we fit is quite far above both $N\pi$ and $N^*\pi$ thresholds, the results are insensitive to the relative amounts of their partial widths. Although the best fits are obtained with less than 100% resonance, the fraction of resonance required is consistent with the assumption of pure resonance decay. A value of $0.85 \pm 0.15$ for the resonant fraction is typical. In Table III we present, for fixed values of $\ell$ and b, the best determinations for $m_o$ and $\Gamma_t(m_o)$ and the corresponding $\chi^2$ for the fit. The shifts from these best values assuming only resonance decay are neglible compared to the uncertainties. Furthermore, the answer for the nominal resonance mass does not change if all of the $\Delta^2$ dependence is removed, although slightly narrower widths are obtained as expected. In a maximum likelihood fit to a pure resonance model with no $\Delta^2$ dependence we find, for example, $m_o = 1994$ MeV/$c^2$ and $\Gamma = 190$ MeV/$c^2$ for $\ell = 1$ and b = 350 MeV/c with uncertainties comparable to those given in Table III.

There is some question as to the validity of the above resonance form and energy dependent partial widths in a region far removed from the nominal resonance mass. However, assuming the model is correct, the data are consistent with the values $m_o = 1950$ MeV/$c^2$ and $\Gamma_t(m_o) = 220$ MeV/$c^2$. These are the presently accepted solutions for the resonance parameters of $N^*(1950)$ observed in the $F_{37}$ partial wave in pion-nucleon scattering.[32,33,34] Although several other I=3/2 resonances have been reported in this energy region,[32] $N^*(1950)$ is the only firmly established one. The dashed curve in Fig. 18 is the prediction of our peripheral model assuming 100% resonance decay with $\ell = 3$, b = 0.20 BeV/c, $m_o = 1940$ MeV/$c^2$ and $\Gamma_t(m_o) =$

Table III. Results of fit to $Y^{*+}K^{+}$ mass spectrum.

| Decay Angular Momentum $\ell$ | b | Resonance Mass $m_o$ | Total Width $\Gamma_t(m_o)$ | $\chi^2$ for 4 Constraints |
|---|---|---|---|---|
| 0 | | 2035 ± 20 | 200 ± 50 | 0.1 |
| 1 | .20 | 2010 ± 25 | 240 ± 70 | 1.1 |
| | .35 | 1990 ± 25 | 230 ± 70 | 2.1 |
| 2 | .20 | 1980 ± 35 | 230 ± 70 | 2.1 |
| | .35 | 1930 ± 35 | 200 ± 70 | 3.7 |
| 3 | .20 | 1940 ± 55 | 190 ± 45 | 3.1 |
| | .35 | 1850 ± 55 | 70 ± 45 | 7.9 |

190 MeV/$c^2$.

Unlike N*(1236), we do not expect N*(1950) to be cleanly produced, i.e. free of overlap and/or interference with other amplitudes. The $\Gamma_{1950}(m_o)$ is about twice as large as $\Gamma_{1236}(m_o)$ and there is an I=1/2 resonance at 2190 MeV/$c^2$ which may overlap with the N*(1950). From our analysis given in Section V, we believe pion exchange to be an accurate description of the production of N*(1950). The corresponding $\pi p \to Y^*K$ cross sections used in that calculation are displayed in Figs. 21, 22, and 23. These indicate that a single I=3/2 resonant amplitude is insufficient fordescribing the $\pi^- p$ data in the relevant energy range although the $\pi^+ p$ data are in excellent agreement with this assumption. It appears that all of the $\pi p \to Y^*K$ data can be fitted by a sum of I=3/2 resonant and non-resonant amplitudes and an I= 1/2 background, although much more data and a detailed partial wave analysis is needed for conclusive proof. For these reasons, we do not attempt to determine the "amount" of N*(1950) in the two channels $\Lambda K^o p\pi^+$ and $\Lambda K^+ p\pi^o$. We estimate the cross section for $pp \to N^{*++}(1950)$, $N^{*++}(1950) \to Y^{*+}K^+$ to be 13 ± 2 μb. Further discussion of $SU_3$ predictions for N*(1950) is given in Section VI.

## V. ONE-PION EXCHANGE

We have indicated above that a simple phase space model fails to describe certain aspects of the data which are sensitive to both the production and decay distributions of the resonances. Although several single particle exchange processes can contribute to the amplitudes which describe each final state, we make the assumption that only pion exchange is present and do not consider other processes such as kaon exchange. We now describe our formulation of this model which we find adequate to describe almost all features of the data.

In Figs. 20(a) and 20(b) we have drawn the two possible single pion exchange diagrams which we assume to be the only contributors to the amplitude. Of the two diagrams, (a) requires fewest assumptions for the calculation since the vertices involve only two-body scattering processes. The $N\pi$ cross sections are known very well and the $\Lambda K$ cross section is fairly well studied. For diagram (b) we separate the $\pi p \to \Lambda K \pi$ vertex into the two two-body diagrams shown in (c) and (d) and the three-body diagram (e), assuming that the only resonances produced are K*(890) and Y*(1385). This assumption has been made when we unfold the experimental cross sections. We discuss this below. The cross section for a final state is then calculated as an incoherent sum of squares of the corresponding amplitudes for the four diagrams (a), (c), (d), and (e). Since there are two identical Fermions in the initial state there are really two sets of diagrams, related by interchange of the two initial state protons, which contibute to the cross section. We assume that the cross section can be calculated neglecting the interference term in which case the cross section is just twice that for the single set of diagrams.

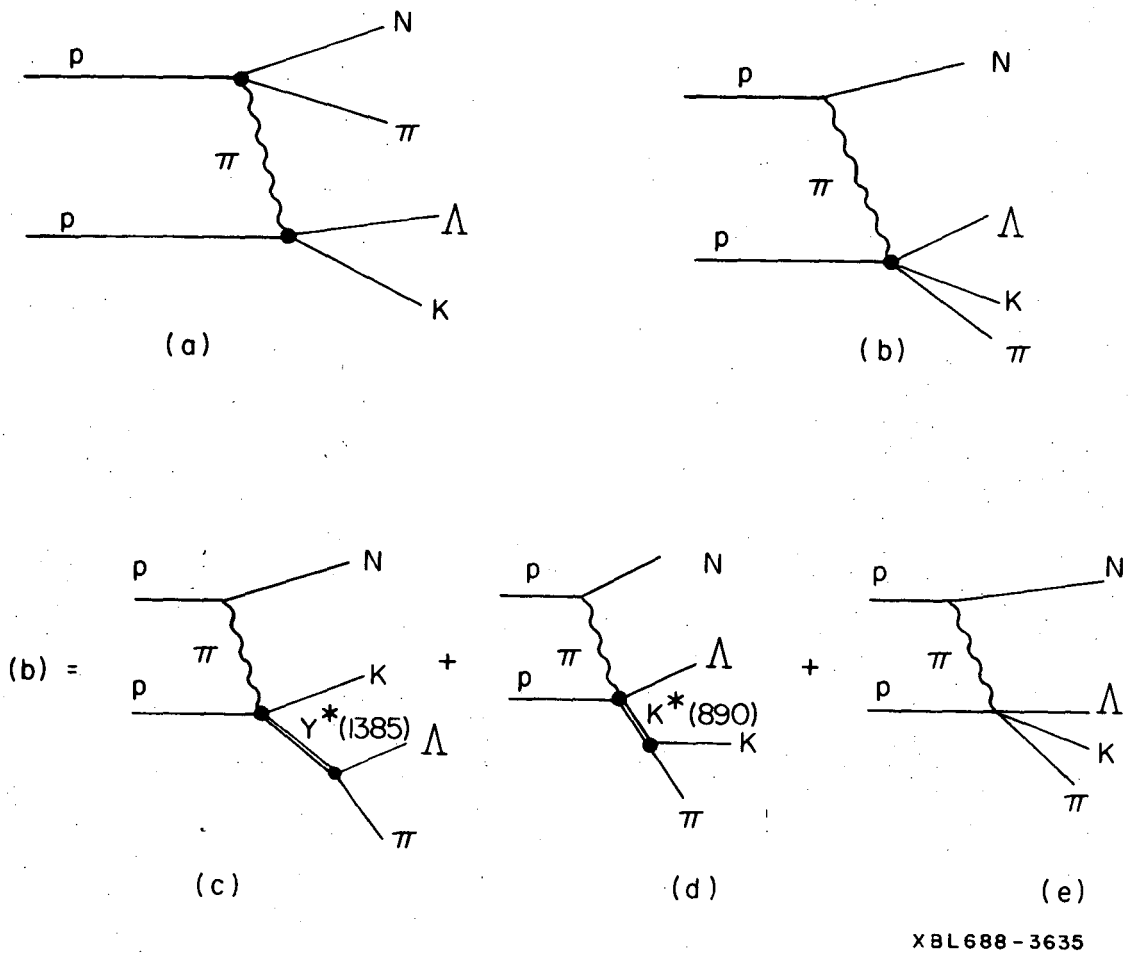


Fig. 20. One-pion exchange diagrams used in the calculation. These are explained in the text.

For the calculation of the diagram 20(a) we follow Salzman and Salzman.[35] As in all calculations involving virtual pions, there is some arbitrariness as to how to relate the virtual pion cross section to the real pion cross section. We make the assumption that both of the virtual pion cross sections can be replaced by the real pion cross sections at the same total energy. We have calculated the cross section according to

$$\frac{d^7\sigma}{dm^2_{N\pi}dm^2_{\Lambda K}dtd\cos\theta_{N\pi}d\phi_{N\pi}d\cos\theta_{\Lambda K}d\phi_{\Lambda K}} = \frac{1}{16\pi^3}\frac{1}{(\bar{p}\bar{E})^2}\frac{1}{(t+\mu^2)^2}\frac{d\sigma_{N\pi}}{d\Omega_{N\pi}}k_{N\pi}m_{N\pi} \cdot \frac{d\sigma_{\Lambda K}}{d\Omega_{\Lambda K}}k_{\Lambda K}m_{\Lambda K}$$

$m_{N\pi}$ and $m_{\Lambda K}$ are the effective masses of the pairs of particles.

$t$ is the four-momentum transfer squared between the initial proton and the $N\pi$ system.

$\theta_{N\pi}$ is the angle between the initial proton and the final state nucleon in the $N\pi$ rest system and

$\phi_{N\pi}$ is the corresponding azimuthal angle of the nucleon about the initial proton direction.

$\theta_{\Lambda K}$ and $\phi_{\Lambda K}$ are defined in the same way as $\theta_{N\pi}$ and $\phi_{N\pi}$.

$\bar{p}$ and $\bar{E}$ are the momentum and energy of either initial state proton in the overall center of mass.

$\frac{d\sigma_{N\pi}}{d\Omega_{N\pi}}$ and $\frac{d\sigma_{\Lambda K}}{d\Omega_{\Lambda K}}$ are the experimental differential cross sections for $\pi p \to \pi N$ and $\pi p \to \Lambda K$ respectively.

$k_{N\pi}$ and $k_{\Lambda K}$ are the momenta of real pions in the center of mass for the reactions $\pi p \to \pi N$ and $\pi p \to \Lambda K$ at energies $m_{N\pi}$ and $m_{\Lambda K}$.

The experimental $\pi p \to \pi N$ cross sections we use are calculated from the phase shifts of Lovelace's analysis.[32] In the energy range needed for our four-body states, these cross sections are dominated by N*(1236) production. The various $\pi p \to \Lambda K$ differential cross sections we use are taken from reports listed in reference 36.

There are seven independent variables needed to describe the most general four-body final state for fixed center-of-mass energy and we have written all differential cross sections indicating the seven variables we use in a Monte Carlo calculation. The details are given in Appendix B.

For the process describing Y*(1385) production we use the following cross section

$$\frac{d^7\sigma}{dm^2_{\Lambda\pi}\,dw^2\,dt\,d\cos\theta_{\Lambda\pi}\,d\phi_{\Lambda\pi}\,d\cos\theta_{\Lambda}\,d\Phi_{\Lambda}} =$$

$$\frac{G^2}{4\pi}\,\frac{1}{16\pi}\,\frac{e^{-\alpha(t+m_\pi^2)}}{(t+m_\pi^2)^2}\,t\,\frac{1}{(\bar{p}\bar{E})^2}\,kw\,\frac{d\sigma_{Y^*}}{d\Omega}(w,\theta_{Y^*})\,\frac{p_\Lambda}{m_{\Lambda\pi}}\,\frac{p_{\Lambda\pi}}{(m^2_{\Lambda\pi}-m_o^2)^2+m_o^2\Gamma^2}\cdot y(w)$$

where

$$\frac{1}{y(w)} = \int_{(m_\Lambda+m_\pi)^2}^{(w-m_k)^2} \frac{4\pi\, p_{\Lambda\pi}\, p_\Lambda}{m_{\Lambda\pi}\left[(m^2_{\Lambda\pi}-m_o^2)^2 + m_o^2\Gamma^2\right]}\, dm^2_{\Lambda\pi}$$

$\frac{G^2}{4\pi}$ = 15 for $\pi^o$ exchange, = 30 for $\pi^+$ exchange.

$w$ = effective mass of $\Lambda K\pi$ system.

$k$ = c.m. momentum of a real pion in the initial state for $\pi p \to \Lambda K\pi$ at total energy w.

$t$ = four-momentum transfer between initial state proton and final state nucleon.

$\theta_{\Lambda\pi}$ and $\phi_{\Lambda\pi}$ are the angles describing the $\Lambda\pi$ system defined in the

$\Lambda K\pi$ rest system.

$\theta_\Lambda$ and $\phi_\Lambda$ are the angles describing the $\Lambda$ in the $\Lambda\pi$ rest system.

$\frac{d\sigma_{Y^*}}{d\Omega}(w,\theta_{Y^*})$ = differential cross section for Y*(1385) production at total energy w.

$p_{\Lambda\pi}$ = momentum of the $\Lambda\pi$ system in the $\Lambda K\pi$ rest system.

$p_\Lambda$ = momentum of the $\Lambda$ in the $\Lambda\pi$ rest system.

$m_o$ and $\Gamma_o$ = 1.385 BeV/$c^2$ and 0.040 BeV/$c^2$, respectively.

The factor $e^{-\alpha(t+m_\pi^2)}$ is needed to obtain agreement with the four-momentum transfer distribution in the $nY^{*+}K^+$ final state and we find $\alpha = 1.0\ (\text{BeV/c})^{-2}$ adequate for all three final states.

The momentum dependence for the Y* decay we have used may not be the best, but since the Y* is narrow it does not matter. As indicated in the cross section, we assume a uniform decay angular distribution for the $\Lambda$ in the $\Lambda\pi$ rest frame.

The data for $\pi p \to Y^*K$ are sparse. Except for $\pi^- p \to Y^{*o}K^o$ at 2 BeV/c, no production angular distributions are published.[37] Therefore, we have used the total Y* production cross sections with production angular distributions taken from our own data assuming pion exchange. For the relevant energy region, we find excellent agreement with Hardy's angular distribution.

We have fitted the total $\pi p \to \Lambda K\pi$ cross sections to a sum of Y*(1385), K*(890), and background. All of the $\pi^- p$ data are from the compilation of Hardy[37] and the $\pi^+ p$ data are taken from the reports listed in reference.[38] Our fits to the data are drawn in Figures 21, 22, and 23. The procedure we have used to obtain these fits is as follows. First,

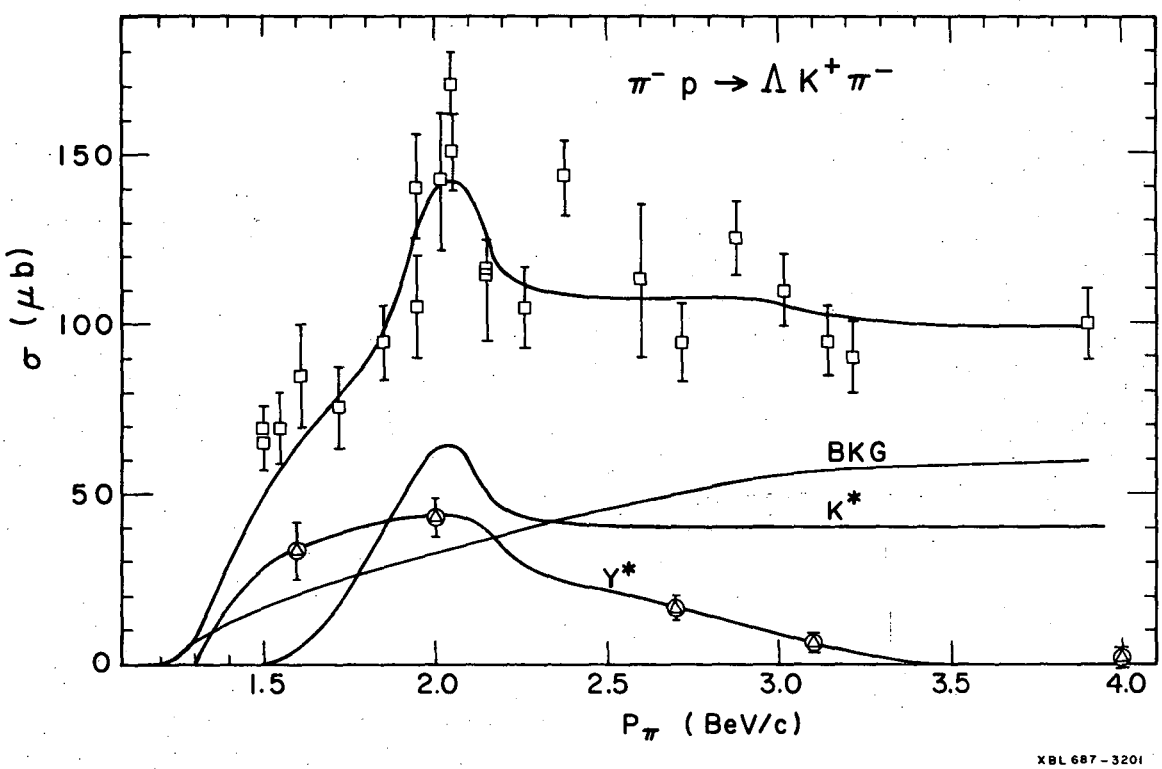


Fig. 21. Cross section for the reaction $\pi^- p \rightarrow \Lambda K^+ \pi^-$ as a function of beam momentum. Boxes are for total cross section, inscribed triangles are $Y^{*-}(1385)K^+$ cross sections. The curves are described in the text.

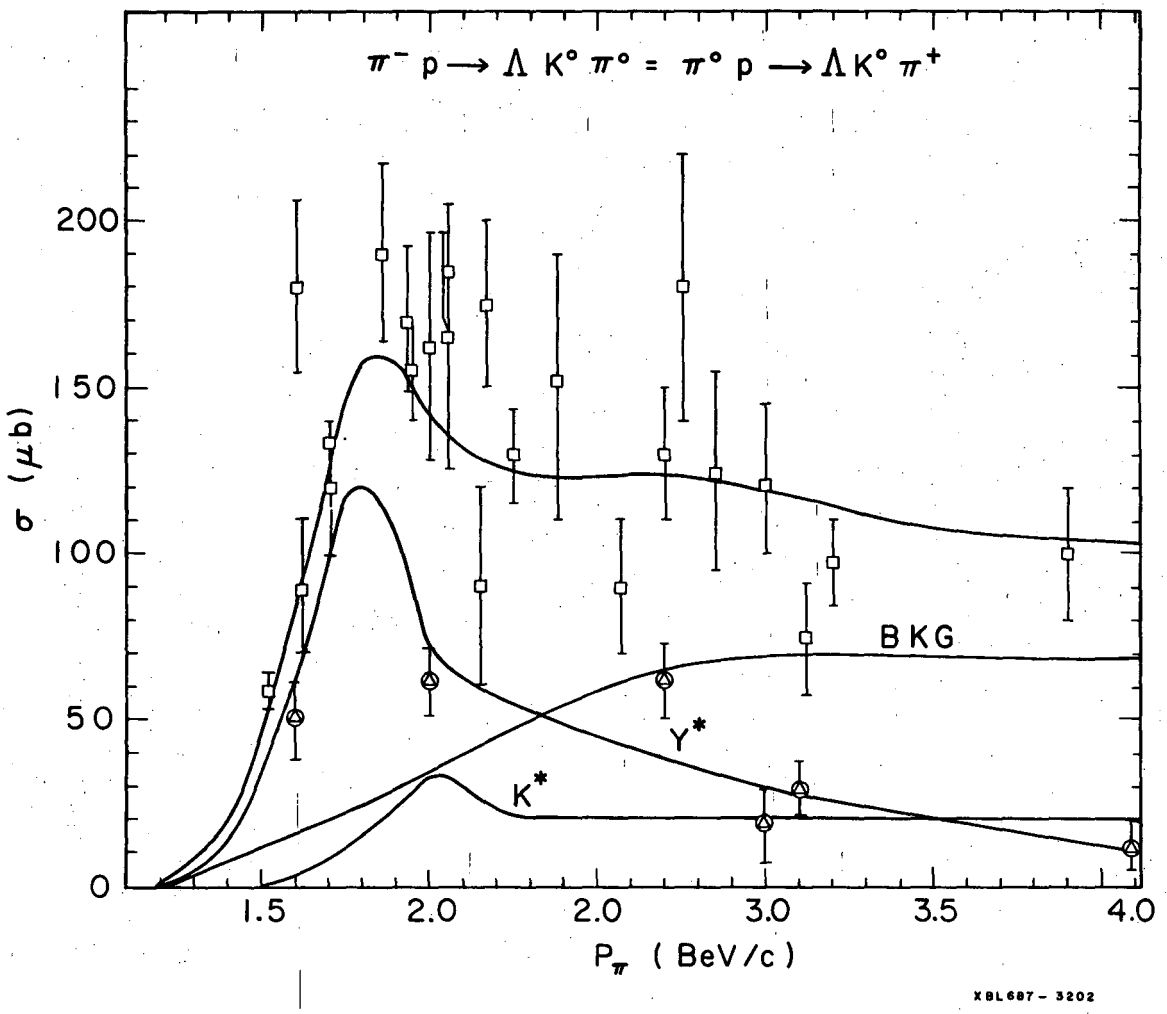


Fig. 22. Cross section for the reaction $\pi^- p \rightarrow \Lambda K^\circ \pi^\circ$ as a function of beam momentum. Boxes are for total cross section, inscribed triangles are $Y^{*\circ}(1385)K^\circ$ cross section. The curves are described in the text.

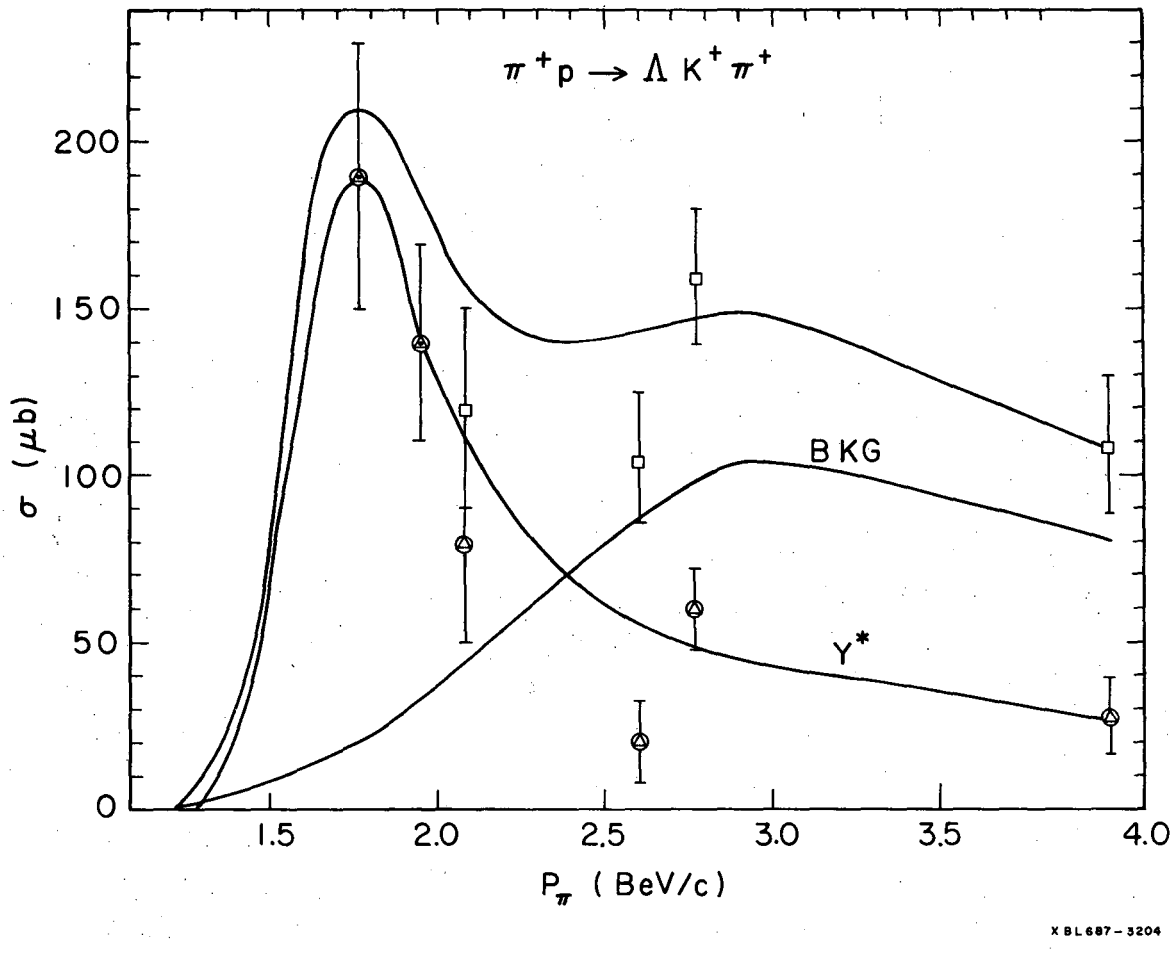


Fig. 23. Cross section for the reaction $\pi^+ p \rightarrow \Lambda K^+ \pi^+$ as a function of beam momentum. Boxes are for total cross section, inscribed triangles are $Y^{*+}(1385)K^+$ cross sections. For the first two data points, the data are reported to be completely $Y^{*+}(1385)K^+$ production. The curves are described in the text.

the $\pi^- p \to \Lambda K^+ \pi^-$ and $\pi^- p \to \Lambda K^o \pi^o$ total cross section data were fit by eye with the curves shown in Figs. 21 and 22, respectively. (These data are represented by the boxes.) Next, the $\pi^- p \to Y^{*-}(1385) K^+$ cross section was fit by eye with the curve passing through the inscribed triangles of Fig. 21. Then, assuming the non-resonant $\pi^- p \to \Lambda K^+ \pi^-$ background cross section to be smoothly rising from threshold, we obtain the $\pi^- p \to \Lambda K^*(890)$, $K^*(890) \to K^+ \pi^-$ cross section by subtraction. Having determined this $K^*(890)$ cross section from Fig. 21, we invoke isotopic spin invariance to obtain the $K^*$ cross sections for the reaction $\pi^- p \to \Lambda K^+ \pi^-$, which is just half that for the $\pi^- p \to \Lambda K^+ \pi^-$ reaction. This fit for $K^{*o}(890)$ production is in good agreement with the $\pi^- p \to \Lambda K^{*o}(890)$ data shown in Fig. 24. Finally, again assuming the non-resonant $\pi^- p \to \Lambda K^o \pi^o$ background cross section to be smoothly rising from threshold, we obtain the $\pi^- p \to Y^{*o}(1385) K^o$ cross section by subtraction. The curve obtained in this way agrees fairly well with the $\pi^- p \to Y^{*o}(1385) K^o$ data indicated by the inscribed triangles of Fig. 22. Although no measurement of the $Y^{*o} K^o$ cross section is published at 1.8 BeV/c, Miller has indicated the reaction is indeed dominated by $Y^*(1385)$ production. The $\pi^+ p \to \Lambda K^+ \pi^+$ data were fit again assuming that the non-resonant background cross section is smoothly rising from threshold. The $Y^*$ curve obtained is in good agreement with the $\pi^+ p \to Y^{*+}(1385) K^+$ data points indicated by the inscribed triangles in Fig. 23. These $\pi^+ p$ data indicate that $Y^*$ production drops sharply as the momentum increases. These data, as we mentioned in Section IV B, are also consistent with the assumption that $N^*(1950)$ dominates $Y^{*+} K^+$ production.

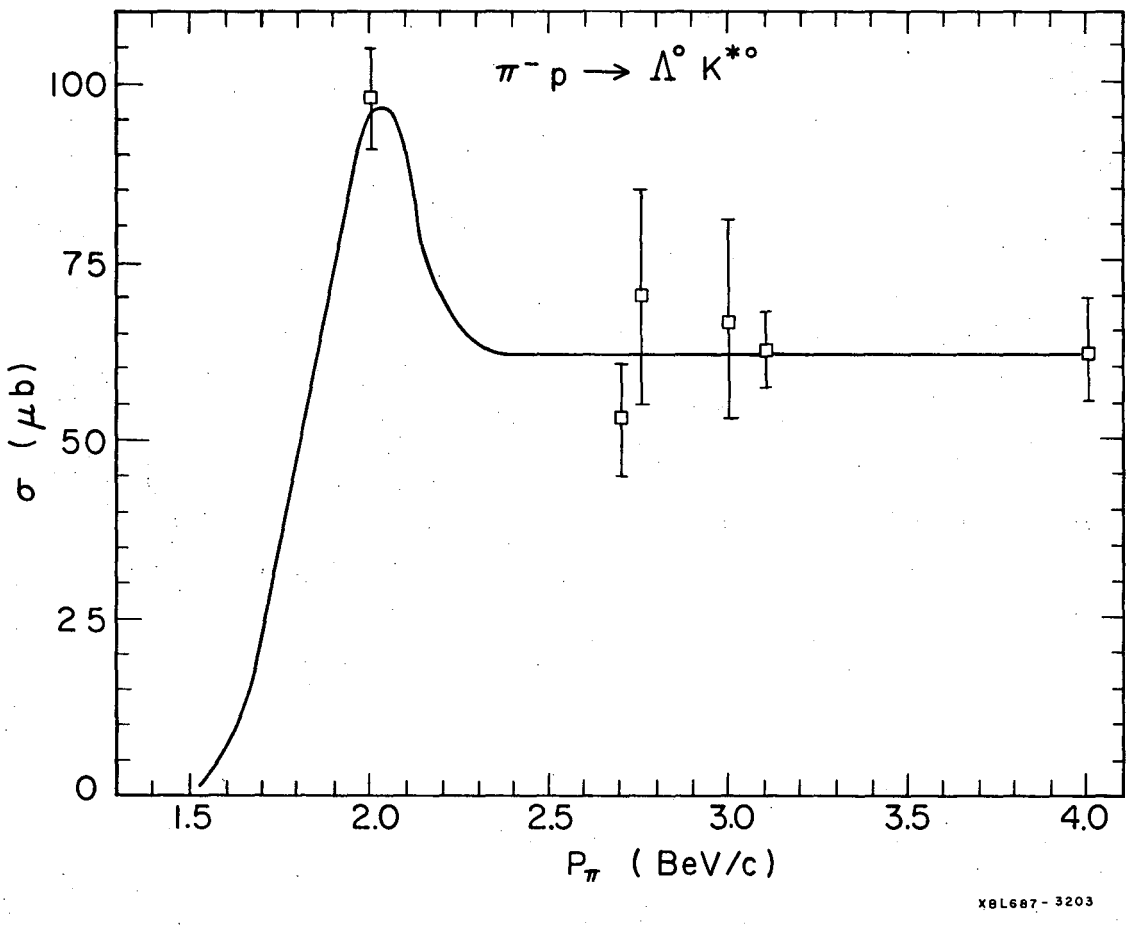


Fig. 24. Cross section for the reaction $\pi^- p \rightarrow \Lambda K^{*0}$ as a function of beam momentum. The curve is described in the text.

Our model for K*(890) is identical to the one just discussed for Y*(1385). The only difference is that we use the experimental differential cross sections interpolating linearly between data points. The factor $e^{-\alpha(t+m_\pi^2)}$ is also omitted in the calculation. We use $m_o = 890$ MeV/$c^2$ and $\Gamma = 50$ MeV/$c^2$ for the resonance parameters.

To describe the non-resonant background, we assume $\pi p \to \Lambda K \pi$ to be described by phase space and use isotropic production distributions for each of three particles. This assumption is clearly not valid at high values of $\Lambda K \pi$ mass and also neglects the low mass $\Lambda K$ interaction which is probably present. The cross section we use is then

$$\frac{d^7\sigma}{dm_{\Lambda\pi}^2 dw^2 dt d\cos\theta_{\Lambda\pi} d\phi_{\Lambda\pi} d\cos\theta_\Lambda d\phi_\Lambda} = \frac{G^2}{4\pi}\frac{1}{16\pi}\frac{t}{(t+m_\pi^2)^2}\frac{1}{(\bar{p}\bar{E})^2} kw\sigma(w) p_{\Lambda\pi}\frac{p_\Lambda}{m_{\Lambda\pi}} A(w)$$

where

$$\frac{1}{A(w)} = 16\pi^2 \int_{(m_\Lambda+m_\pi)^2}^{(w-m_k)^2} \frac{p_{\Lambda\pi}\, p_\Lambda}{m_{\Lambda\pi}}\, dm_{\Lambda\pi}^2$$

$\sigma(w)$ is the background $\pi p \to \Lambda K \pi$ cross section at total energy w. The other definitions are the same as before.

For the $\Lambda K^o p \pi^+$ final state, we use $\pi^- p \to \Lambda K^o \pi^o$ cross sections which are identically equal to the $\pi^o p \to \Lambda K^o \pi^+$ cross sections. The final state $\Lambda K^+ p \pi^o$ requires $\pi^o p \to \Lambda K^+ \pi^o$ cross sections. Isotopic spin invariance relates this to physical cross sections viz

$$\sigma(\pi^o p \to \Lambda K^+ \pi^o) = \frac{1}{2}\left[\sigma(\pi^+ p \to \Lambda K^+ \pi^+) + \sigma(\pi^- p \to \Lambda K^+ \pi^-) - \sigma(\pi^- p \to \Lambda K^o \pi^o)\right].$$

Unfortunately, none of the experimental cross sections are known accurately and we therefore expect even larger errors in this $\pi^o p \to \Lambda K^+ \pi^o$ cross section since subtraction of two comparable numbers is involved.

We have fitted the data for each final state by fitting to the $N\pi$, $\Lambda\pi$, and $K\pi$ mass distributions as described in Section IV. The relative intensities for the different processes are in excellent agreement with the relative intensities found in the phase space fit. The absolute predictions of the models we use are not in agreement with our measured cross sections. These predictions are given in Table IV. Since one can introduce form factors which do not significantly alter the shapes of distributions, but result in rather different total cross sections, we do not take this discrepancy as evidence of failure of the model.

We now compare our experimental distributions with the pion exchange model. All calculations of experimental quantities, such as scattering angles, which involve an initial state proton in the calculation were made assuming that the proton with the smallest $\Delta^2$ to a particular system is at the same vertex as that system. This same selection was included in the Monte Carlo calculations and we find less than 15% of the Monte Carlo events were interpreted differently from their generation. In Figs. 25 through 34 we display the six two-body and the four three-body effective mass distributions for $\Lambda pK^0\pi^+$. In Figs. 39 through 48 we show the ten effective mass distributions for $\Lambda pK^+\pi^0$ and in Figs. 52 through 61 the masses for the $\Lambda nK^+\pi^+$ final state. In all of our histograms we include the pion-exchange prediction with each contribution separately shown and labelled. The relative intensities for the different processes are determined from the likelihood fit and are held fixed in all plots for a given final state.

The overall agreement is best for the $\Lambda pK^0\pi^+$ final state. This is

Table IV. One-pion exchange predicted cross sections for $pp \rightarrow \Lambda NK\pi$ at 6 BeV/c.

| | Y*(1385) | N*(1236) | K*(890) | Background |
|---|---|---|---|---|
| $\Lambda pK^o\pi^+$ | 15 μb(with form factor)<br>41 μb(no form factor) | 42 μb | 28 μb | 34 μb |
| $\Lambda pK^+\pi^o$ | 8 μb(with form factor)<br>22 μb(no form factor) | 11 μb | 14 μb | 20 μb |
| $\Lambda nK^+\pi^+$ | 48 μb(with form factor)<br>130 μb (no form factor) | 6μb | | 46 μb |

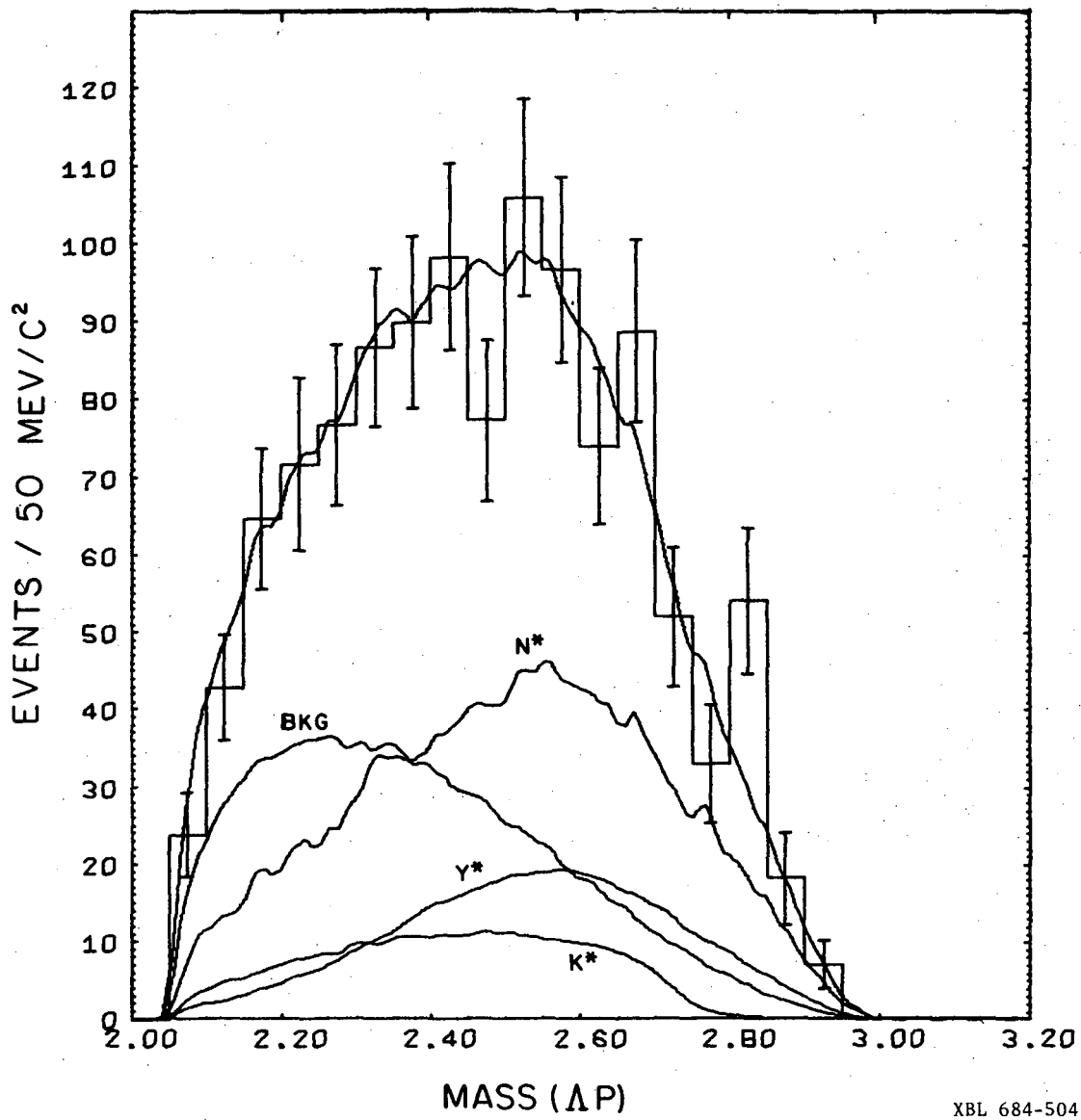


Fig. 25. Effective mass distribution of $\Lambda p$ for examples of the reaction $pp \rightarrow \Lambda p K^{o} \pi^{+}$ (1170 events). The curves are pion-exchange predictions and are described in the text.

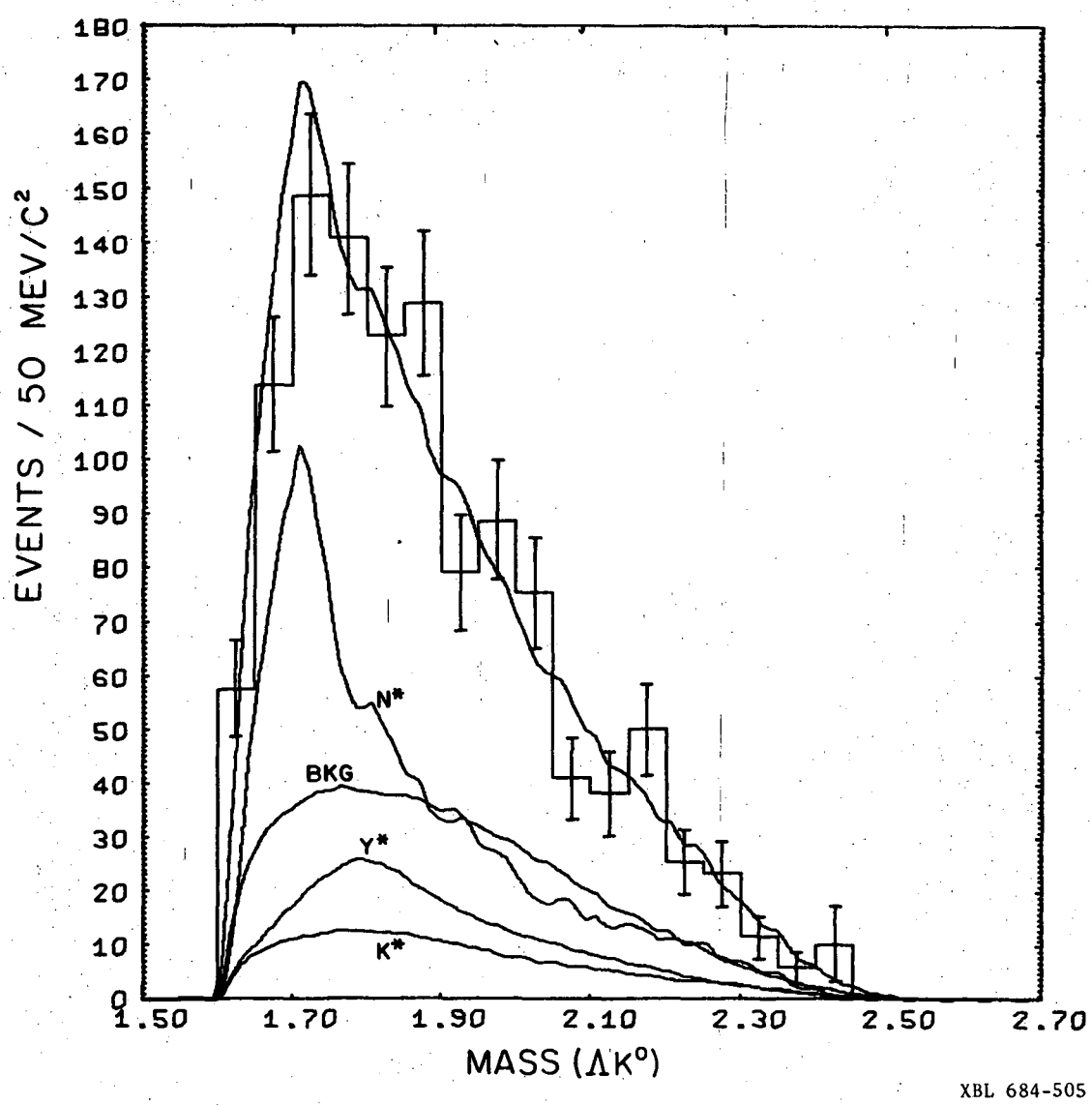


Fig. 26. Effective mass distribution of $\Lambda K^{o}$ for examples of the reaction $pp \rightarrow \Lambda p K^{o} \pi^{+}$ (1170 events). The curves are pion-exchange predictions and are described in the text.

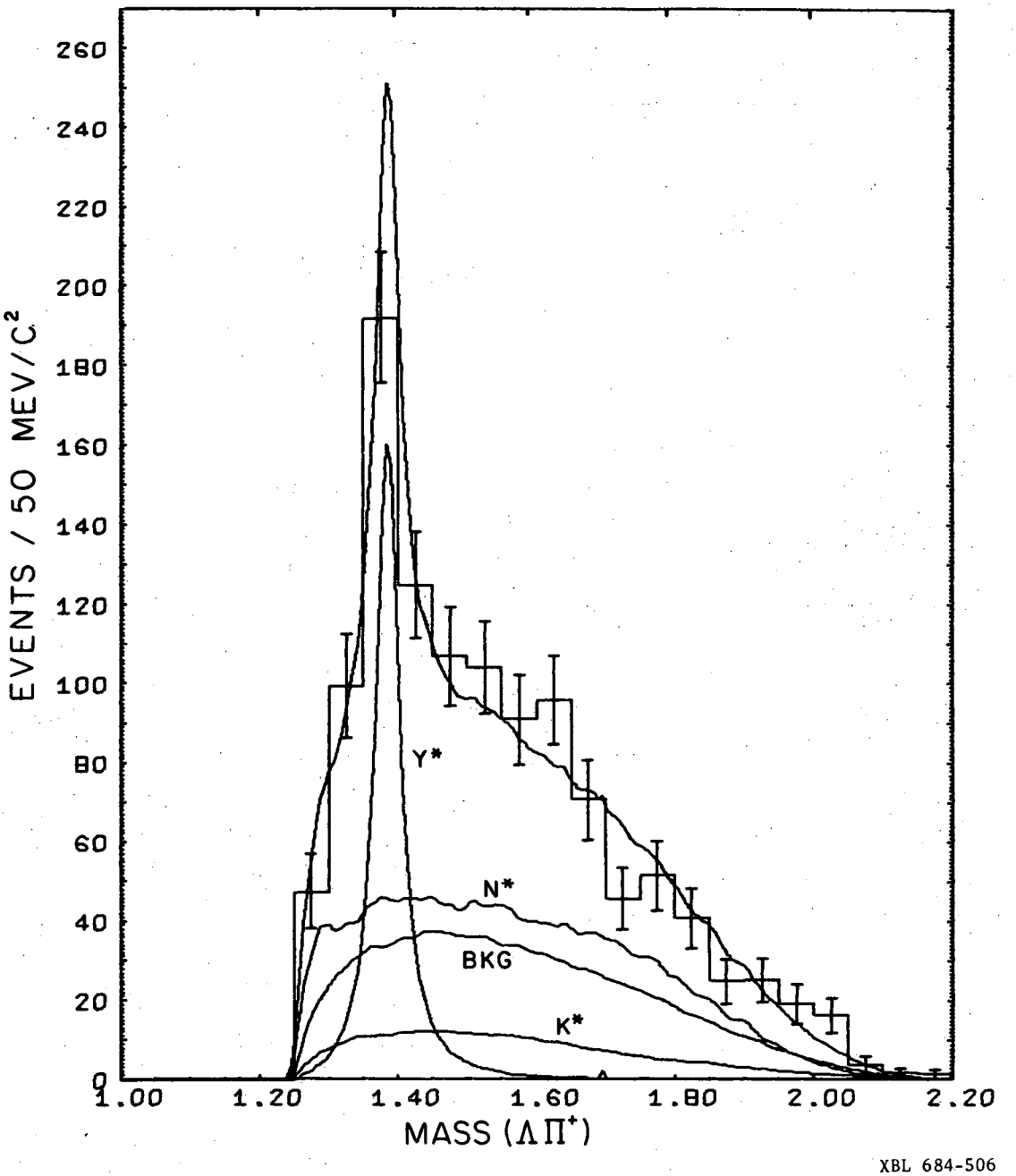


Fig. 27. Effective mass distribution of $\Lambda\pi^+$ for examples of the reaction $pp \rightarrow \Lambda pK^o\pi^+$ (1170 events). The curves are pion-exchange predictions and are described in the text.

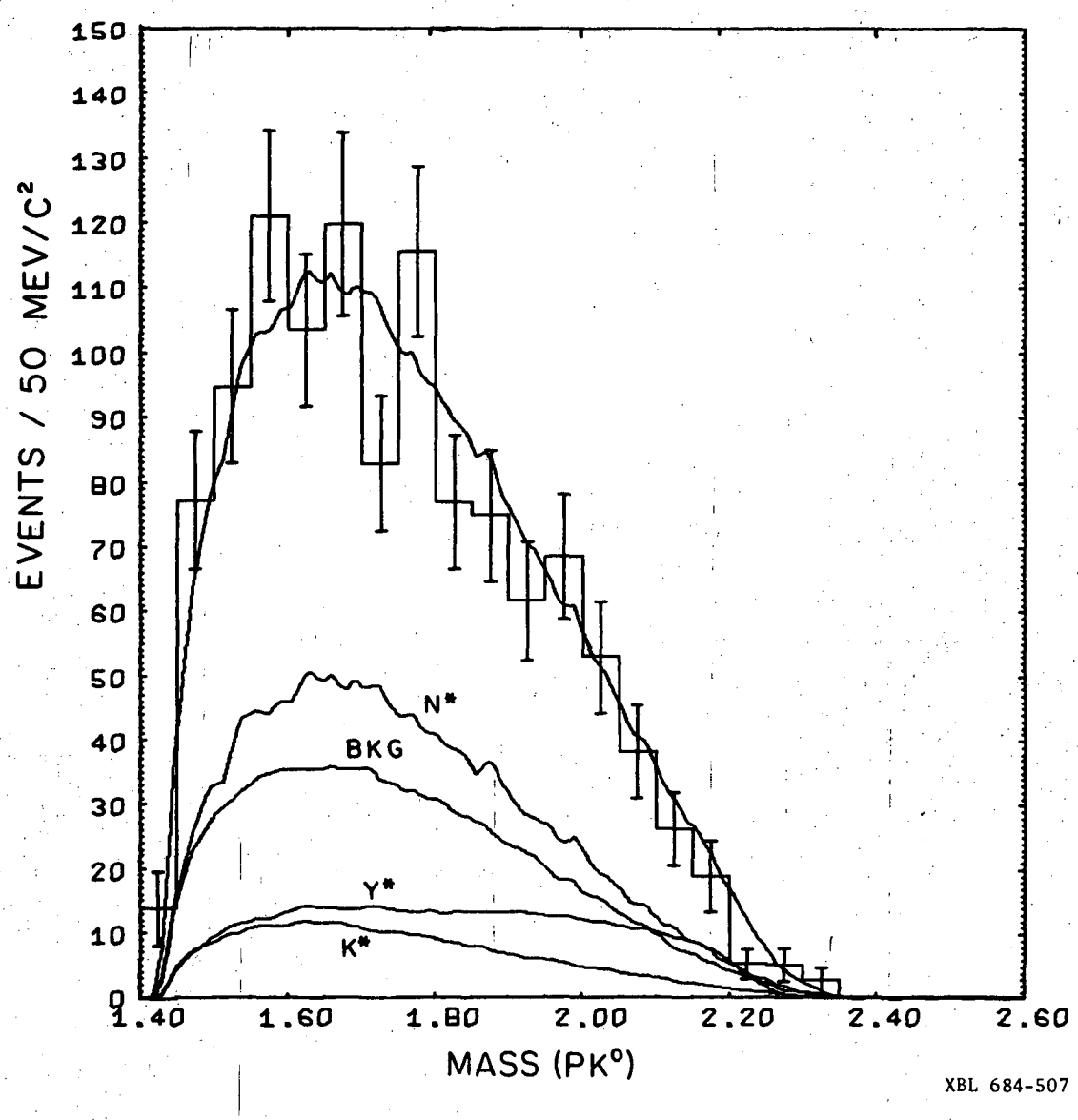


Fig. 28. Effective mass distribution of $pK^{o}$ for examples of the reaction $pp \rightarrow \Lambda pK^{o}\pi^{+}$ (1170 events). The curves are pion-exchange predictions and are described in the text.

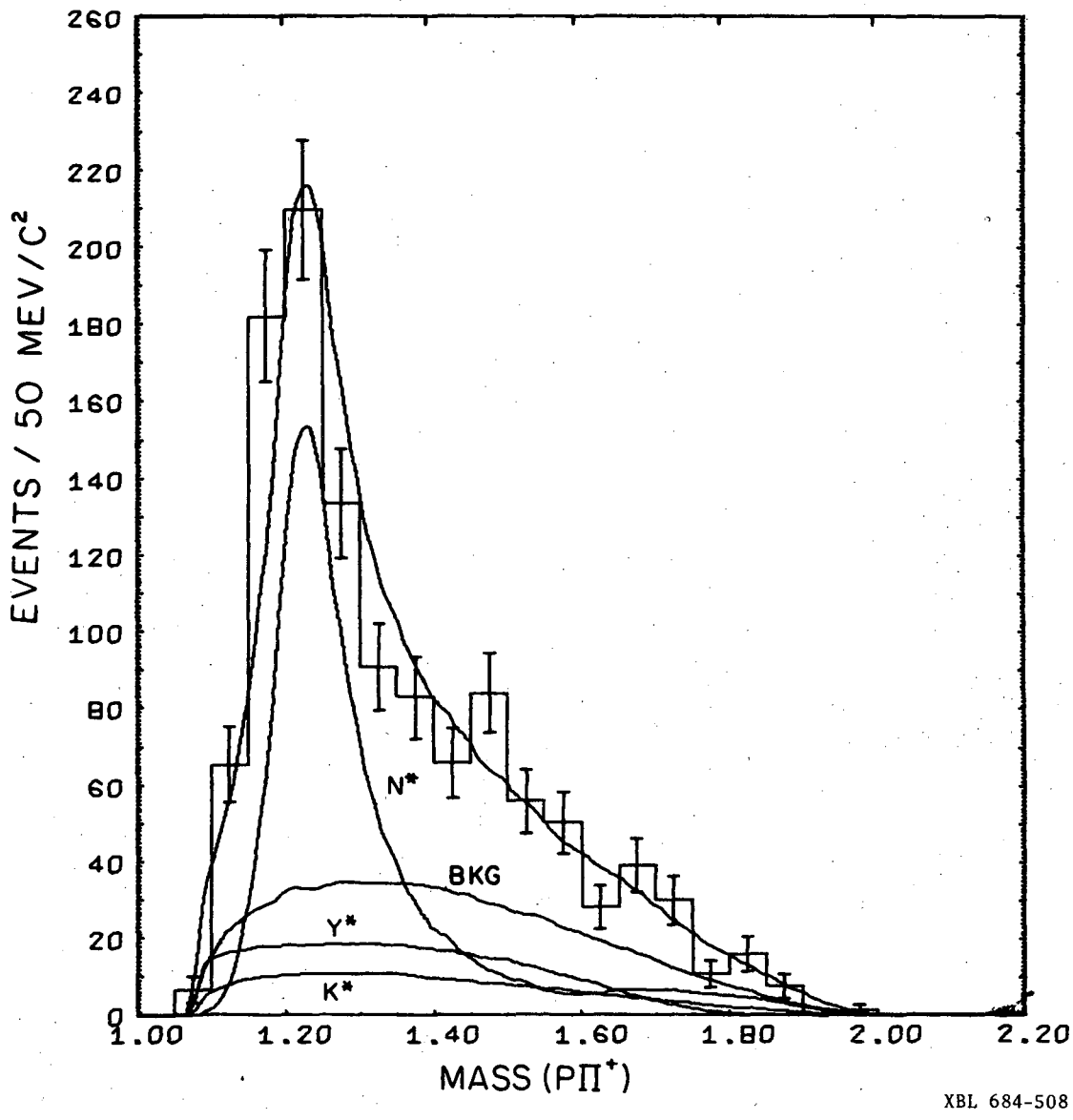


Fig. 29. Effective mass distribution of $p\pi^+$ for examples of the reaction $pp \rightarrow \Lambda p K^0 \pi^+$ (1170 events). The curves are pion-exchange predictions and are described in the text.

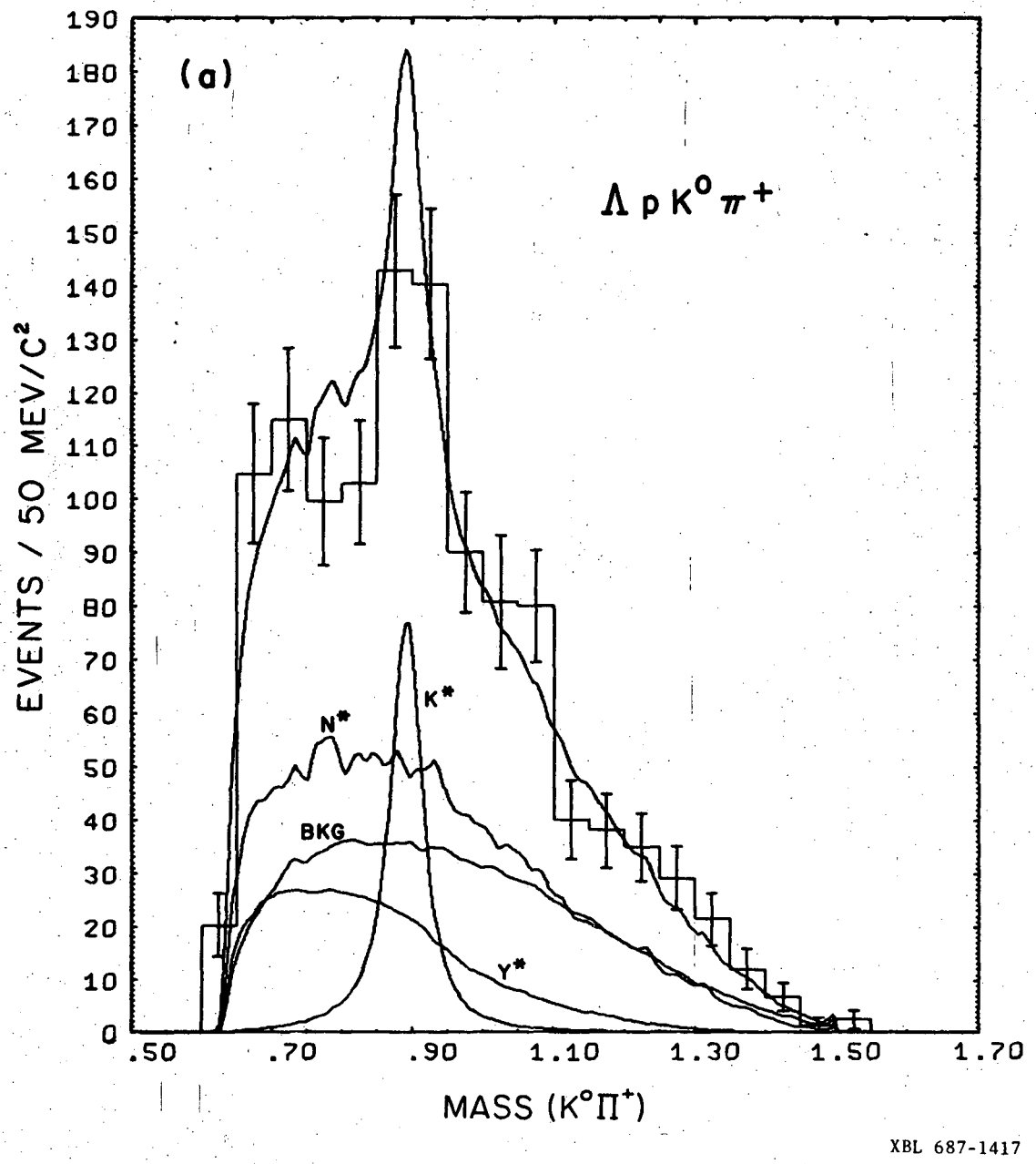


Fig. 30. Effective mass distribution of $K^{o}\pi^{+}$ for examples of the reaction $pp \rightarrow \Lambda pK^{o}\pi^{+}$ (1170 events). The curves are pion-exchange predictions and are described in the text.

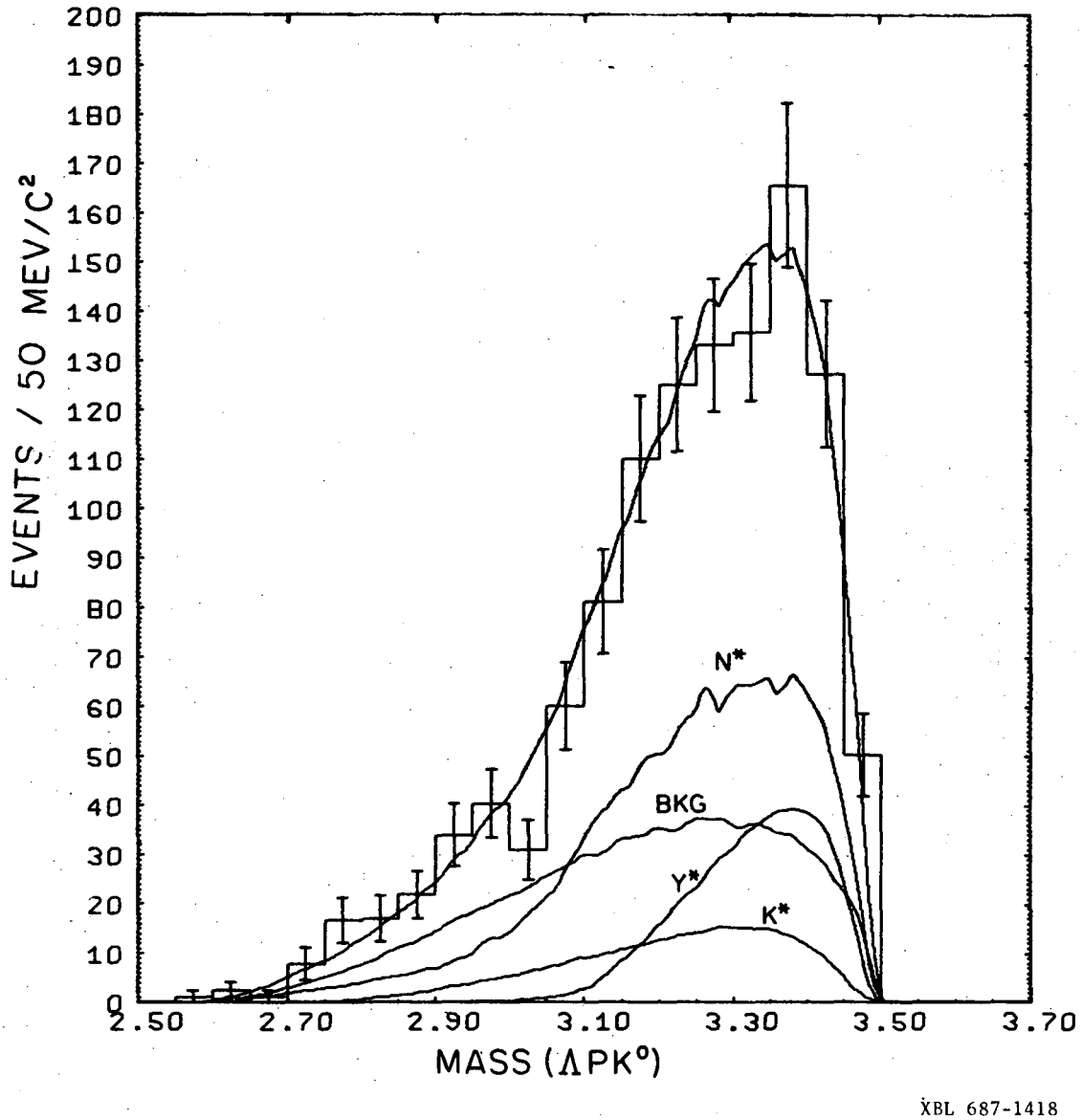


Fig. 31. Effective mass distribution of $\Lambda pK^{o}$ for examples of the reaction $pp \rightarrow \Lambda pK^{o}\pi^{+}$ (1170 events). The curves are pion-exchange predictions and are described in the text.

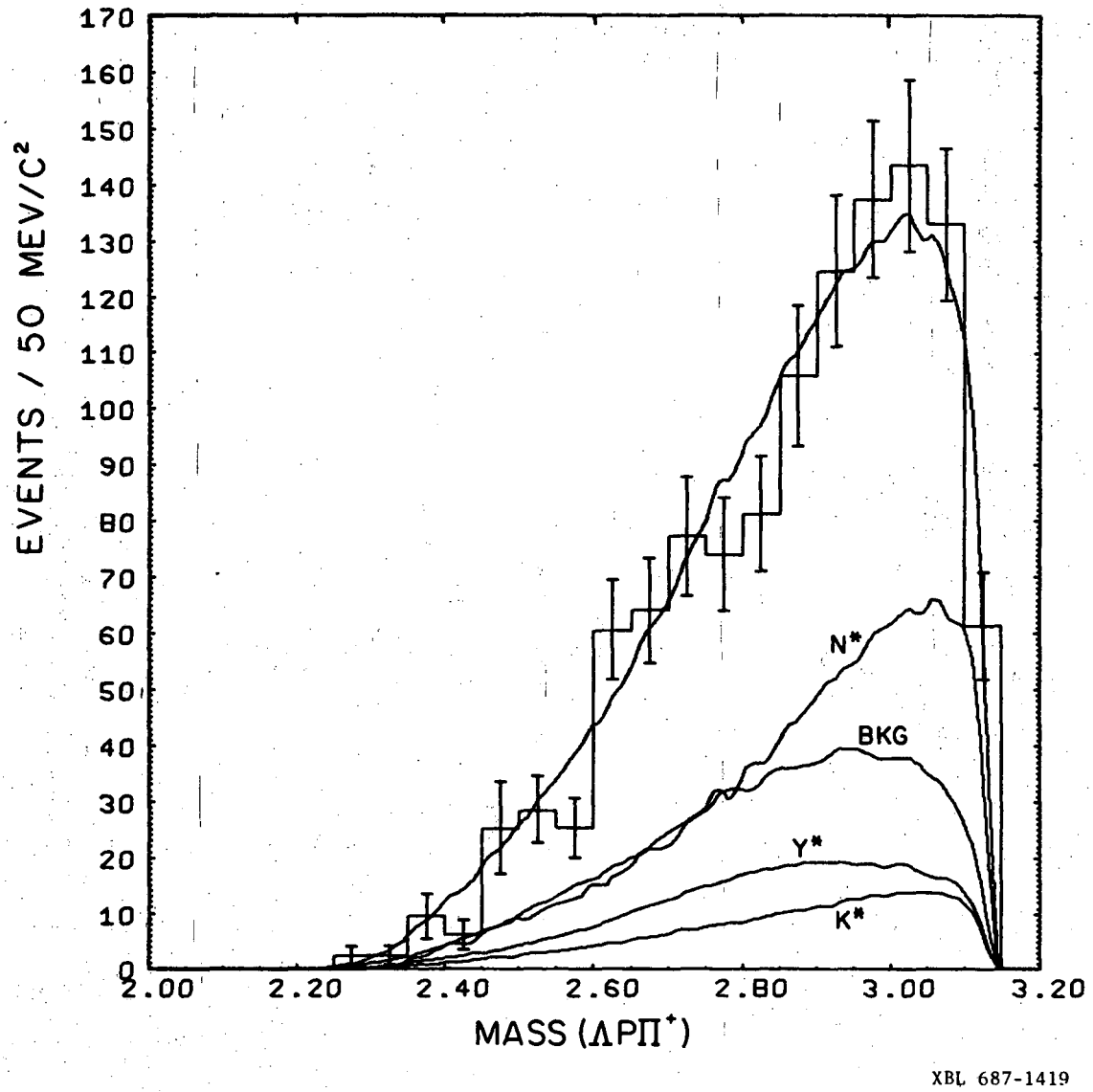


XBL 687-1419

Fig. 32. Effective mass distribution of $\Lambda p\pi^+$ for examples of the reaction $pp \rightarrow \Lambda pK^0\pi^+$ (1170 events). The curves are pion-exchange predictions and are described in the text.

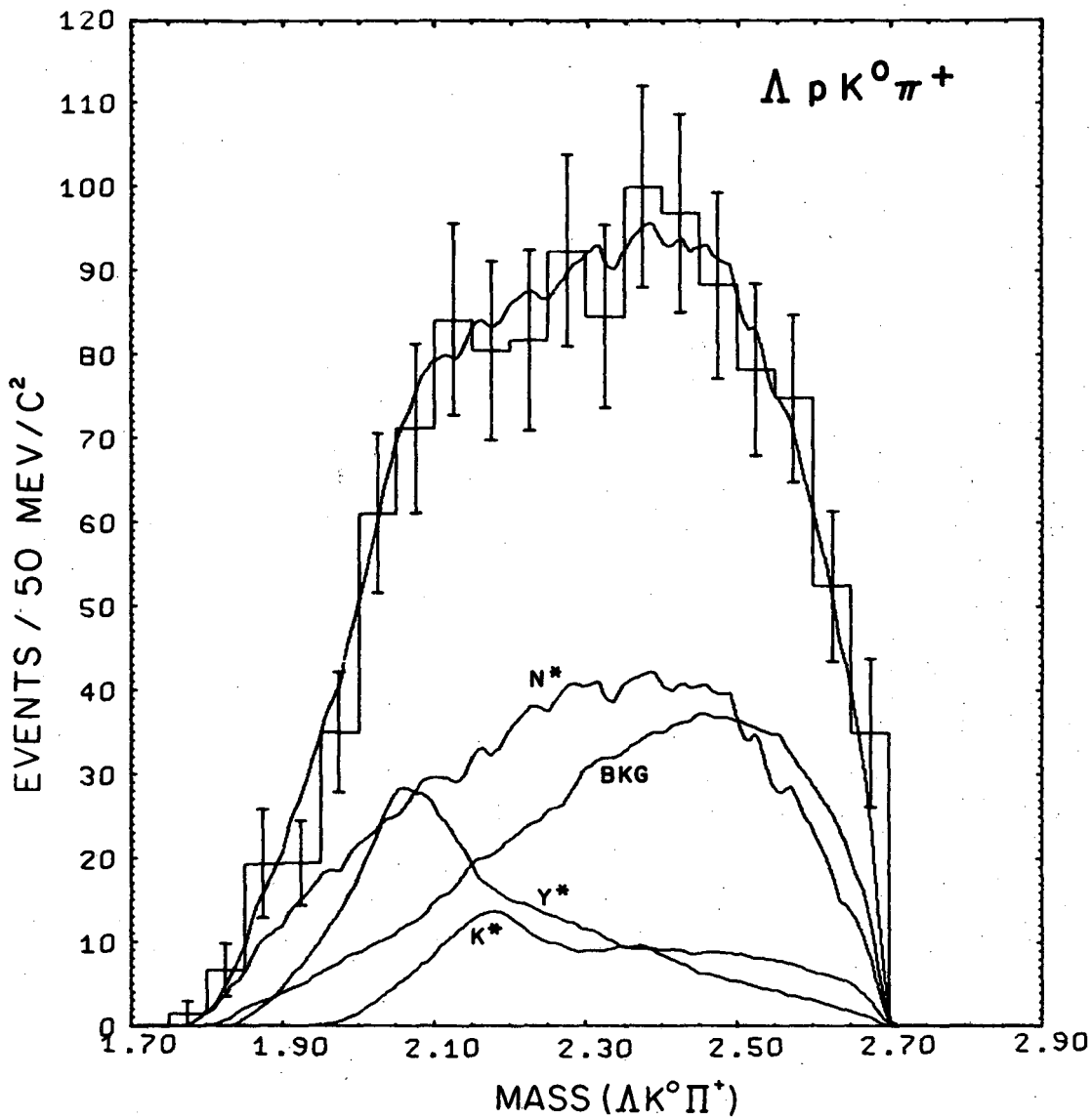


XBL 687-1420

Fig. 33. Effective mass distribution of $\Lambda K^{o}\pi^{+}$ for examples of the reaction $pp \rightarrow \Lambda p K^{o}\pi^{+}$ (1170 events). The curves are pion-exchange predictions and are described in the text.

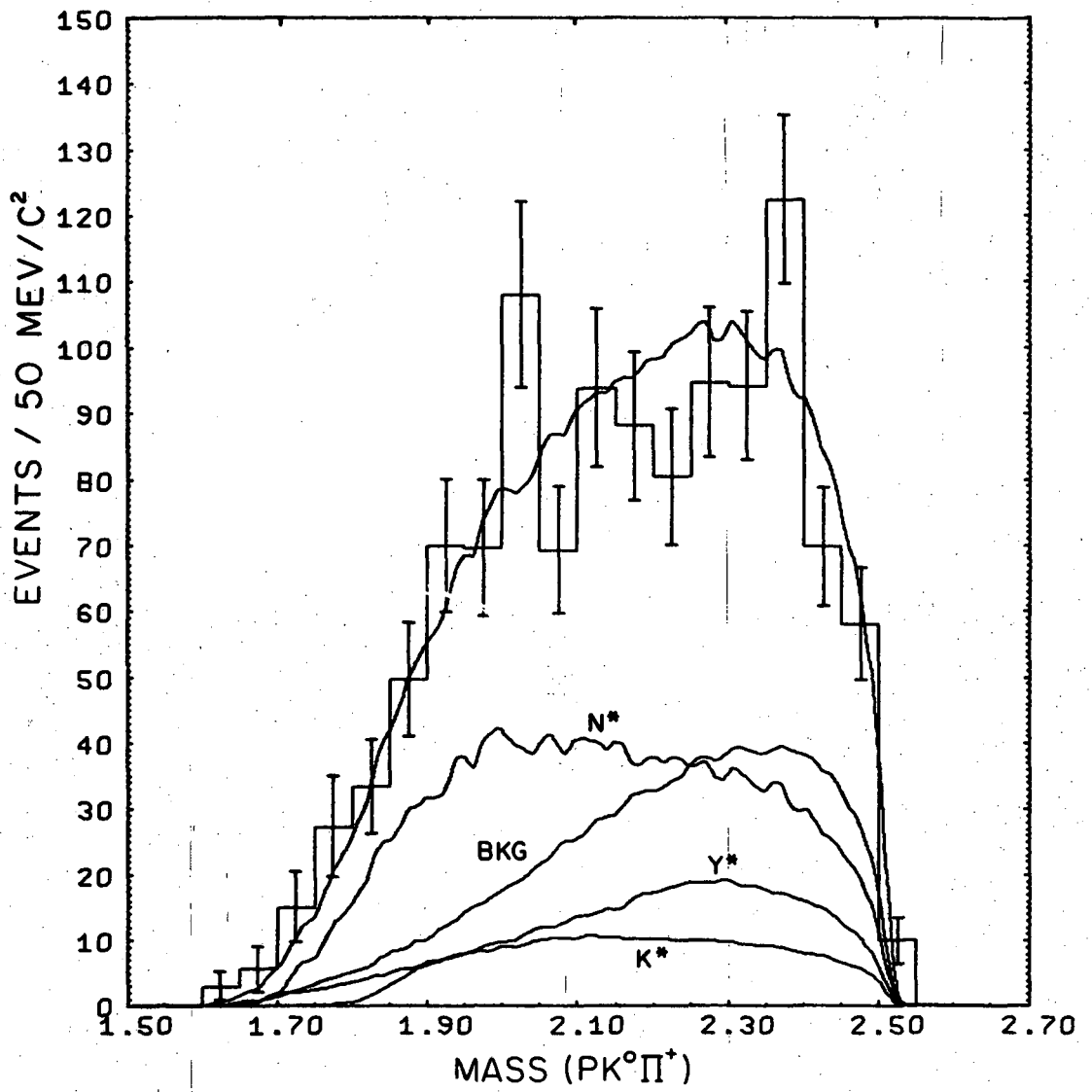


XBL 687-1421

Fig. 34. Effective mass distribution of $pK^{o}\pi^{+}$ for examples of the reaction $pp \rightarrow \Lambda pK^{o}\pi^{+}$ (1170 events). The curves are pion-exchange predictions and are described in the text.

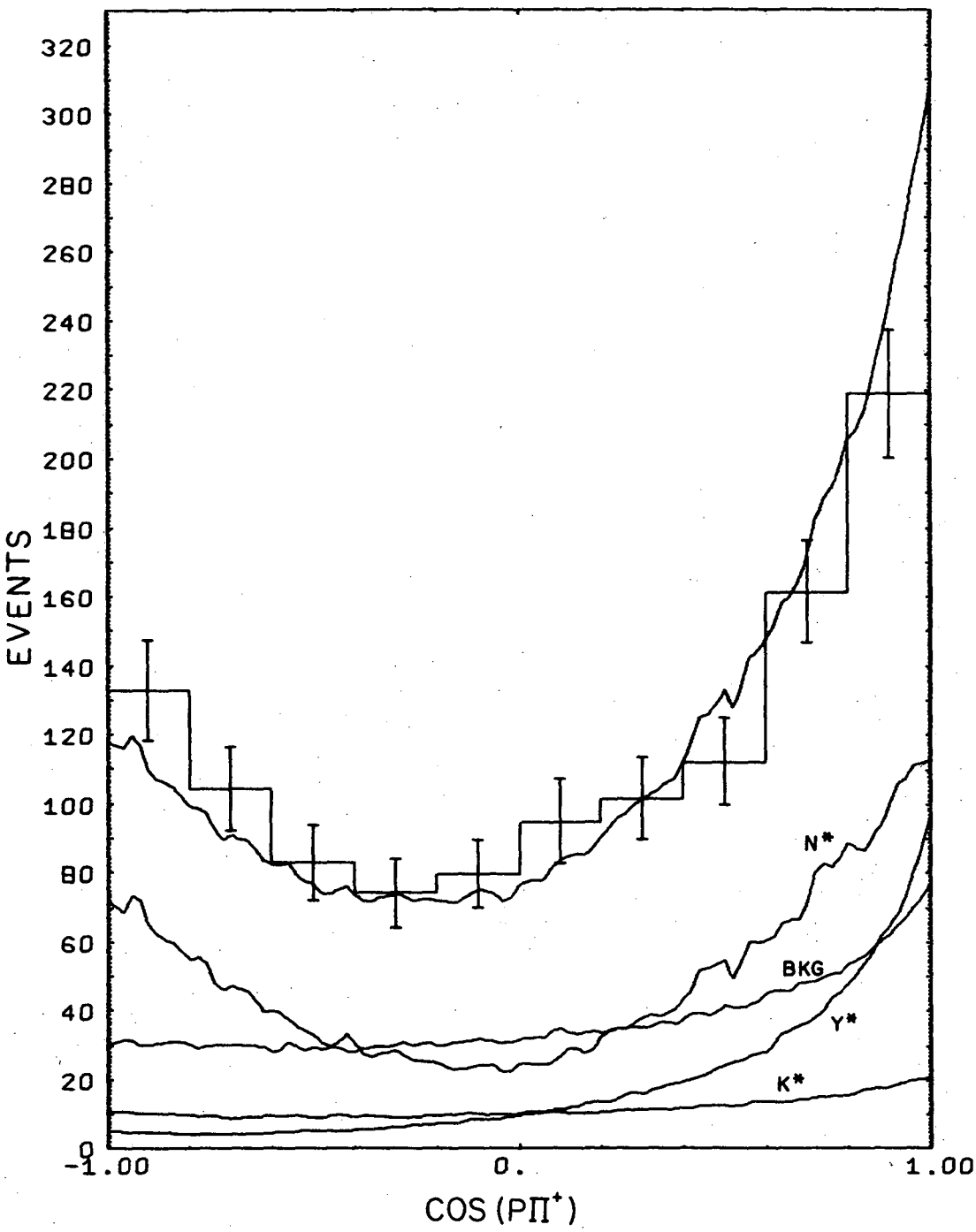


XBL 684-542

Fig. 35. Decay angular distribution of the $p\pi^+$ system for examples of the reaction $pp \rightarrow \Lambda pK^0\pi^+$ (1170 events). The angle is between the p and momentum transfer direction in the $p\pi^+$ rest system. The curves are pion-exchange predictions and are described in the text.

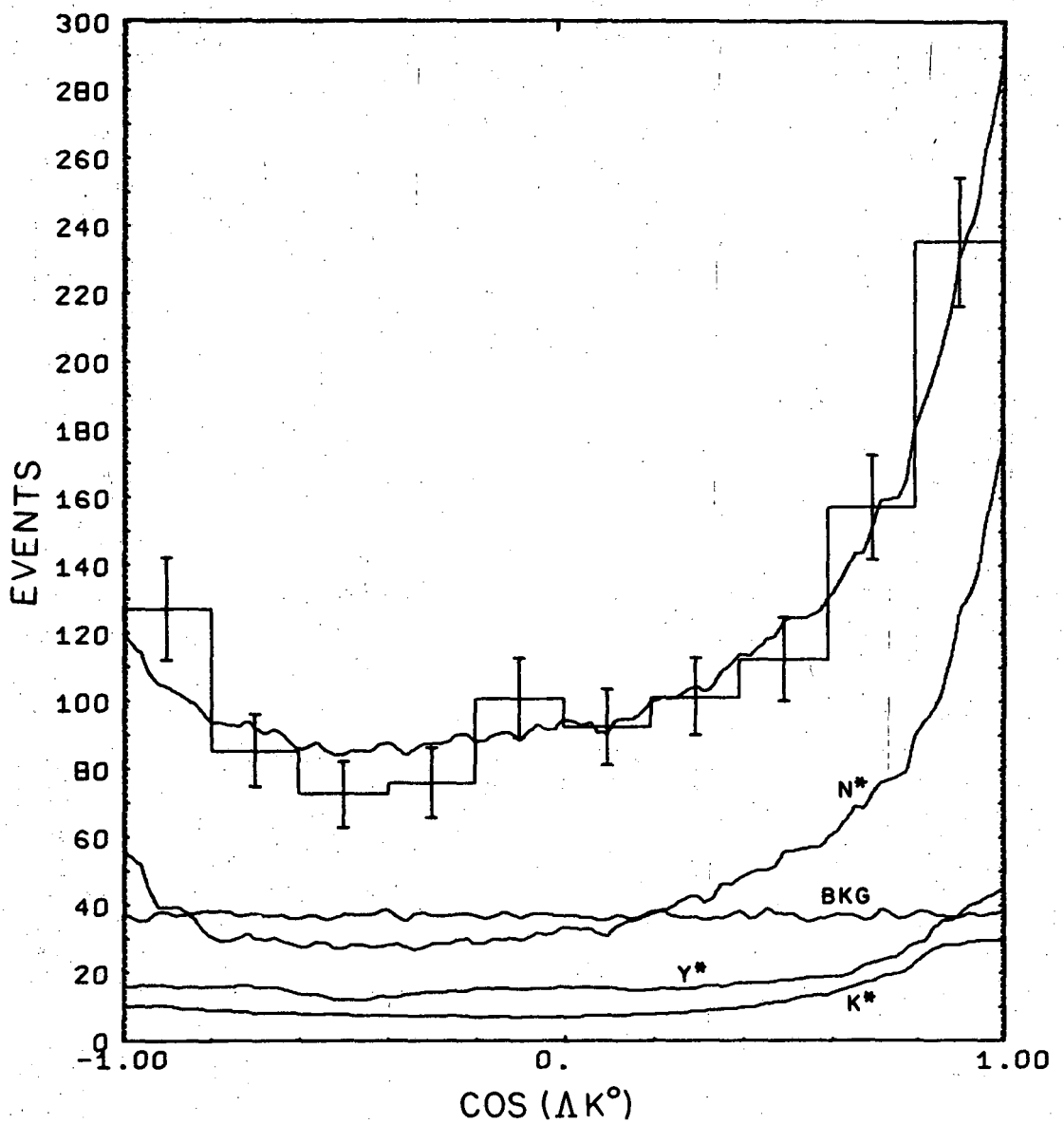


XBL 684-543

Fig. 36. Decay angular distribution of the $\Lambda K^{o}$ system for examples of $pp \rightarrow \Lambda p K^{o} \pi^{+}$ (1170 events). The angle is between the $\Lambda$ and momentum transfer direction in the $p\pi^{+}$ rest system. The curves are pion-exchange predictions and are described in the text.

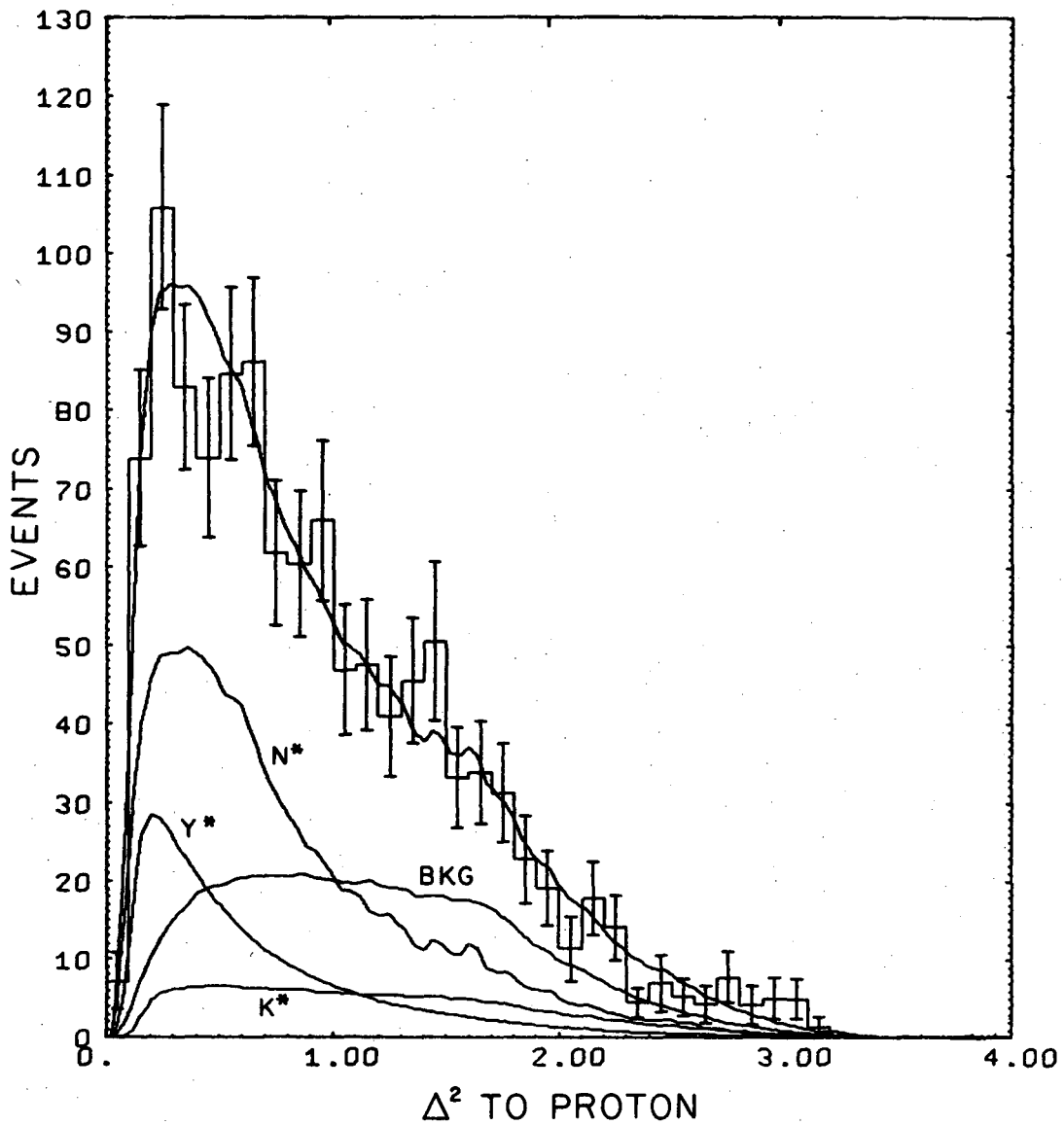


Fig. 37. Distribution of four-momentum transfer to the proton for examples of the reaction $pp \rightarrow \Lambda p K^{o} \pi^{+}$ (1170 events). The curves are pion-exchange predictions and are described in the text.

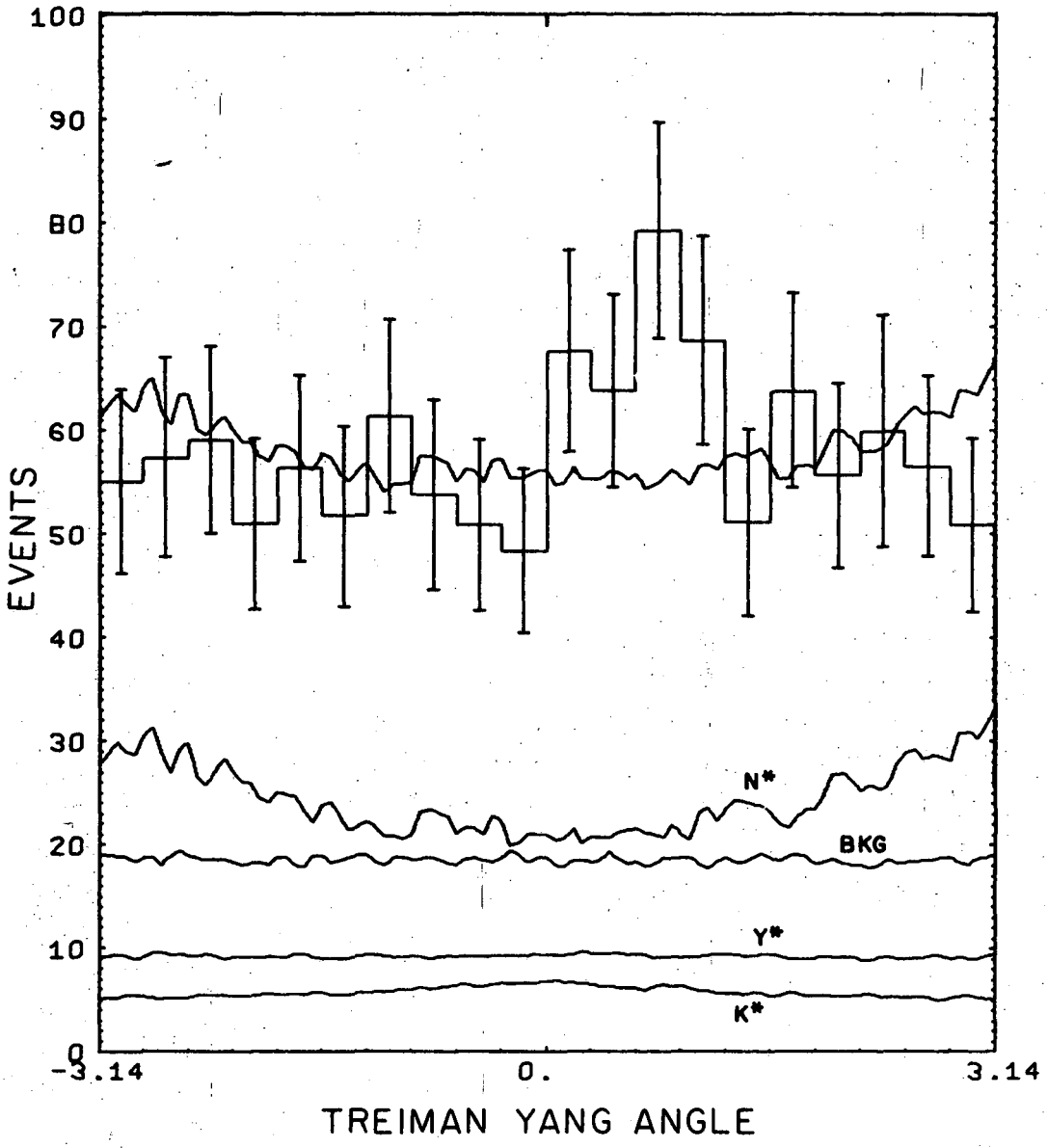


Fig. 38. Distribution of the Treiman-Yang angle for examples of the reaction $pp \rightarrow \Lambda pK^{o}\pi^{+}$ (1170 events). The curves are pion-exchange predictions and are described in the text.

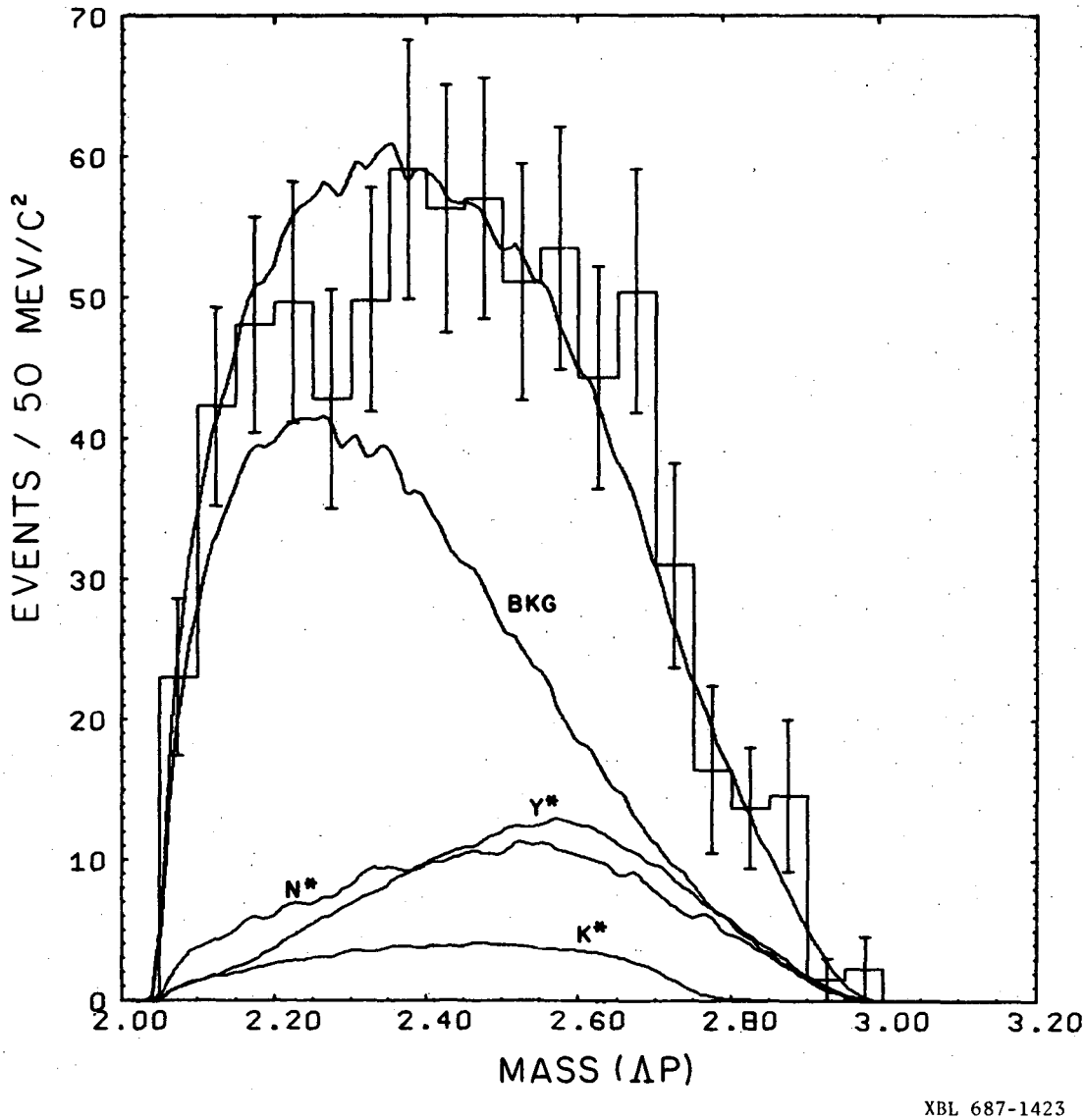


Fig. 39. Effective mass distribution of Λp for examples of the reaction $pp \rightarrow \Lambda p K^{+} \pi^{o}$ (708 events). The curves are pion-exchange predictions and are described in the text.

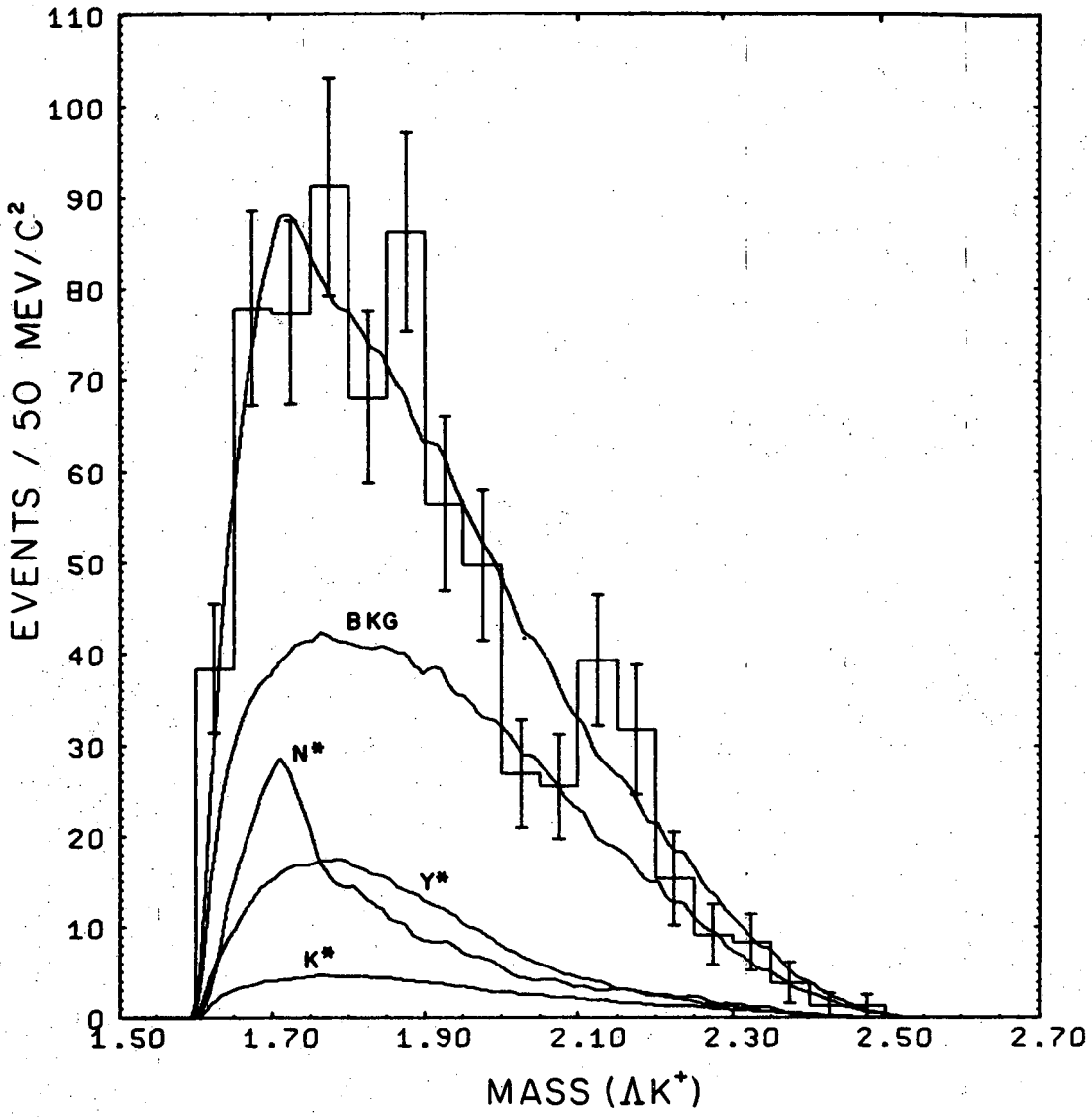


XBL 687-1424

Fig. 40. Effective mass distribution of $\Lambda K^+$ for examples of the reaction $pp \rightarrow \Lambda p K^+ \pi^o$ (708 events). The curves are pion-exchange predictions and are described in the text.

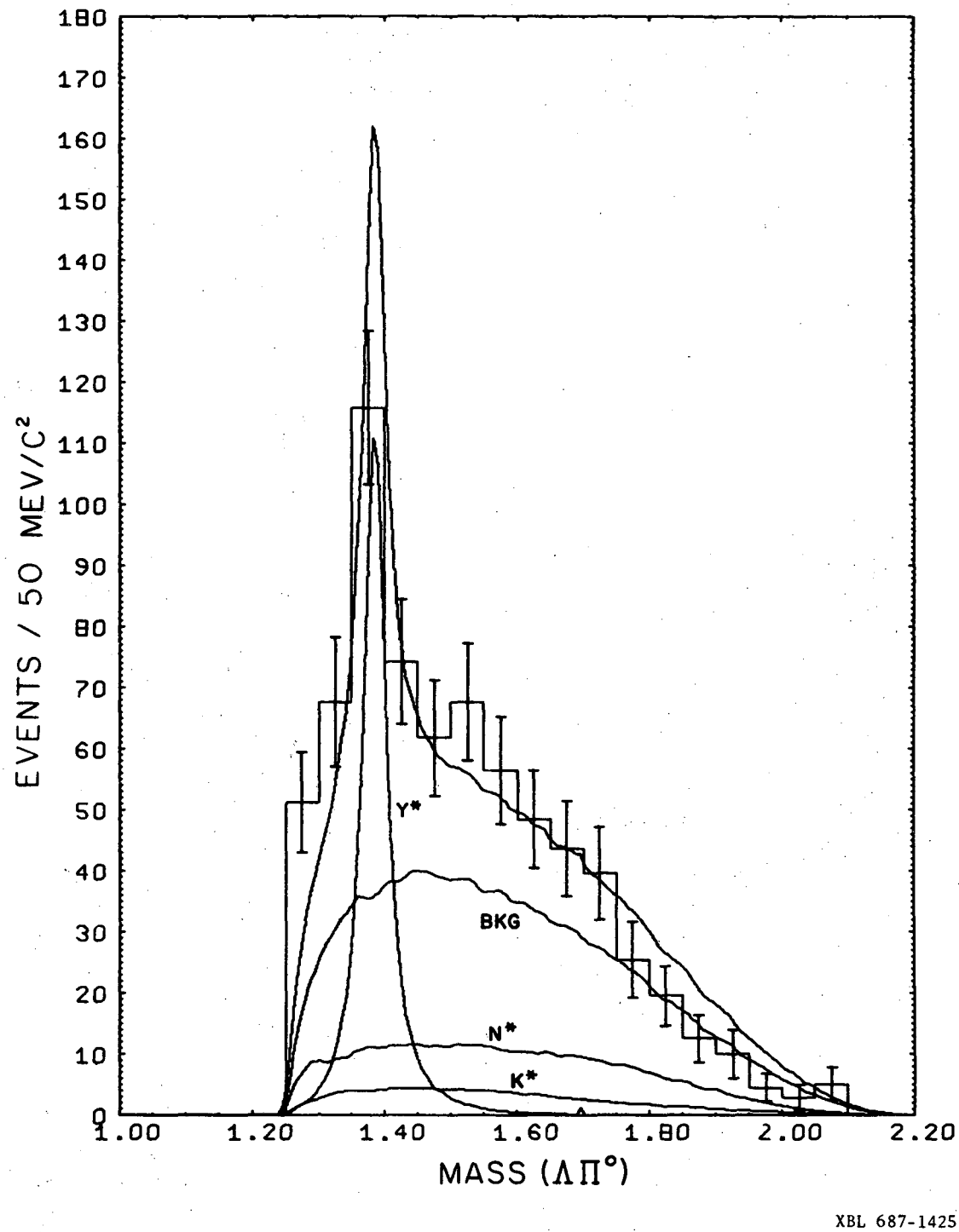


XBL 687-1425

Fig. 41. Effective mass distribution of $\Lambda\pi^{o}$ for examples of the reaction $pp \rightarrow \Lambda pK^{+}\pi^{o}$ (708 events). The curves are pion-exchange predictions and are described in the text.

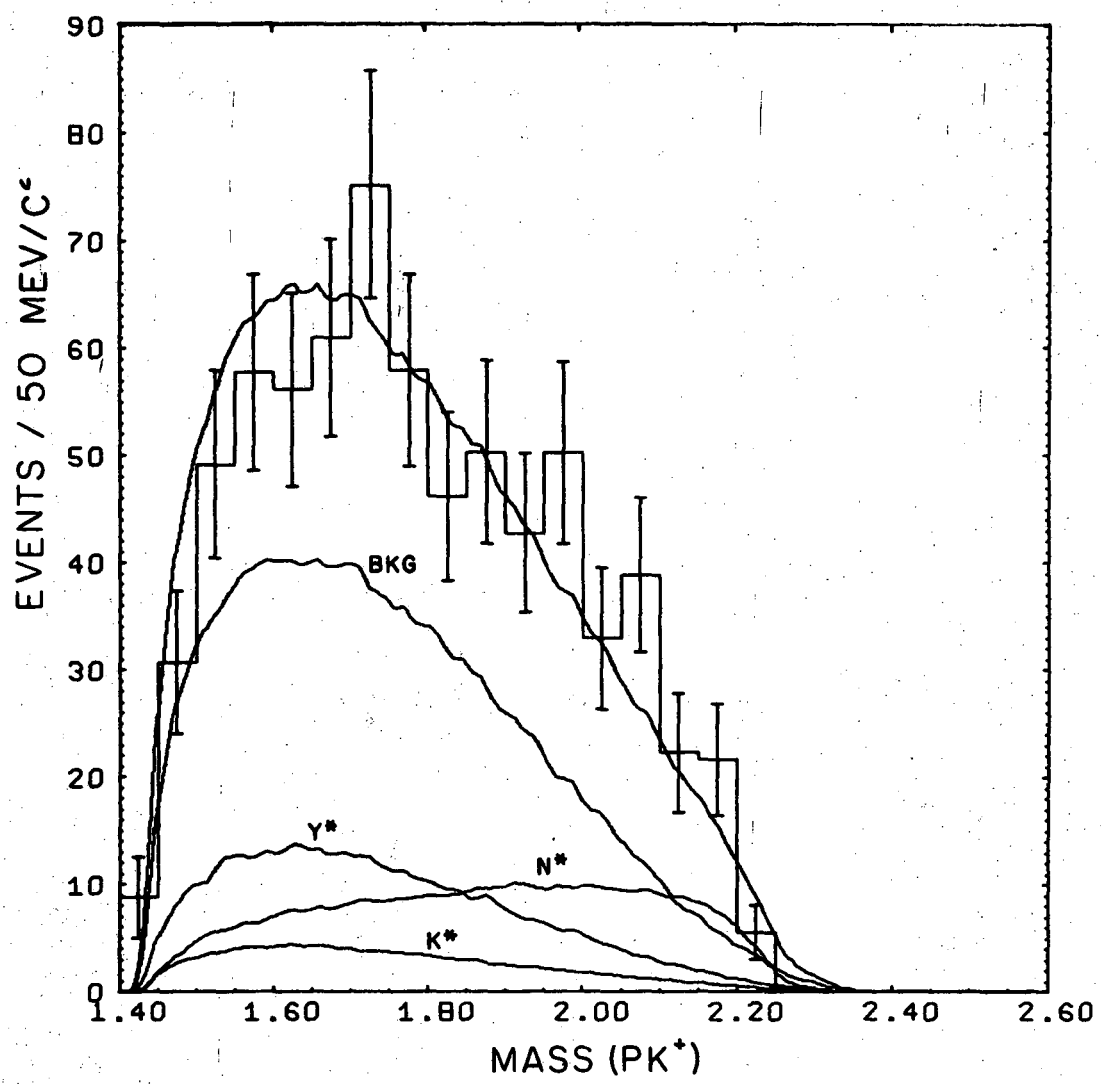


XBL 687-1449

Fig. 42. Effective mass distribution of $pK^+$ for examples of the reaction $pp \rightarrow \Lambda pK^+\pi^o$ (708 events). The curves are pion-exchange predictions and are described in the text.

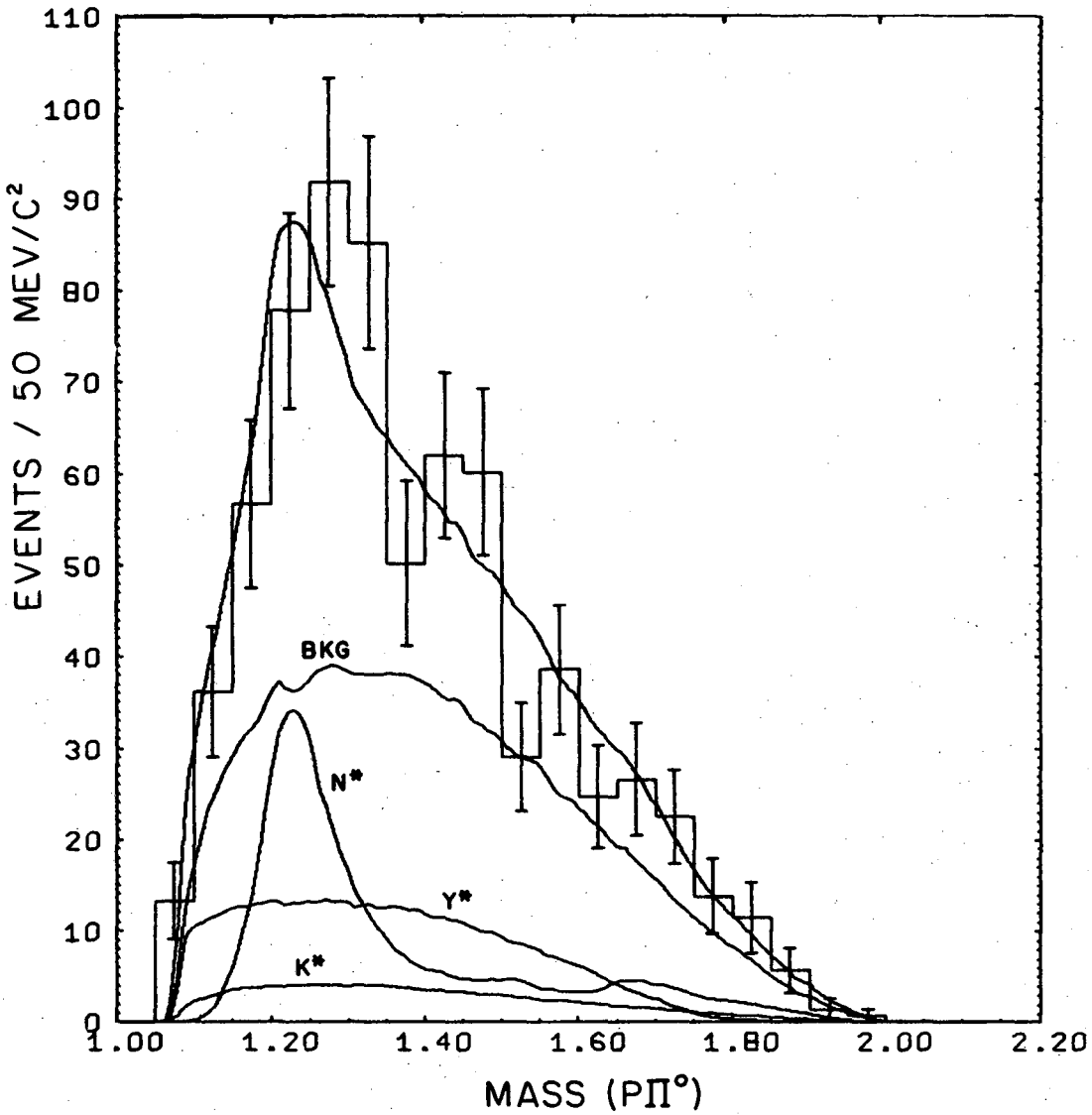


XBL 687-1426

Fig. 43. Effective mass distribution of $p\pi^0$ for examples of the reaction $pp \rightarrow \Lambda pK^+\pi^0$ (708 events). The curves are pion-exchange predictions and are described in the text.

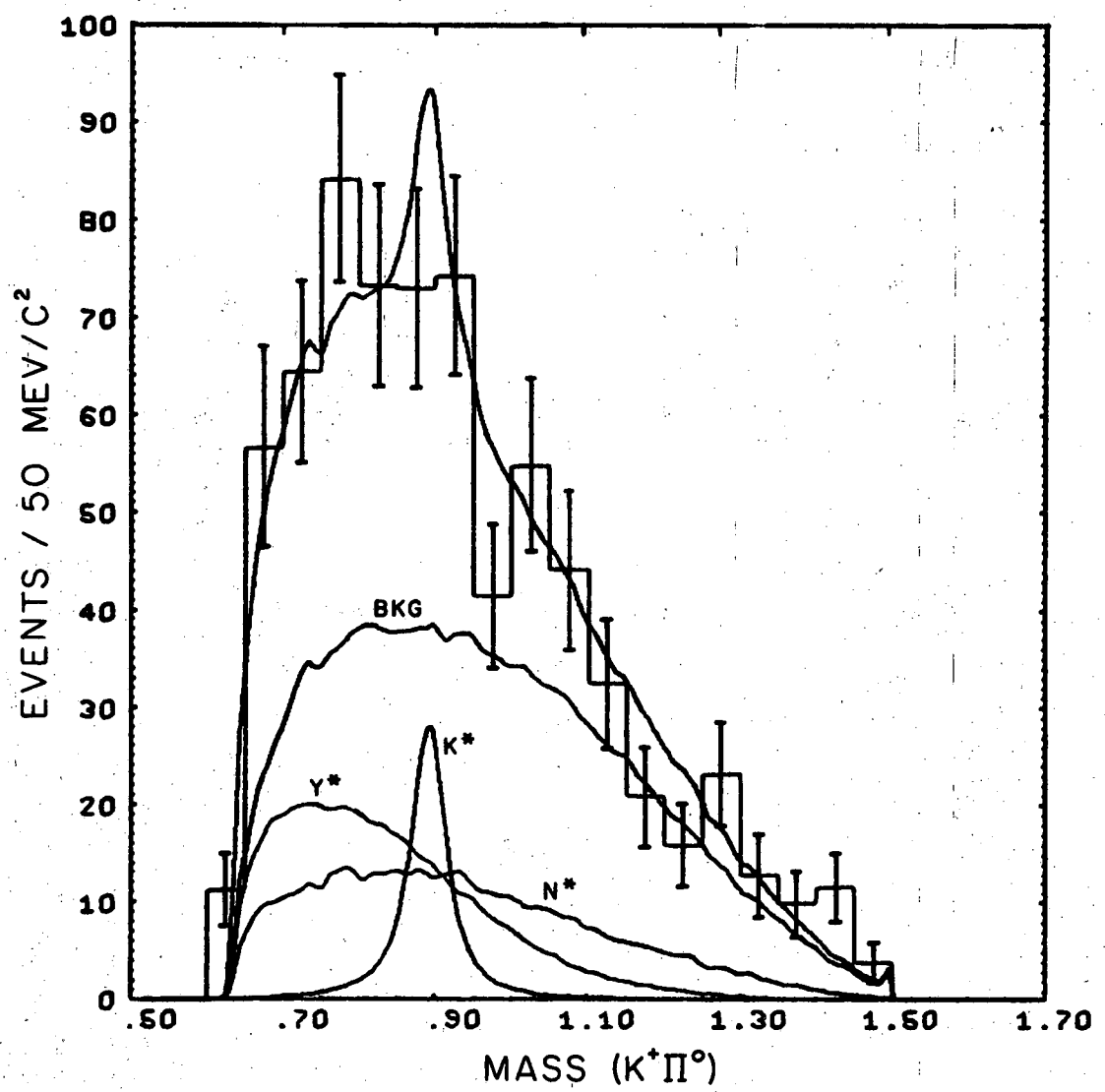


Fig. 44. Effective mass distribution of $K^+\pi^o$ for examples of the reaction $pp \rightarrow \Lambda pK^+\pi^o$ (708 events). The curves are pion-exchange predictions and are described in the text.

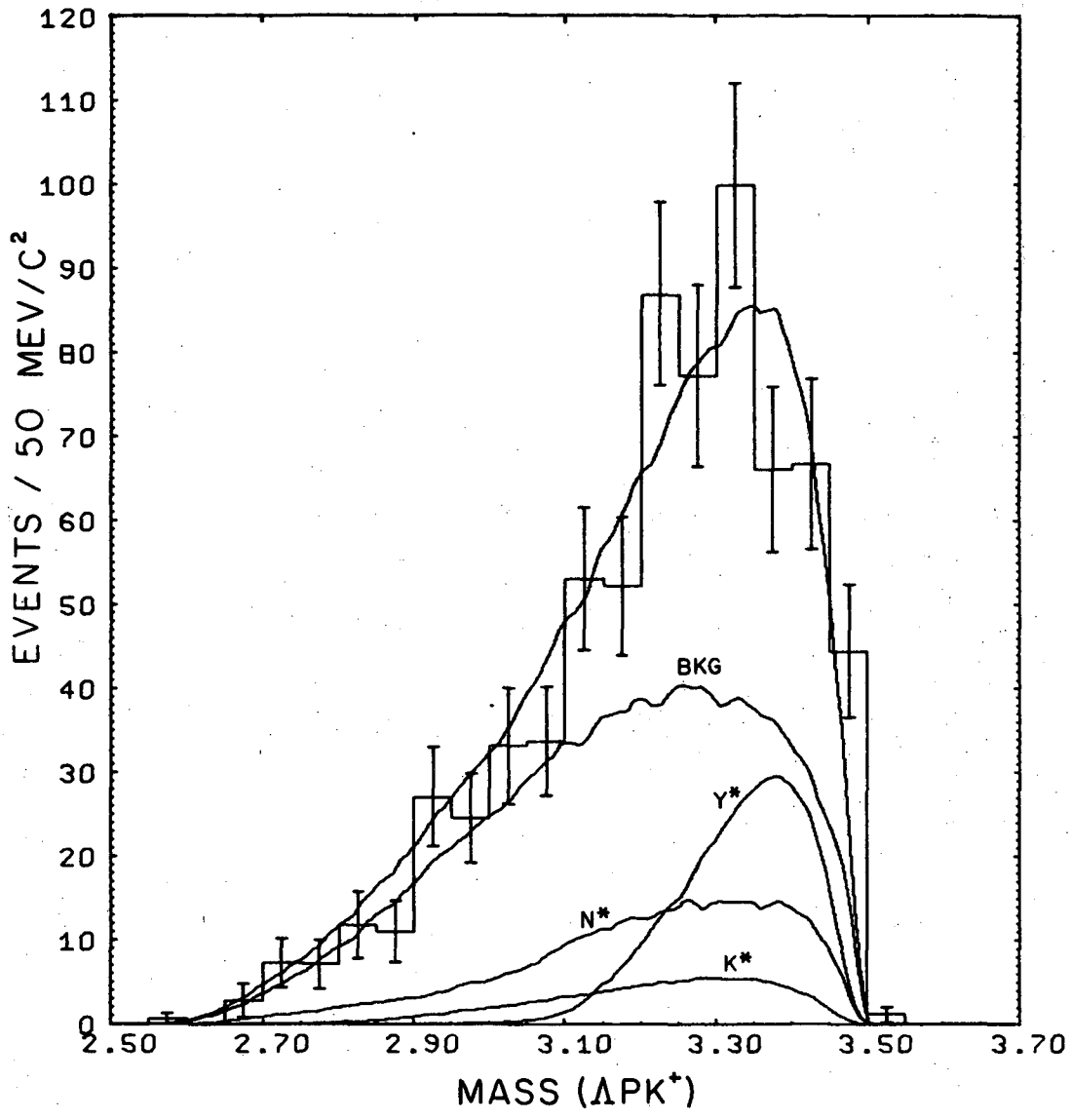


XBL 687-1428

Fig. 45. Effective mass distribution of $\Lambda pK^+$ for examples of the reaction $pp \rightarrow \Lambda pK^+\pi^o$ (708 events). The curves are pion-exchange predictions and are described in the text.

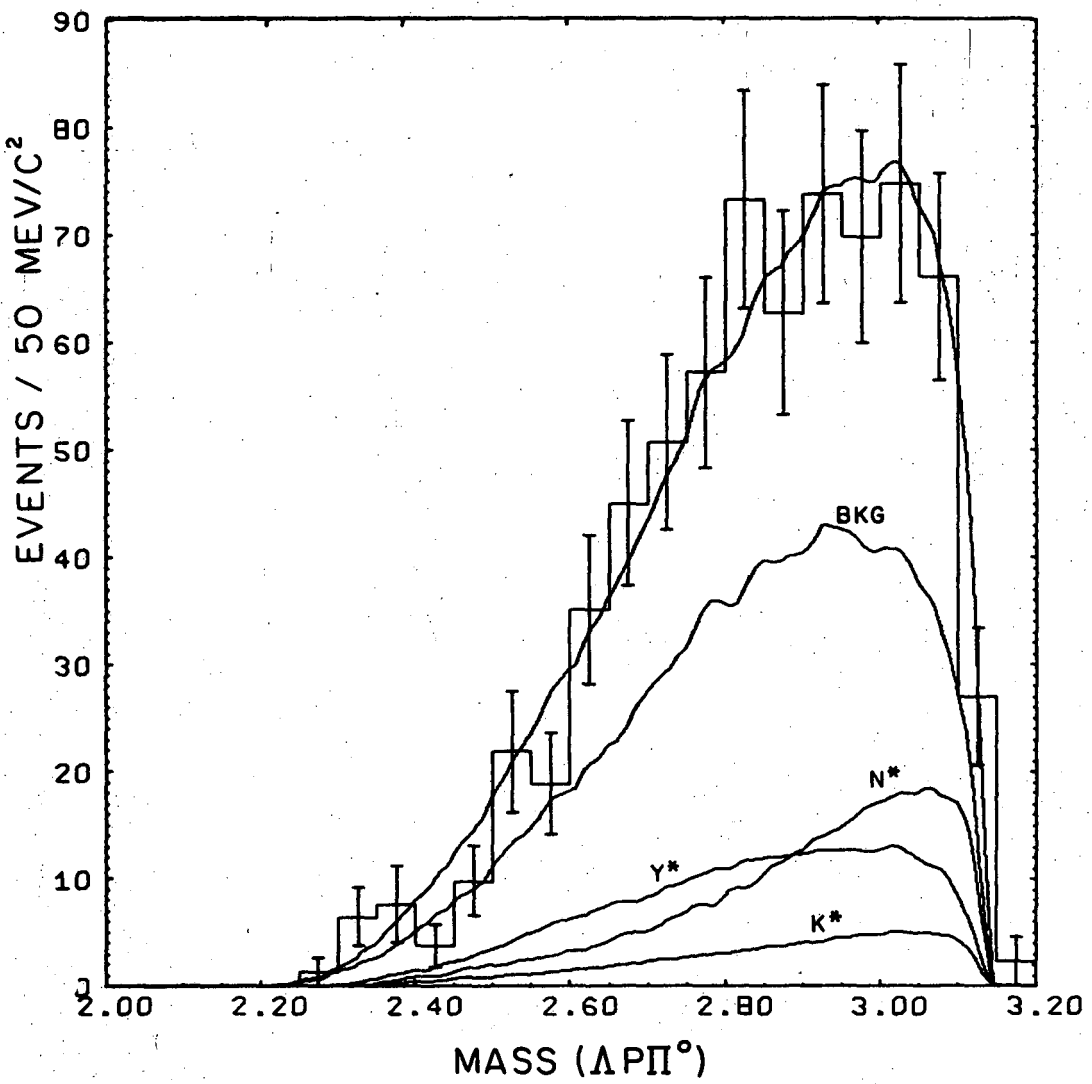


Fig. 46. Effective mass distribution of $\Lambda p\pi^0$ for examples of the reaction $pp \rightarrow \Lambda pK^+\pi^0$ (708 events). The curves are pion-exchange predictions and are described in the text.

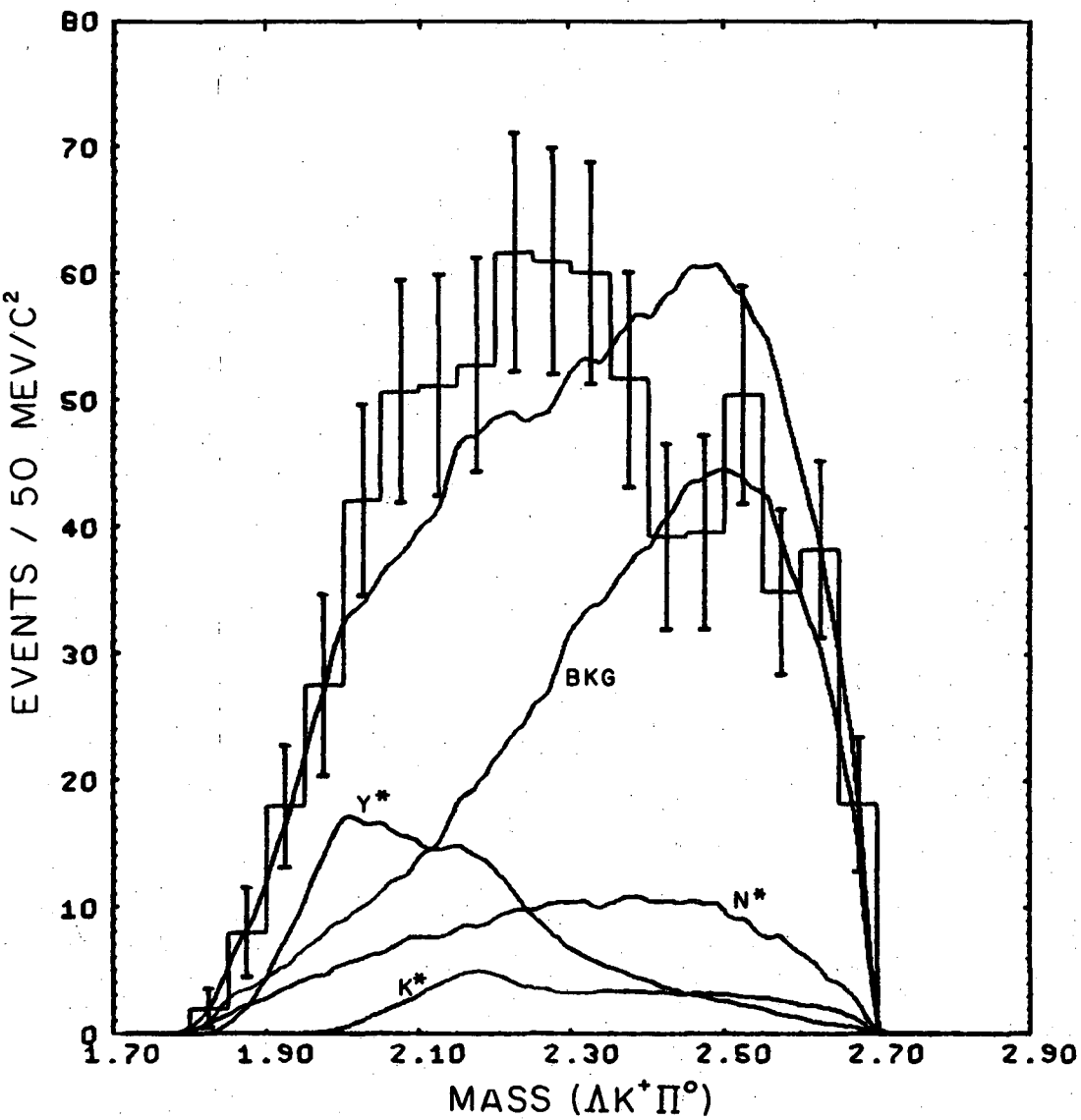


Fig. 47. Effective mass distribution of $\Lambda K^+\pi^o$ for examples of the reaction $pp \rightarrow \Lambda pK^+\pi^o$ (708 events). The curves are pion-exchange predictions and are described in the text.

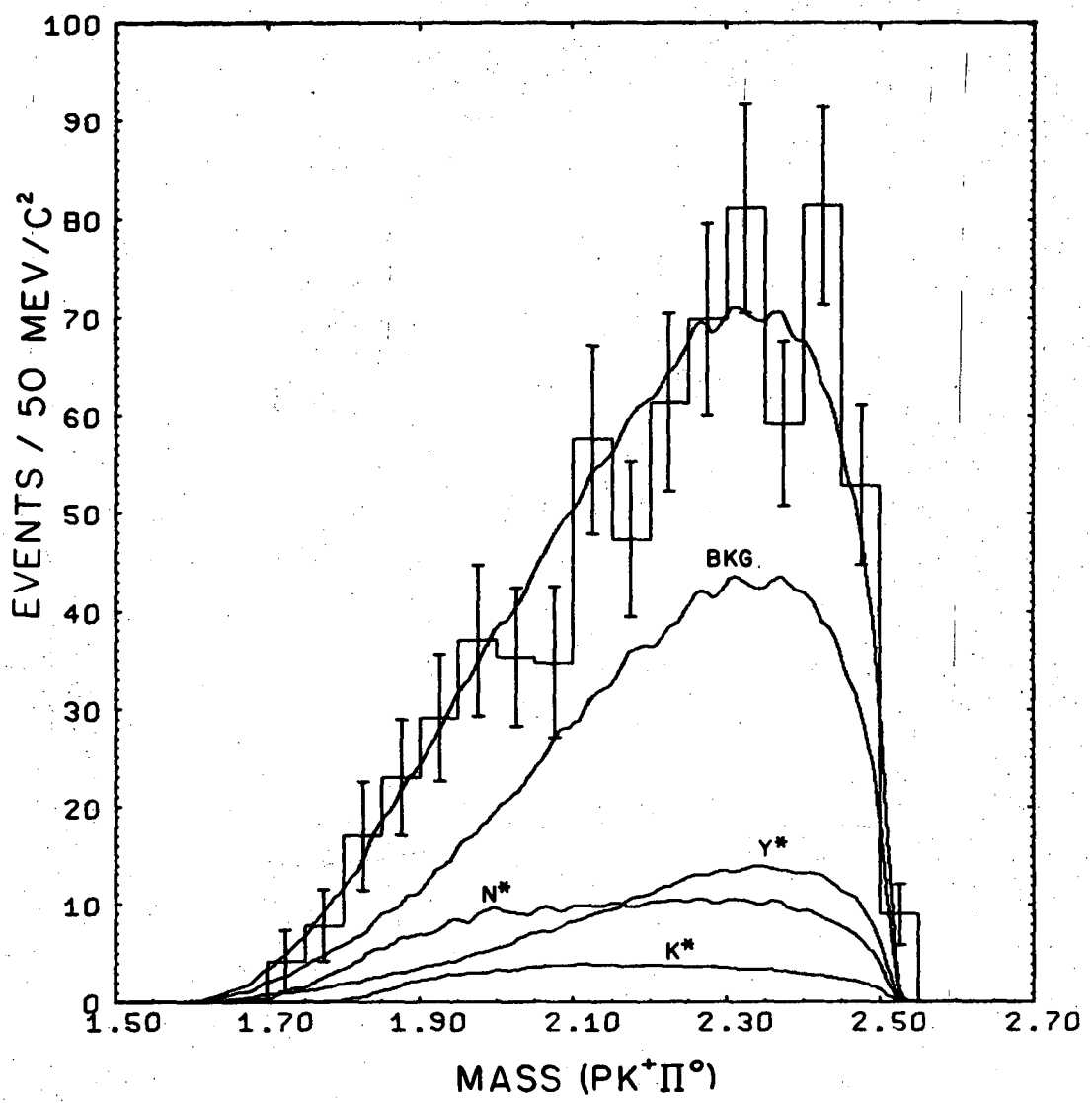


XBL 687-1431

Fig. 48. Effective mass distribution of $pK^+\pi^o$ for examples of the reaction $pp \rightarrow \Lambda pK^+\pi^o$ (708 events). The curves are pion-exchange predictions and are described in the text.

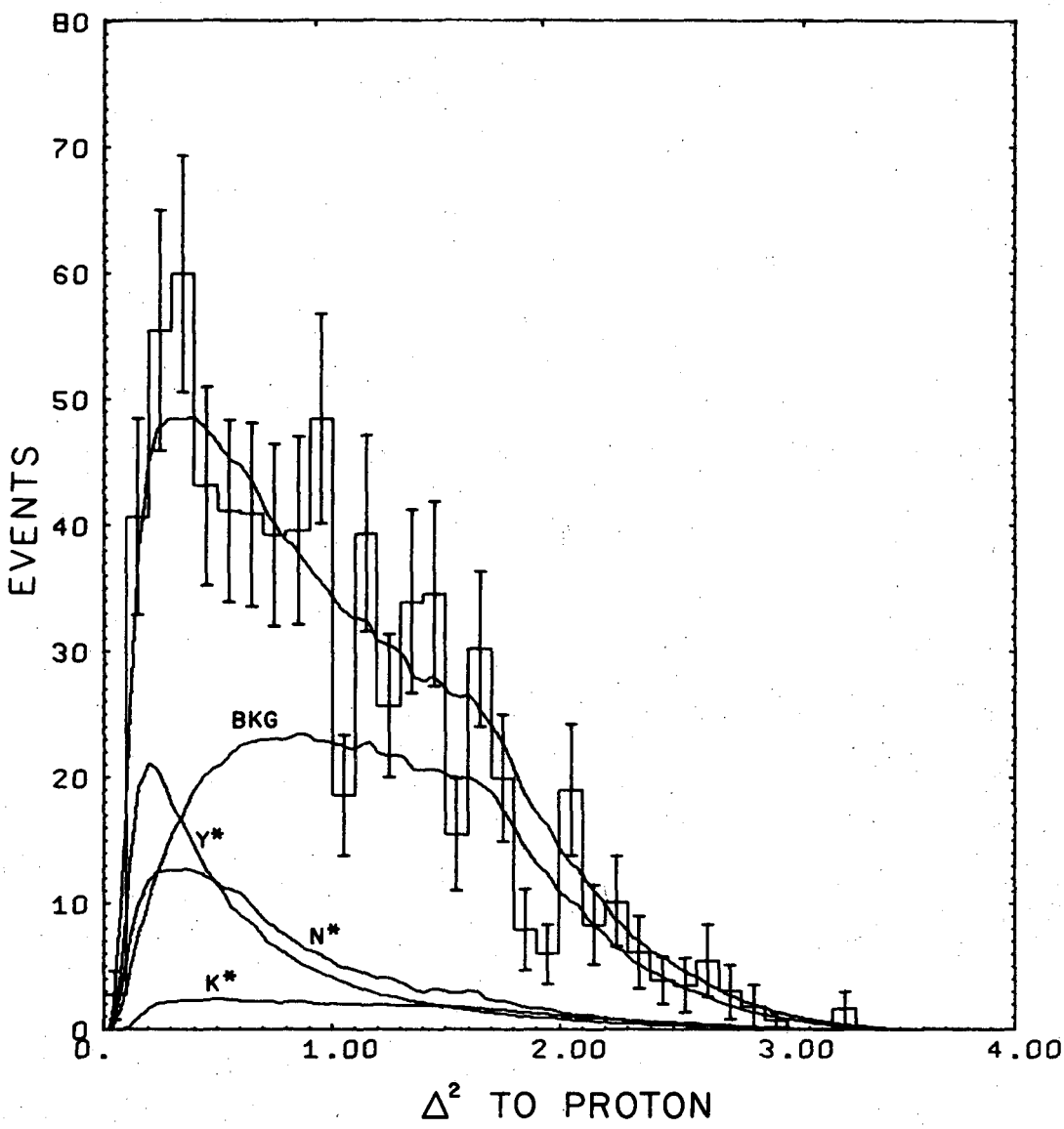


Fig. 49. Distribution of four-momentum transfer to the proton for examples of the reaction $pp \rightarrow \Lambda pK^{+}\pi^{o}$ (708 events). The curves are pion-exchange predictions and are described in the text.

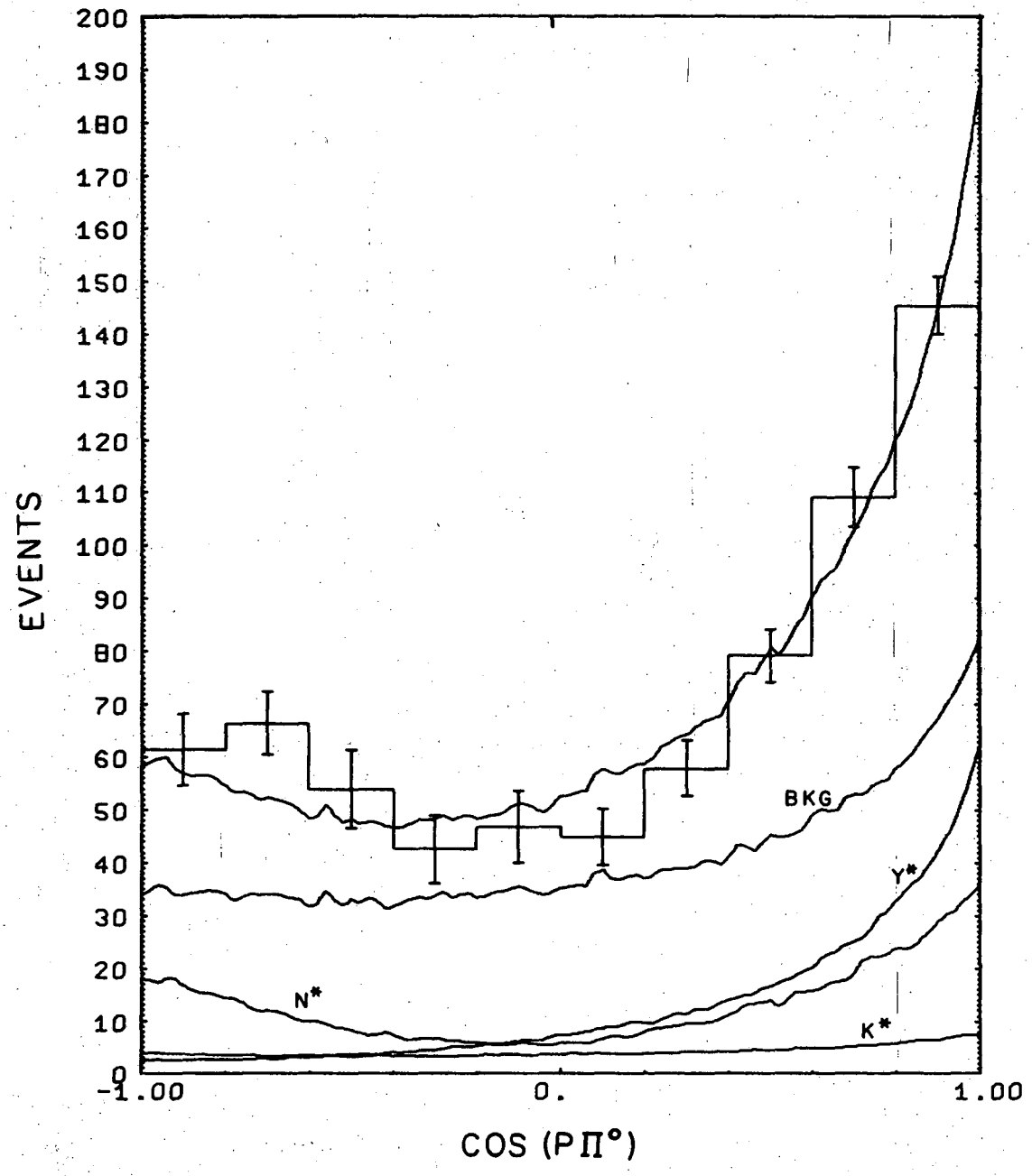


XBL 687-1434

Fig. 50. Decay angular distribution of the $p\pi^o$ system for examples of the reaction $pp \rightarrow \Lambda pK^+\pi^o$ (708 events). The angle is between the p and momentum transfer direction in the $p\pi^o$ rest system. The curves are pion-exchange predictions and are described in the text.

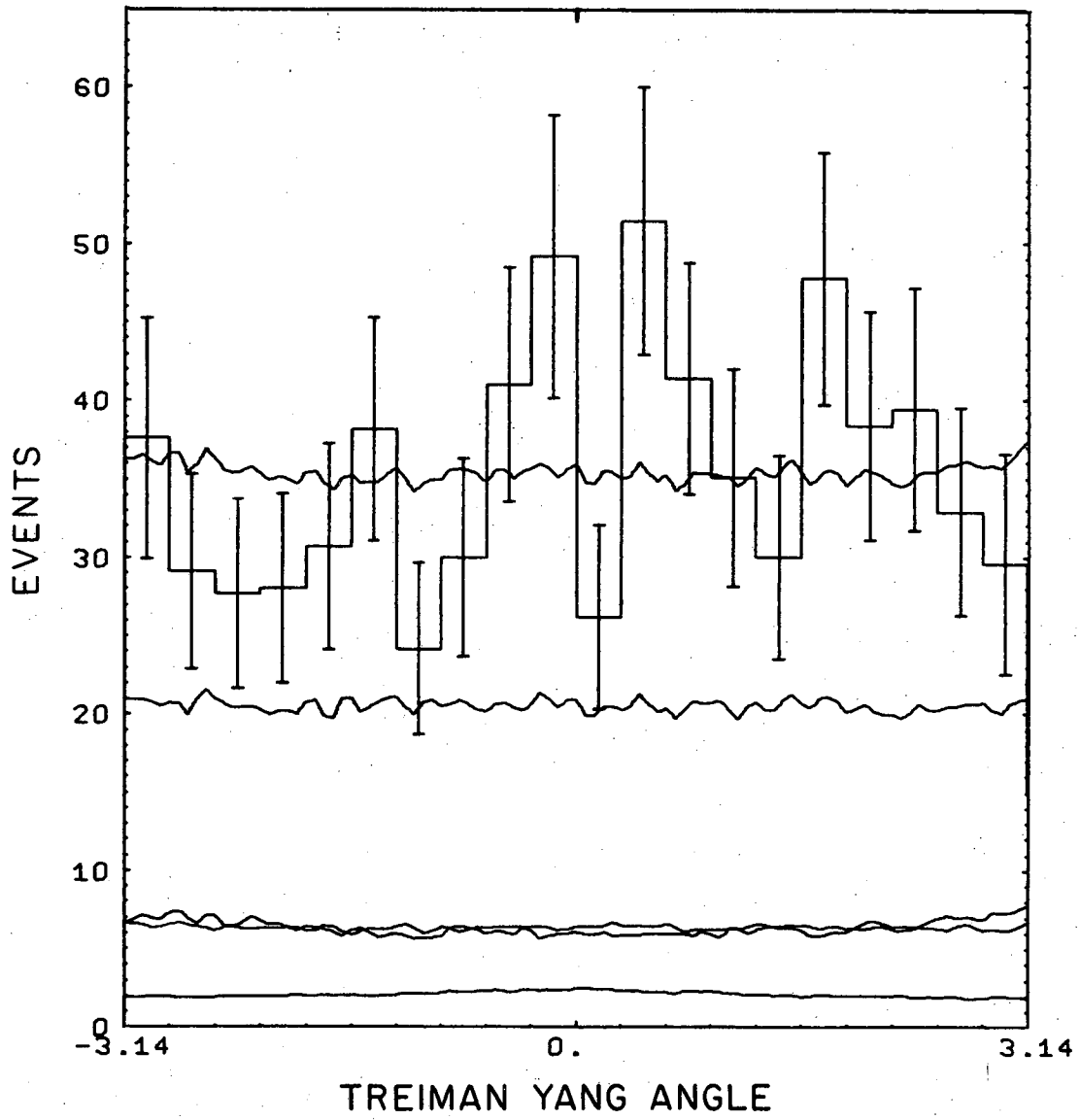


XBL 687-1433

Fig. 51. Distribution of the Treiman-Yang angle for examples of the reaction $pp \rightarrow \Lambda pK^{+}\pi^{o}$ (708 events). The curves are pion-exchange predictions and are described in the text.

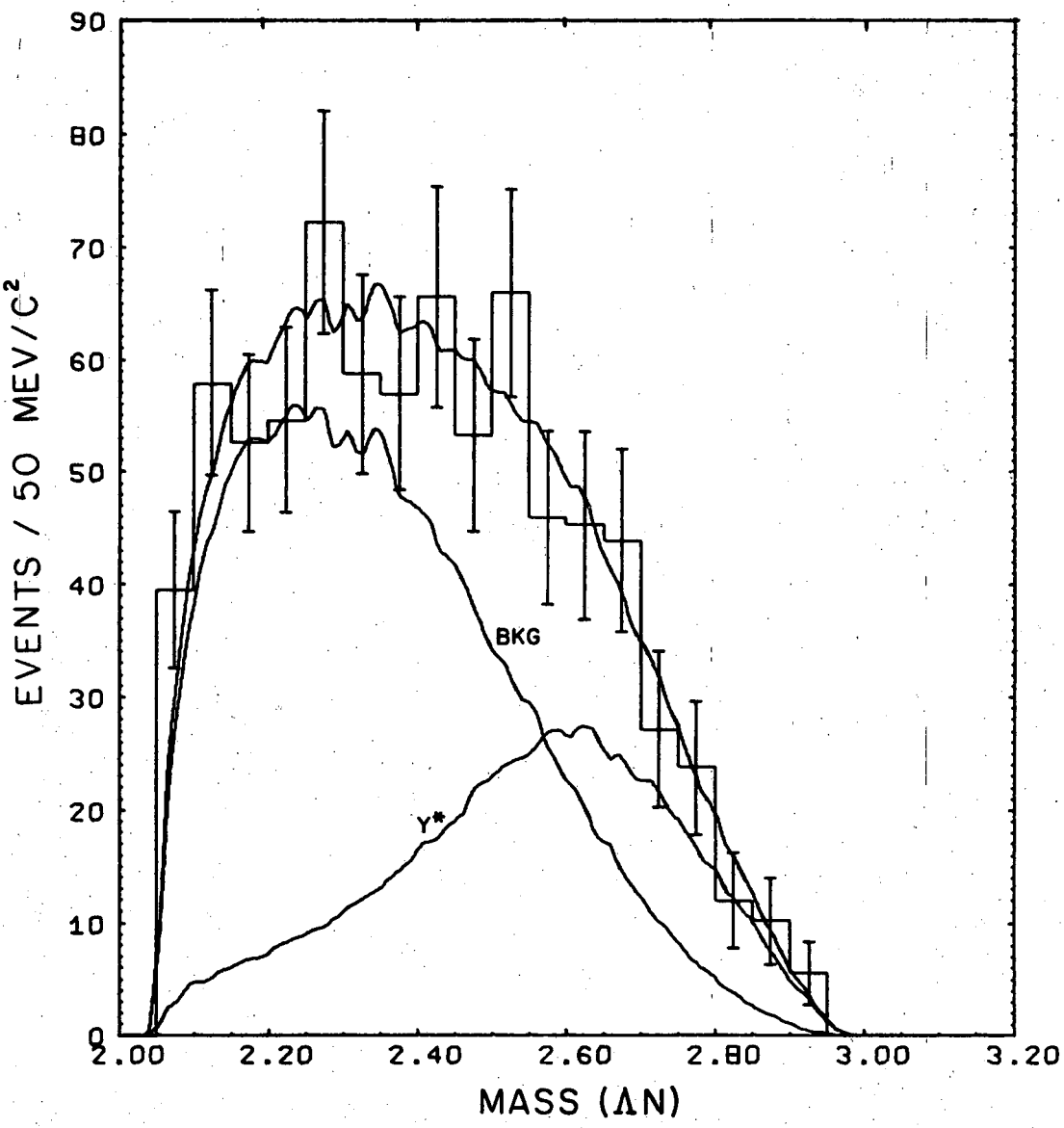


XBL 687-1435

Fig. 52. Effective mass distribution of Λn for examples of the reaction $pp \rightarrow \Lambda n K^+ \pi^+$ (791 events). The curves are pion-exchange predictions and are described in the text.

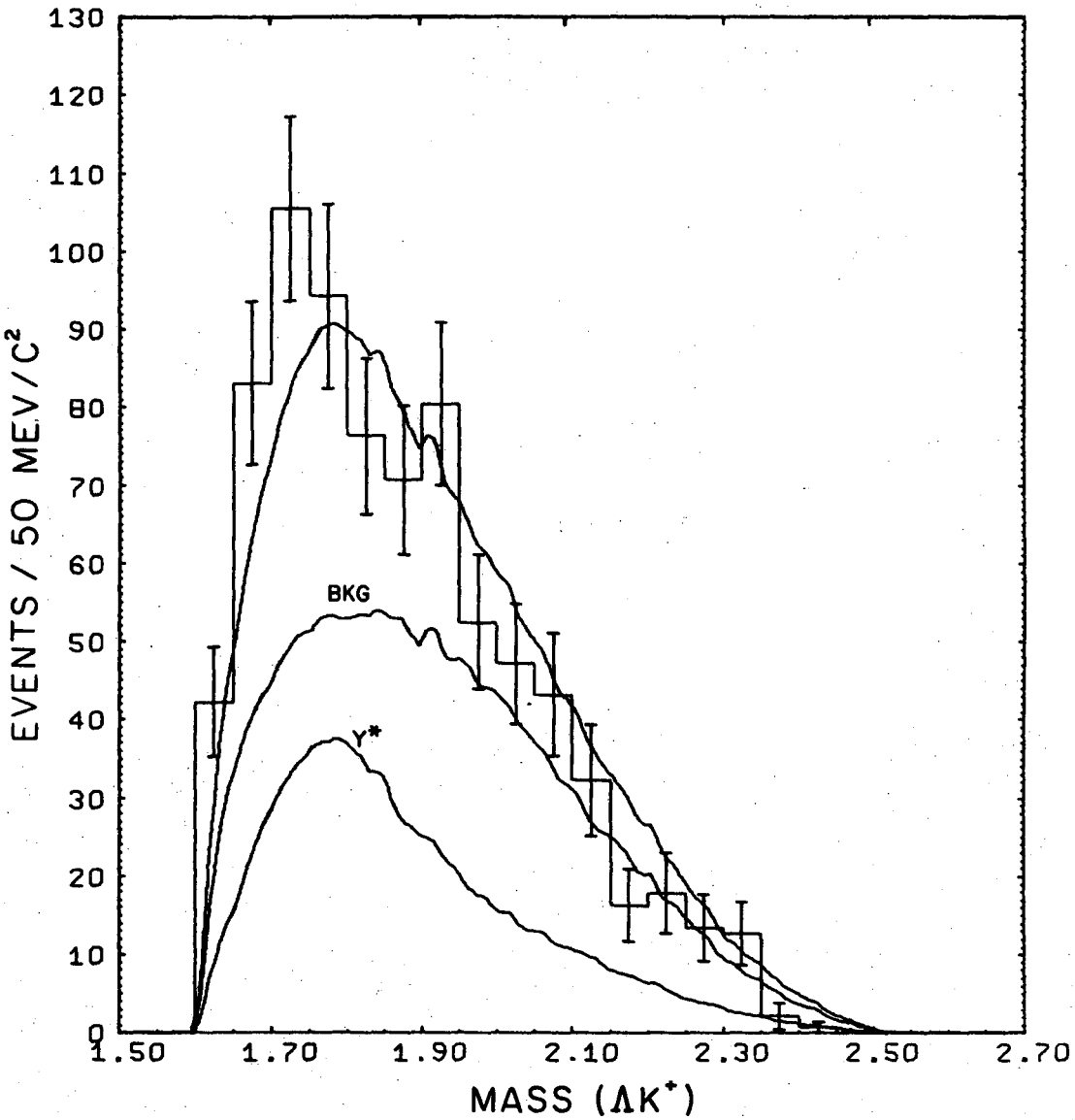


XBL 687-1436

Fig. 53. Effective mass distribution of $\Lambda K^+$ for examples of the reaction $pp \rightarrow \Lambda n K^+ \pi^+$ (791 events). The curves are pion-exchange predictions and are described in the text.

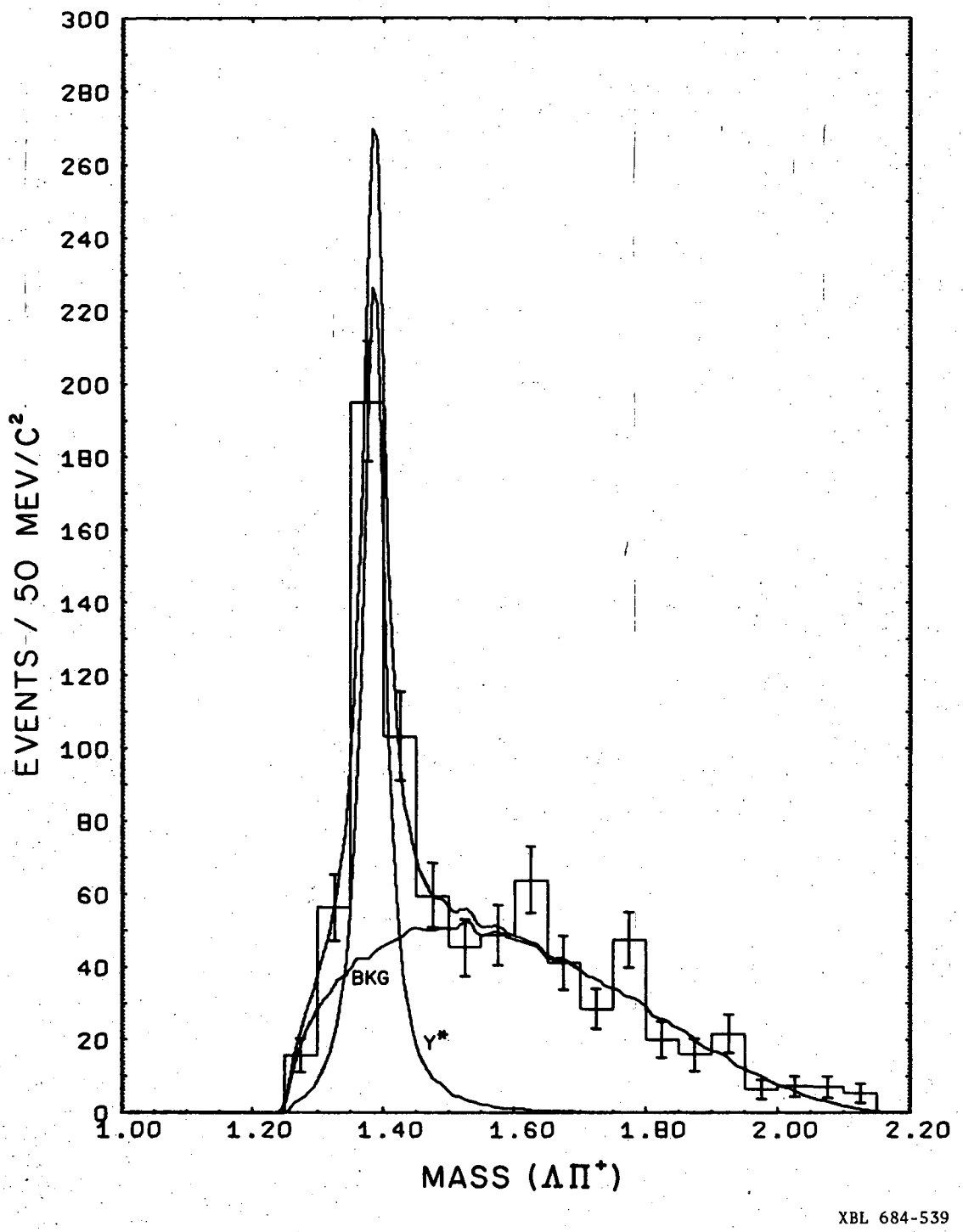


Fig. 54. Effective mass distribution of $\Lambda\pi^+$ for examples of the reaction $pp \rightarrow \Lambda n K^+ \pi^+$ (791 events). The curves are pion-exchange predictions and are described in the text.

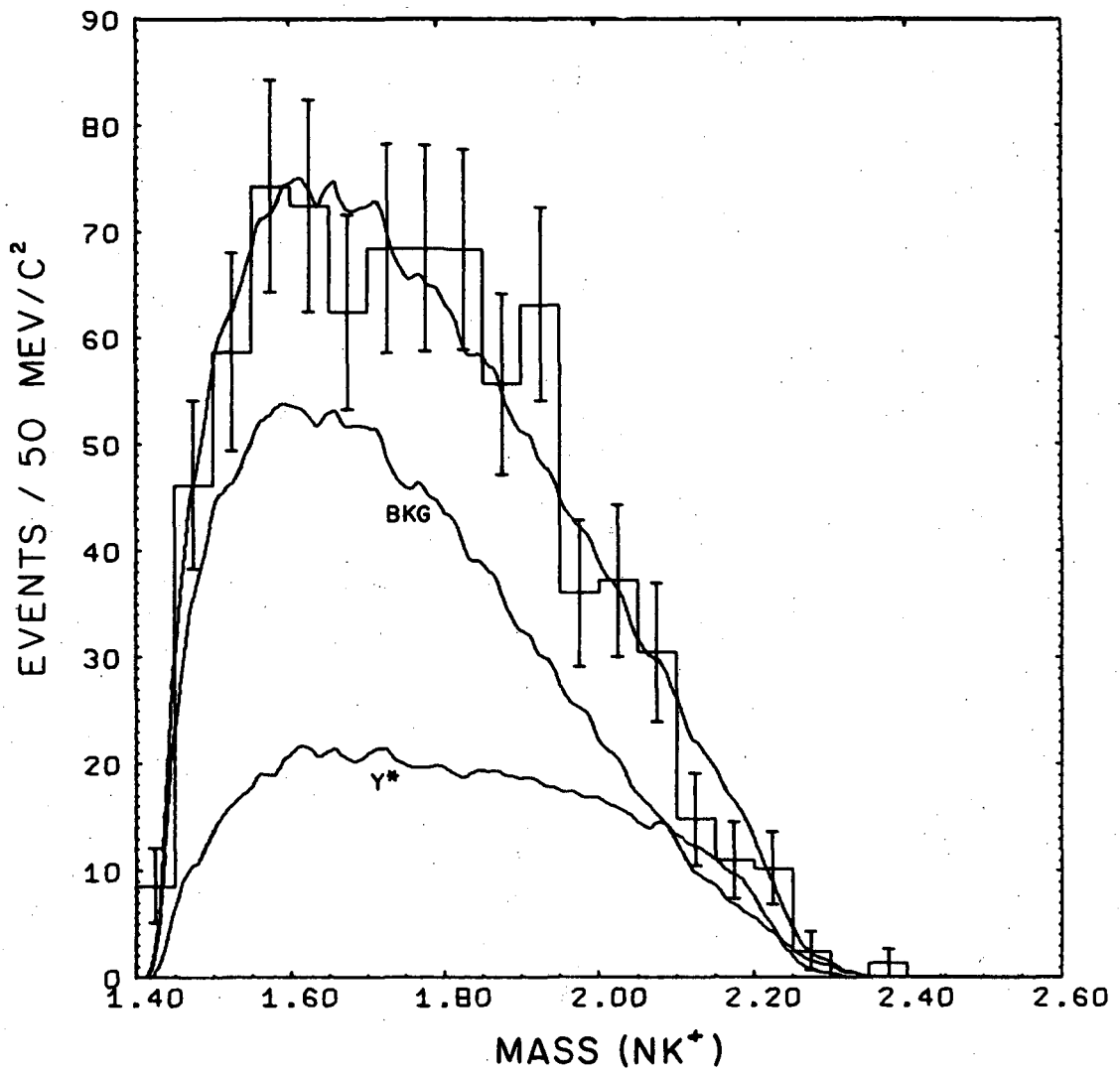


XBL 687-1437

Fig. 55. Effective mass distribution of $nK^+$ for examples of the reaction $pp \rightarrow \Lambda nK^+\pi^+$ (791 events). The curves are pion-exchange predictions and are described in the text.

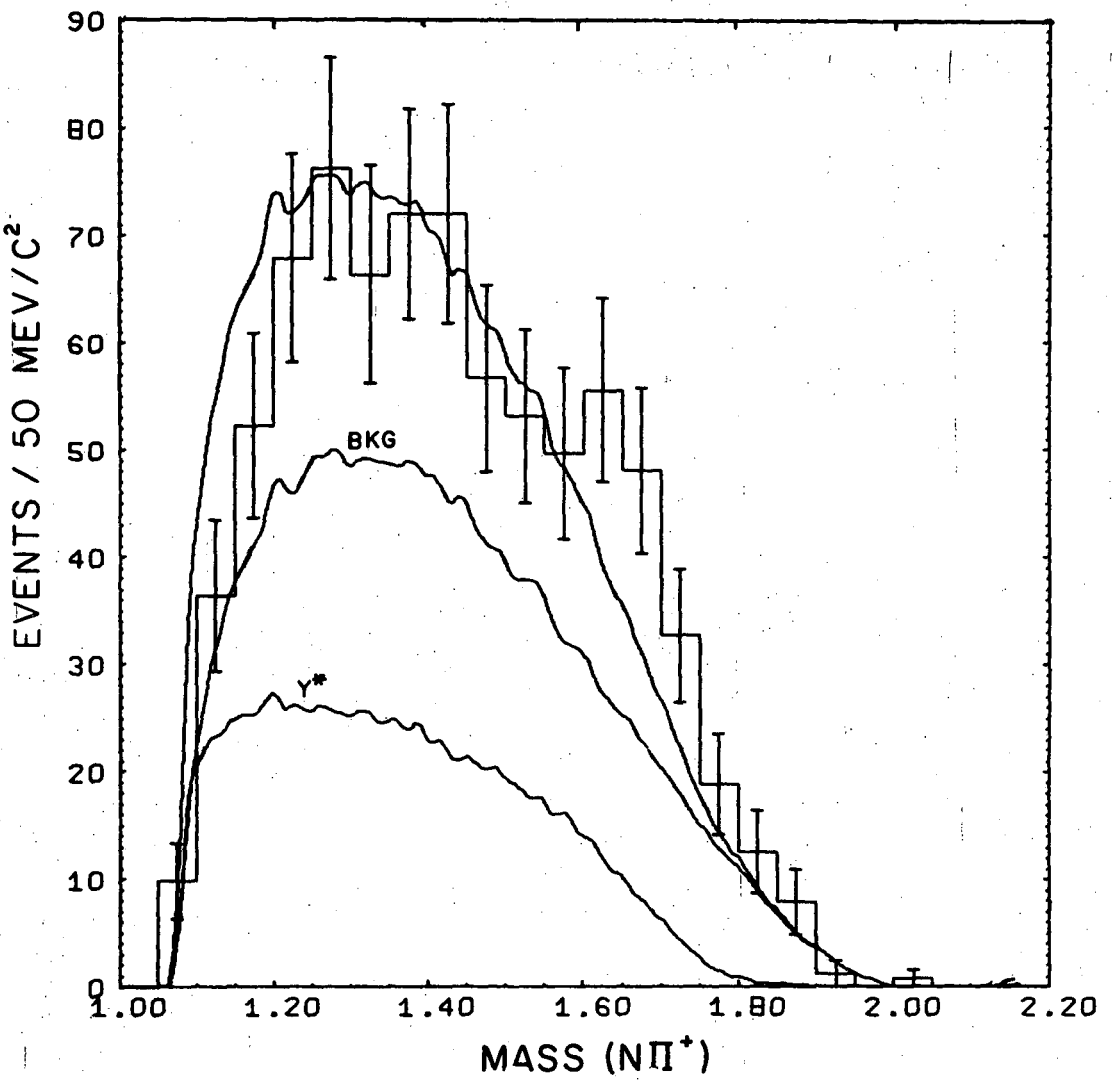


XBL 687-1438

Fig. 56. Effective mass distribution of $n\pi^+$ for examples of the reaction $pp \rightarrow \Lambda nK^+\pi^+$ (791 events). The curves are pion-exchange predictions and are described in the text.

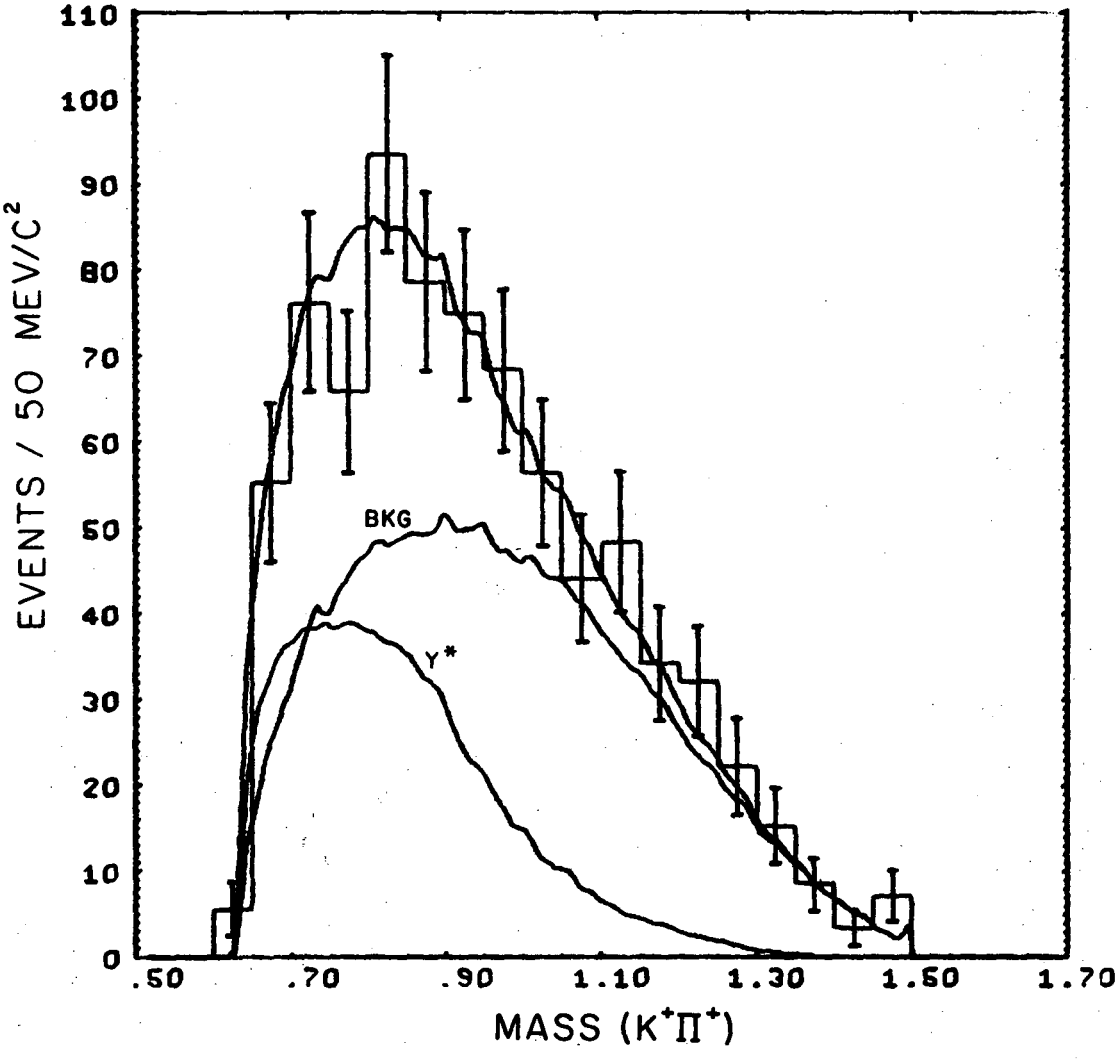


XBL 687-1439

Fig. 57. Effective mass distribution of $K^+\pi^+$ for examples of the reaction $pp \rightarrow \Lambda nK^+\pi^+$ (791 events). The curves are pion-exchange predictions and are described in the text.

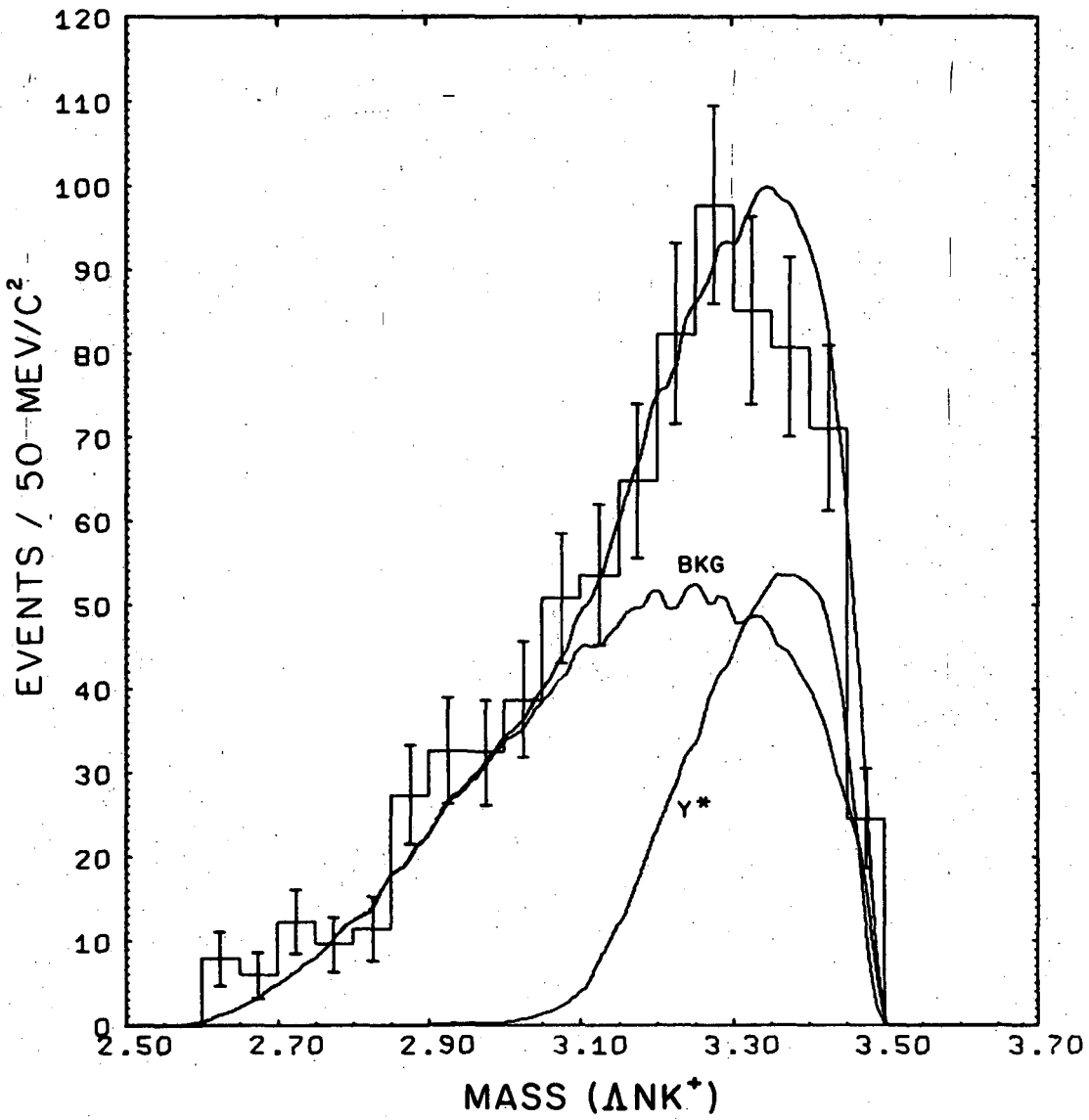


XBL 687-1440

Fig. 58. Effective mass distribution of $\Lambda nK^+$ for examples of the reaction $pp \rightarrow \Lambda nK^+\pi^+$ (791 events). The curves are pion-exchange predictions and are described in the text.

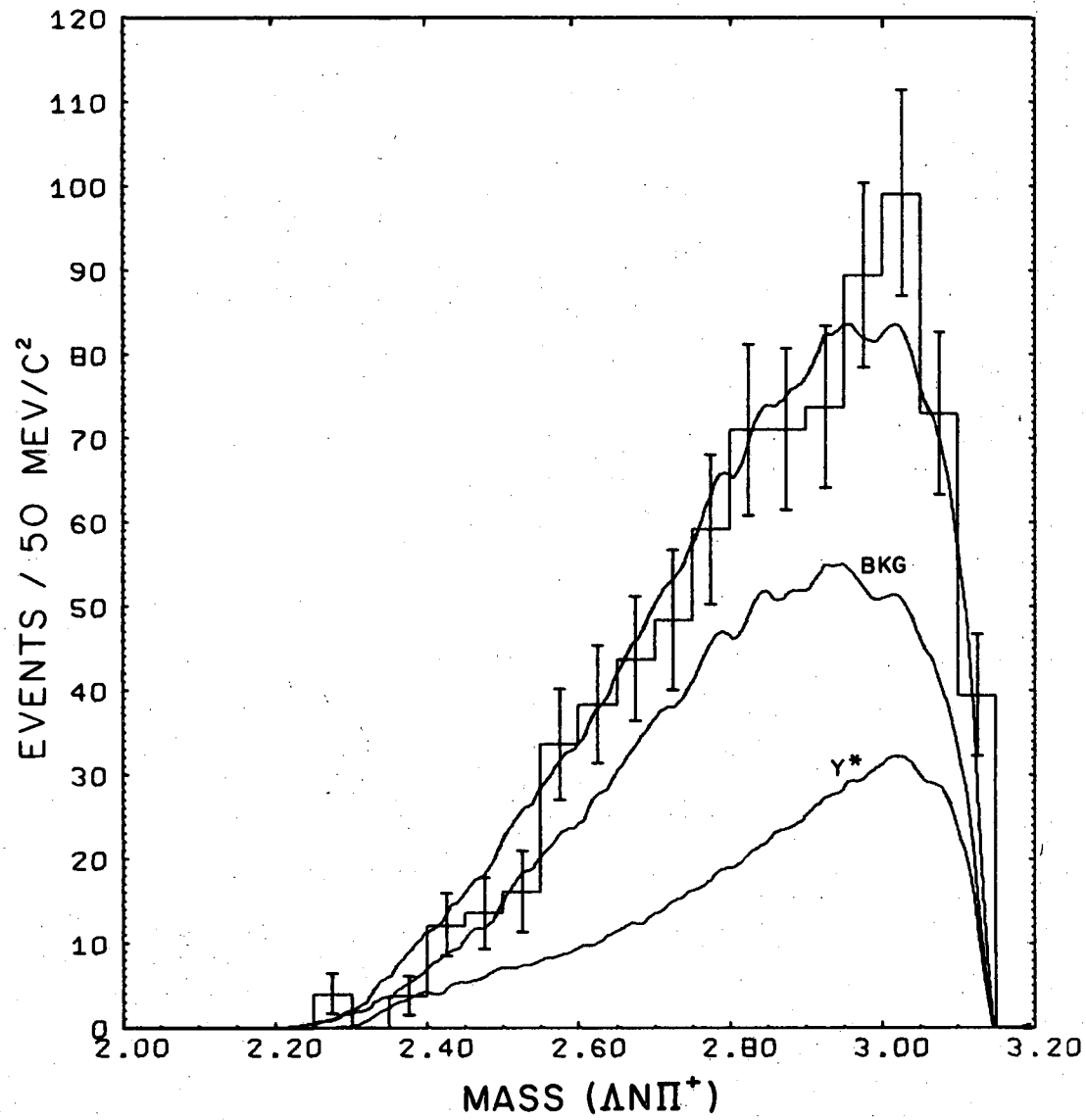


XBL 687-1441

Fig. 59. Effective mass distribution of $\Lambda n\pi^+$ for examples of the reaction $pp \rightarrow \Lambda nK^+\pi^+$ (791 events). The curves are pion-exchange predictions and are described in the text.

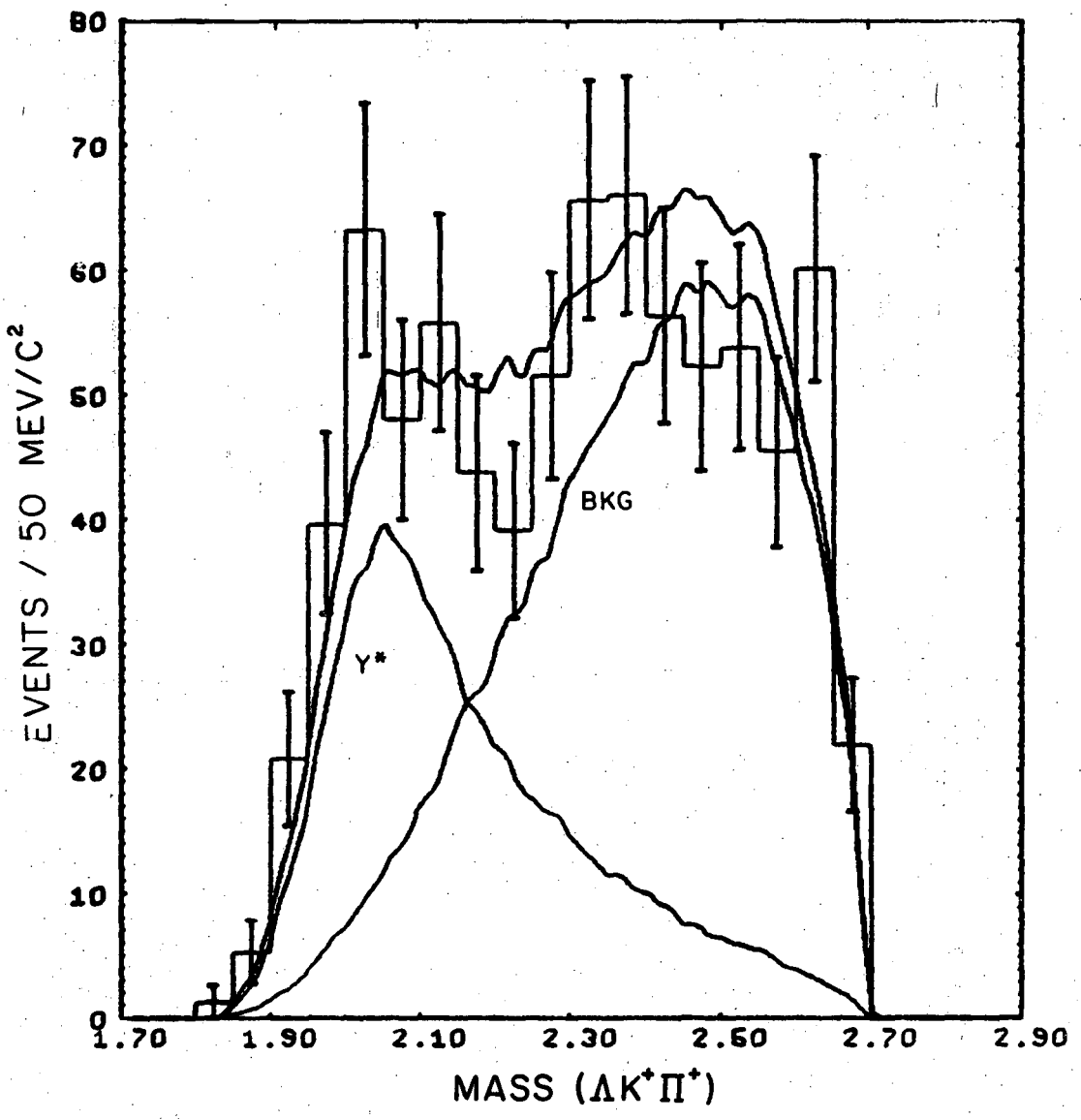


XBL 687-1442

Fig. 60. Effective mass distribution of $\Lambda K^+\pi^+$ for examples of the reaction $pp \rightarrow \Lambda nK^+\pi^+$ (791 events). The curves are pion-exchange predictions and are described in the text.

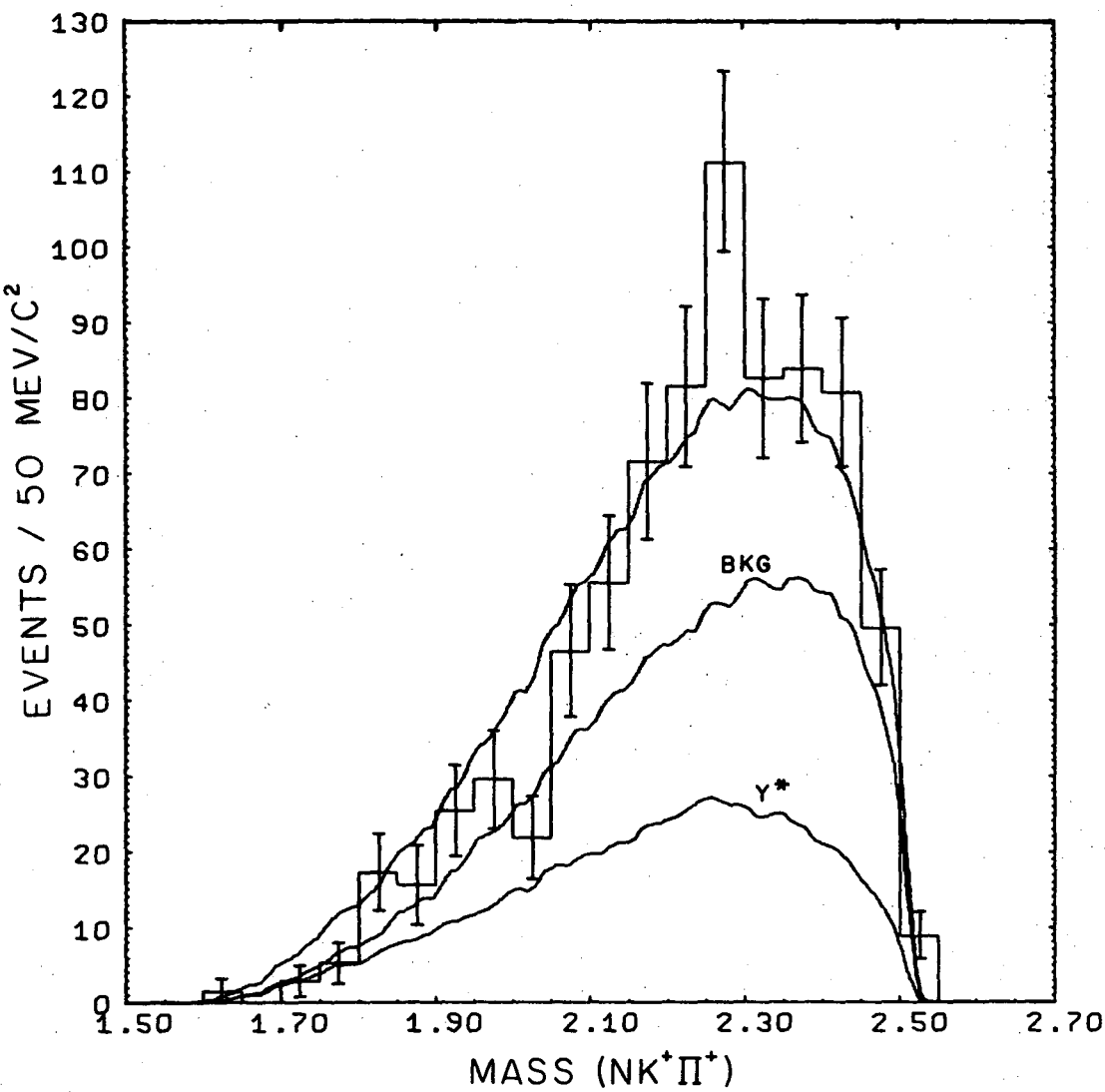


XBL 687-1443

Fig. 61. Effective mass distribution of $nK^+\pi^+$ for examples of the reaction $pp \rightarrow \Lambda nK^+\pi^+$ (791 events). The curves are pion-exchange predictions and are described in the text.

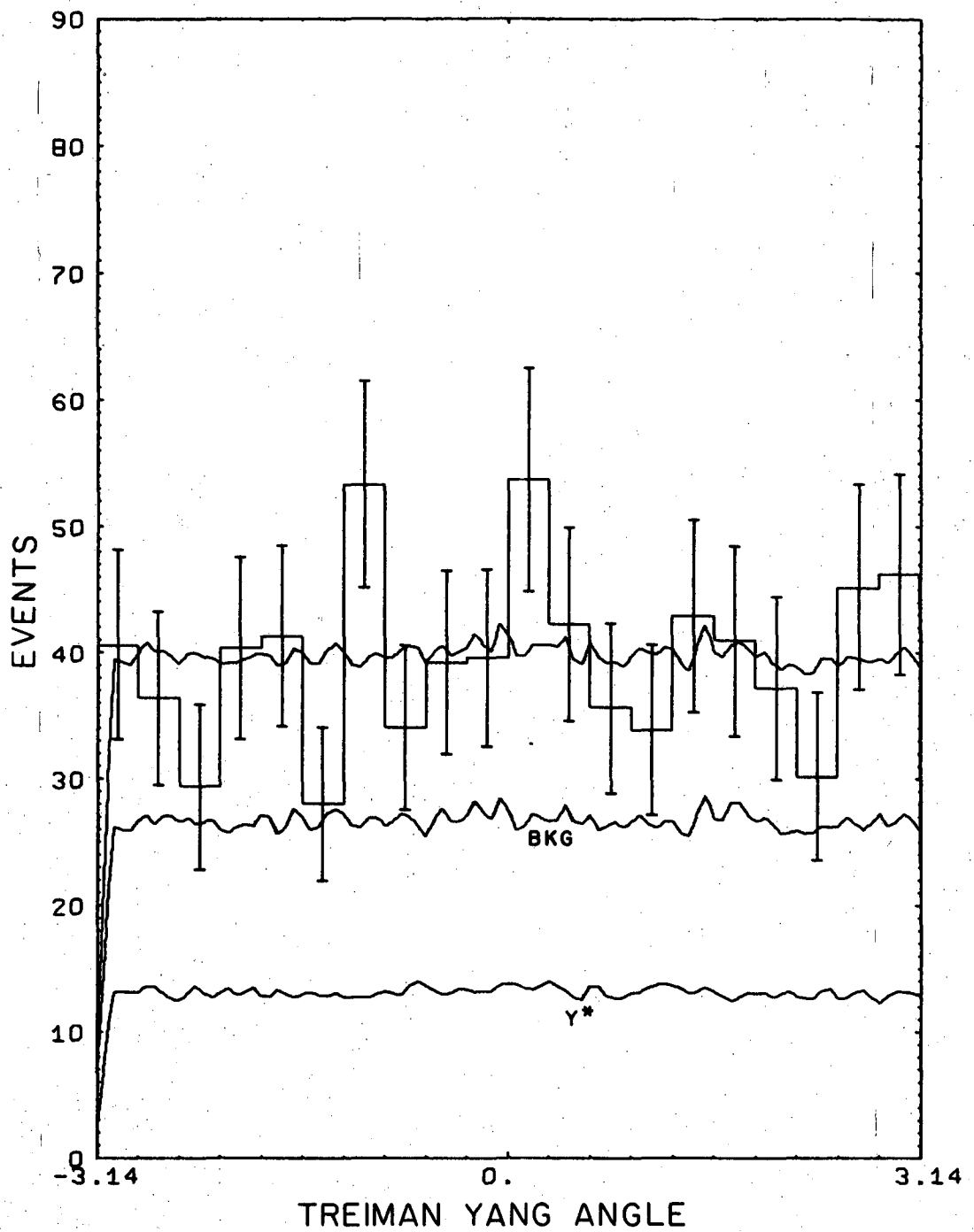


XBL 687-1448

Fig. 62. Distribution of the Treiman-Yang angle for examples of the reaction $pp \rightarrow \Lambda n K^+ \pi^+$ (791 events). The curves are pion-exchange predictions and are described in the text.

not surprising, since the input cross sections used in the calculation of the model are best known for this state and our data have little contamination. As we discussed above, the low $K^{o}\pi^{+}$ effective mass region is not fit well by the model. The fit to the $p\pi^{+}$ effective mass, shown in Fig. 29 could be improved. From other analyses in non-strange data we find the correction factors of Dürr and Pilhuhn tend to shift the resonance peak to a slightly lower value and result also in a somewhat narrower effective width for the resonance region.[39] In Figs. 35 and 36 we plot the cosines of the scattering angles in the $p\pi^{+}$ and $\Lambda K^{o}$ rest systems, respectively. These distributions indicate that the real differential cross sections we use describe the virtual scattering processes quite well. Finally, in Fig. 37, we plot the four-momentum transfer to the final state proton and it appears that our model is sufficient to fit even the large $\Delta^2$ region.

The $\Lambda pK^{+}\pi^{o}$ final state has probably the largest amount of contamination and the errors in the $\pi^{o}p \rightarrow \Lambda K^{+}\pi^{o}$ cross sections are largest here. These facts prevent us from making finer conclusions about the validity of the pion exchange model. In Fig. 49 we show the $\Delta^2$ distribution to the proton. The agreement is again rather good for all values of $\Delta^2$. The scattering angle in the $p\pi^{o}$ center of mass is shown in Fig. 50. This distribution no longer mainly represents virtual pion scattering, since most of the cross section is due to $\Lambda K\pi$ production at one vertex, but the prediction of our model for this distribution is still very good.

In the $\Lambda nK^{+}\pi^{+}$ final state only the one exchange process $\pi p \rightarrow \Lambda K\pi$ is included in the fit. All effective masses are in rather good agreement with our somewhat over simplified model for the background. In

this final state, a clean selection of Y* is possible and we find that the agreement of the data with the model persists after this selection is made. As a typical example, we display the $Y^{*+}K^{+}$ mass distribution in Fig. 63. The selection on $M(\Lambda\pi)$ is $1.35 \leq 1.42$ BeV/$c^2$. This mass distribution reflects most directly the $\pi^{+}p \rightarrow Y^{*+}K^{+}$ cross section which we have used in the pion exchange calculation. As we have discussed above, our data indicate the decay of N*(1950) in the Y*K mode; and, if our pion exchange model is correct, we expect that the $\pi^{+}p \rightarrow Y^{*+}K^{+}$ data can be explained by the existence of an s channel resonance, namely N*(1950).

A further check of single pion exchange is provided by the Treiman-Yang test. In Figs. 38, 51 and 62 we show for each final state the angle $\phi_{\Lambda\pi}$ which we briefly defined on page 52. The precise definition of this angle is

$$\sin(\phi_{\Lambda\pi}) = \frac{\vec{P}_{p1}\times(\vec{P}_{p2}\times\vec{P}_{N})}{|\vec{P}_{p1}\times(\vec{P}_{p2}\times P_{N})|} \cdot \frac{\vec{P}_{p1}\times\vec{P}_{\Lambda\pi}}{|\vec{P}_{p1}\times\vec{P}_{\Lambda\pi}|}$$

$$\cos(\phi_{\Lambda\pi}) = \frac{\vec{P}_{p2}\times\vec{P}_{N}}{|\vec{P}_{p2}\times\vec{P}_{N}|} \cdot \frac{\vec{P}_{p1}\times\vec{P}_{\Lambda\pi}}{|\vec{P}_{p1}\times\vec{P}_{\Lambda\pi}|}$$

where p1 and p2 refer to the initial state protons and N to the final state nucleon. All momenta are evaluated in the $\Lambda K\pi$ rest frame. This angle is calculated for all events in the same way and has the meaning of a Treiman-Yang angle only for events which are not N*(1236). The fact that we include the N*(1236) events in these distributions is not incorrect since the same method of calculation is applied in the Monte Carlo calculation of this angle. For the $\Lambda nK^{+}\pi^{+}$ final state, however,

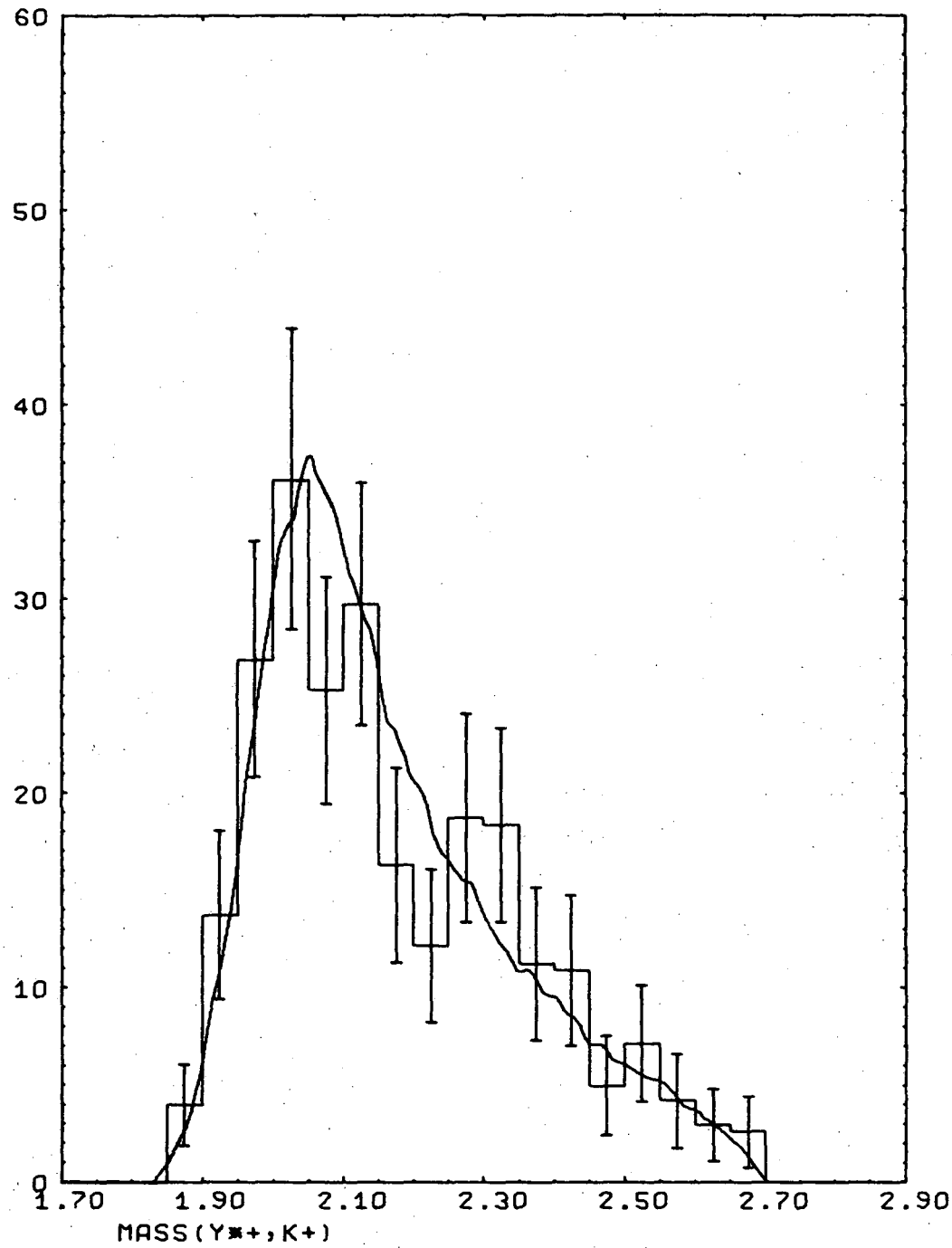


XBL 684-540

Fig. 63. Effective mass distribution of $Y^{*+}K^{+}$ for examples of reaction $pp \rightarrow Y^{*+}K^{+}n$. The curve is the pion-exchange prediction and is discussed in the text.

this angle takes on the usual meaning. All three of these distributions are consistent with spin zero exchange and this fact remains true even when selections on momentum transfer are imposed on the data.

## VI. $SU_3$ RELATIONS FOR N*(1950)

Using a model for resonance production in quasi-two-body final states and four known cross sections we are able to test various $SU_3$ predictions and make consistency checks of our interpretation of the Y*K resonance as N*(1950). In particular it is of interest to see if this interpretation implies a partial width for the $SU_3$ symmetric decay mode, N*π, that is consistent with the known elasticity of N*(1950). The $I_z=3/2$ state of N*π is not observable in this experiment because there are necessarily two neutral particles in the final state. Therefore, we use $SU_3$ symmetry in estimating the partial width for this mode.

From strict $SU_3$ symmetry we have

$$\frac{G^2(N^*\pi)^{++}}{G^2 Y^{*+}K^+} = 2.5 \quad .$$

With this ratio of the couplings and the measured Y*K cross section, we apply the resonance model discussed in detail in Section IV B to predict a value for the cross section $pp \to nN^{*++}(1950)$, $N^{*++}(1950) \to (N^*\pi)^{++}$

$$\sigma_{1950}(nN^*\pi) = 170 \pm 40 \ \mu b \ .$$

This value seems to be consistent with our earlier assumption that N*π is the major inelastic decay mode.

The reported cross sections for the production of $N^{*++}(1950)$ and decay into $p\pi^+$ are $320 \pm 160$ μb[11] and $520 \pm 260$ μb.[40] From the reported elasticity of N*(1950)[32,33] we have a relation between the sum of all inelastic widths and the elastic width at resonance:

$$\frac{\Gamma_{N^*\pi}(m_o)+\Gamma_{n\rho}(m_o)+\Gamma_{n\pi\pi}(m_o)+\Gamma_{\Sigma K}(m_o)+\ldots}{\Gamma_{\pi p}(m_o)} = 1.0 \pm 0.3 \quad .$$

Here, the error estimate is based on the difference between the values published in the two reports.

The ratio of cross sections for decay into different modes are related to the corresponding partial widths viz

$$\frac{\Gamma_\alpha(m_o)}{\Gamma_\beta(m_o)} = \frac{d\sigma_\alpha(m_o)}{d\sigma_\beta(m_o)}$$

where $d\sigma_\alpha(m_o)$ represents the most differential cross section for production of the resonance and decay into mode $\alpha$. We assume that this exact relation remains true if we use our model to describe the production and use integrated cross sections. For our model, this last assumption is a good approximation if the thresholds for $\alpha$ and $\beta$ are fairly close together. We find

$$\frac{\Gamma_{(N^*\pi)^{++}}(m_o)}{\Gamma_{\pi^+p}(m_o)} \simeq \frac{170\pm40}{420\pm210} = 0.4 \pm 0.2 \quad .$$

Thus, it is clear that the cross sections are consistent with the requirements of $SU_3$ with the reasonable assumption that such modes as $N\pi\pi$ and $N\rho$ have partial width comparable to $N^*(1236)\pi$.

The cross section for $\Sigma^+K^+$ decay has also been studied in this experiment and is reported to be $22\pm4$ $\mu$b.[22] The $SU_3$ relation

$$\frac{G^2_{\Sigma^+K^+}}{G^2_{p\pi^+}} = 1$$

and analysis identical to that just described for $N^*\pi$ predicts a ratio of cross sections

$$\frac{\sigma(np\pi^+)}{\sigma(n\Sigma^+K^+)} = 2.5$$

which is in disagreement with the measured cross sections. It is not possible to decide whether this is a result of broken $SU_3$ symmetry or an inadequacy of our model for the production and decay of the resonance. Of course, the best way to study such questions about branching ratios of the resonance would be in $\pi^+ p$ experiments where formation of the resonance in the s channel would eliminate the problems of final state interactions and the dynamical mechanisms would be more easily analyzed.

# VII. CONCLUSIONS

Four-body starange particle production of $\Lambda NK\pi$ is generally well described by one-pion exchange. Resonance production is dominant in these reactions and the pseudo-two-body reaction $pp \rightarrow nN^{*++}(1950)$, $N^{*++}(1950) \rightarrow Y^{*+}K^{+}$ is also explained by this mechanism.

ACKNOWLEDGMENTS

I express my deepest thanks to Professor William Chinowsky for his most valued advice and encouragement.

I am grateful to Professor Jonas Schultz for his interest in this work and I thank him heartily.

I am grateful to Professor Paul Condon and Professor Peter Schmidt for many valuable discussions.

I am grateful to Professor Emilio Segrè for his support of the experiment.

I thank Dr. Robert Kinsey and Professor Mark Mandelkern for their work on this experiment. I thank Professor Martin Perl and Dr. Tai Ho Tan and the other people at SLAC who worked on this experiment.

I especially thank Mr. William Gage for his expert programming ability and his willingness to help me.

I thank Mr. Bruce Douglass and Mrs. Judy Conklin for their help in the programming and bookkeeping for the experiment.

My thanks go to the many scanners and measurers who contributed to the experiment.

I thank Mrs. Rosemary Fowell for her help in typing this thesis.

# APPENDICES

## A. Neutral $V^o$ Detection Biases and Corrections

All examples of the three reactions analyzed in the text are required to have at least one visible $V^o$ decay in order to fit them. Three separate effects are found to be responsible for reduction of the total sample to that observed in the experiment: 1) Inability to detect neutral $V^o$ decays close to the production vertex; 2) Finite size of the bubble chamber and 3) Misidentitification of $\Lambda$'s as electron pairs. Evidences for the first and third of these biases are found in the lifetime and decay angular distributions of the neutral $V^o$'s and are discussed in the text. The second effect is obviously present and is easily corrected for simultaneously with the first. We discuss the corrections for these effects below.

In order to suitably correct for an inefficiency we must have for a given momentum of the $V^o$ that at least some of the events fall outside the inefficient region and that we be able to calculate the probability that such an event could have occurred in the biased region. Each event then in the deficient region is thrown out and the remaining events are weighted according to this probability. To determine the boundary of such a region the behavior of the total weight is observed as the boundary is varied. As the cuts are made more exclusive, the weight will continue to increase until the proper value for the cut is reached, after which point the weight remains constant. It is important to notice that the parameter whose distribution manifests the assumed bias is related to the parameter in which the cut is made but is usually not identical to it. For example, it is the time distribution of the $\Lambda$ which we understand and

find to be depleted while it is the length of the neutral track that we believe to be responsible. Hence, it is in the length that the cut is made.

Length Correction

We first describe the correction for a visible $V^o$. Let $\ell_{min}$ be the minimum length cut off and $\ell_{max}$ the length measured from the production vertex along the neutral track to the boundary of the fiducial volume. For an unstable particle of mass $m_o$, lifetime $\tau_o$, and momentum p, the probability $\eta$ of the decay occurring between $\ell_{min}$ and $\ell_{max}$ is

$$\eta = e^{\frac{-\ell_{min} m_o}{pc\ \tau_o}} - e^{\frac{-\ell_{max} m_o}{pc\ \tau_o}} .$$

Hence, each event with a visible $V^o$ decay is weighted by $1/\eta$. The sum of these weights is then the true number of $V^o$'s which decayed in the charged mode.

Examples of the reaction $pp \rightarrow \Lambda K^o p\pi^+$ can be fitted if at least one of the strange particle decays is visible. Besides the weight described above for the visible $V^o$, an additional correction for the unobserved decay is necessary. The reason for this is that all decays in the charged mode which occurred outside the fiducial volume are included in the sample. Since we have already corrected the visible $V^o$'s for all charged decays, we want now to correct only for the total number of neutral mode decays. Let a be the probability that a $V^o$ decay charged inside the fiducial volume, b the probability of charged decay outside, c the probability of neutral decay inside and d the probability of neutral decay outside. We have

$$a = \left(1 - e^{\frac{-\ell_{max} m_o}{pc\,\tau_o}}\right) \cdot (1 - R)$$

$$b = \left(e^{\frac{-\ell_{max} m_o}{pc\,\tau_o}}\right) \cdot (1 - R)$$

$$c = \left(1 - e^{\frac{-\ell_{max} m_o}{pc\,\tau_o}}\right) \cdot R$$

$$d = \left(e^{\frac{-\ell_{max} m_o}{pc\,\tau_o}}\right) \cdot R$$

where R is the branching ratio of uncharged to total. In addition to c and d, b also contributes to the topology of the missing neutral. Hence, if we want only to correct for the uncharged decay mode, we must weight each unobserved neutral by:

$$\frac{c + d}{b + c + d} = \frac{1}{1 + \frac{(1-R)}{R} e^{\frac{-\ell_{max} m_o}{pc\,t_o}}}$$

Since the $\Lambda$ and $K^o$ decay independently of each other, the weight for an event is the product of the individual weights for each strange particle.

Projected Opening Angle Correction

We have generated a large number of Monte Carlo events for $\Lambda$ decay into $p\pi^+$. After Lorentz transformation to the laboratory, we impose cuts on the projected opening angle. Over a 3.0 BeV/c range in $\Lambda$ laboratory momentum and for projected opening angle cuts varying from 1 to 6 degrees the following expression for the efficiency is accurate to within 1 percent.

$$E = 1 - 0.00125\ \alpha - (0.00166 + \alpha/48)P_\Lambda$$

where $P_\Lambda$ is in BeV/c

$\alpha$ is the projected opening angle in degrees .

B. Monte Carlo Generation of Events

Generally speaking, Monte Carlo methods are useful for simultaneous evaluations of several multi-dimensional integrals of some positive definite density function defined over a multi-dimensional space. In high energy physics this density function is typically the most elemental differential cross section for some reaction. There are two distinct Monte Carlo methods and which one is preferable depends upon the specific functions and the number of variables involved. In the first method, which we have chosen not to use, the variables are picked at random between their absolute minimum and absolute maximum values. If these values are all physical, the cross section is evaluated for this set of variables and then a random number is picked between 0 and the absolute maximum value of the cross section. If this random number is less than the value of the cross section this set of variables is kept, otherwise a new selection is begun. This method is obviously wasteful if the cross section varies significantly in any of the variables and/or if the physical volume of the multi-dimensional space is a small fraction of the circumscribed volume used in the selection of the variables. However, this method does give a distribution of points in the multi-dimensional space which has the same statistical properties as a distribution given us by nature (provided nature is described by the model). For this reason, one often refers to the selected set of variables as an "event", although this nomenclature is often extended to the Monte Carlo method which we now describe in detail.

As in the method above, an event is generated by randomly selecting values for each of the variables which describe the problem. The value for each variable is chosen between a minimum and a maximum value consist-

ent with the "kinematic" boundaries of the multi-dimensional space. These minimum and maximum values will usually be themselves functions of the subset of variables which have already been chosen for a particular event, except of course for the variable chosen first. The order in which the variables are chosen is important only from a statistical point of view, i.e. for large numbers of events, the results do not depend on the order of the selection, although intelligent ordering can reduce computer time for a given degree of random fluctuation in the results. We assign to each event a weight which is the product of two quantities--one being the value of the cross section at the corresponding point in the multi-dimensional space, the other the volume over which the selection was performed in the space. The reason for these factors should be clear from the following.

Let $a_i$ and $b_i$ be the minimum and maximum values respectively for the variables $q_i$ used to define a particular event. Let $N_o$ be the number of events generated as described above. Clearly the generated population of events at a point in the $q_i$ space will be given by

$$\frac{d^m N''}{dq_1 \cdot\cdot dq_m}(q_1,\cdot\cdot q_m) = \frac{N_o}{(b_1-a_1)(b_2(q_1)-a_2(q_1))\cdot\cdot(b_m(q_1,\cdot\cdot q_{m-1})-a_m(q_1,\cdot\cdot q_{m-1}))} .$$

Hence, we include in the weight the products $\Pi_i(b_i-a_i)$ to simply cancel this effect introduced by the random selection of the variables. Using only this weight for each event would give a distribution in weights (numbers of events) that would be constant over the whole multi-dimensional space. Specifically we would then have

$$\frac{d^m N'}{dq_1 \cdot\cdot dq_m} = N_o$$

where $N_o$ is the total number of events generated. The inclusion of the cross section in the weight is obvious now. This is the way in which we introduce the dynamics to give:

$$\frac{d^m N}{dq_1 .. dq_m} = N_o \frac{d^m \sigma}{dq_1 .. dq_m} \quad .$$

By dividing the weights all by $N_o$, we can make the number distribution numerically equal to the elemental cross section. Now we see that to calculate any distribution of interest we may treat the Monte Carlo events exactly like real events, since they have the same properties as real weighted events. Also, we may exclude arbitrary regions in the multi-dimensional space easily with the Monte Carlo method to compare with real events selected in the same way. Although this method does not throw out any events, one should avoid generating large numbers of events in regions where the cross section is smallest and few events in the regions where the cross section is largest. Also, an ideal situation would be to select a set of variables which makes the cross section most nearly constant over all of the multi-demensional space. We explain the Breit-Wigner function as an example.

In reactions involving resonance production one usually has a cross section of the form

$$\frac{d^m \sigma}{dm^2_{ab} dq_2 .. dq_m} = \frac{1}{(m^2_{ab} - m_o^2)^2 + m_o^2 \Gamma_o^2} F(m^2_{ab}, q_2, .. q_m) \quad .$$

Clearly using $m^2_{ab}$ as one of the variables would be very inefficient since the cross section varies rapidly over the kinematic region. We define

$$z(m^2_{ab}) = \int_{(m_a+m_b)^2}^{m^2_{ab}} \frac{1}{(X-m_o^2)^2 + m_o^2\Gamma_o^2}\, dX ,$$

so that

$$\frac{dz}{dm^2_{ab}} = \frac{1}{(m^2_{ab}-m_o^2)^2 + m_o^2\Gamma_o^2} .$$

Now we rewrite our formula for the cross section in terms of z.

$$\frac{d^m\sigma}{dm^2_{ab}dq_2..dq_m} = \frac{d^m\sigma}{dzdq_2..dq_m}\frac{dz}{dm^2_{ab}} .$$

But

$$\frac{d^m\sigma}{dzdq_2..dq_m}\frac{dz}{dm^2_{ab}} = \frac{dz}{dm^2_{ab}} F(m^2_{ab}(z),q_2,..q_m)$$

Hence,

$$\frac{d^m\sigma}{dzdq_2..dq_m} = F(m^2_{ab}(z),q_2,..q_m)$$

In this way, we have eliminated the rapid variation of the cross section. We must be able to solve for $m^2_{ab}$ given z since this is the variable in which F is expressed. Fortunately, this too is easy since

$$z = \frac{1}{m_o\Gamma_o}\left[\text{ARCTAN}\left(\frac{m^2_{ab}-m_o^2}{m_o\Gamma_o}\right) - \text{ARCTAN}\left(\frac{(m_a+m_b)^2-m_o^2}{m_o\Gamma_o}\right)\right]$$

and this equation can be easily rearranged to give $m^2_{ab}$ as a function of z. If one randomly selects z as the first of the m variables to describe the problem, the maximum value of z need only be calculated once since it will be the same for all events. (The lower value is clearly zero.)

We summarize the conditions necessary for such a change of variable as we have just discussed:

1. The cross section has some dependence on a variable which is rapidly varying.
2. The integral of the rapidly varying part of the cross section can be evaluated.
3. Given the value for the integral, the corresponding value of the parameter in which the cross section is expressed must be easily evaluated.

Some other examples of functions which occur in cross sections and have the above properties are power, log, and exponential functions.

REFERENCES AND FOOTNOTES

1. K. J. Foley, R. S. Jones, S. J. Lindenbaum, W. A. Love, S. Ozaki, E. D. Platner, C. A. Quarles, and E. H. Willen, Phys. Rev. Letters 19, 397 (1967).

2. I. M. Blair, A. E. Taylor, W. S. Chapman, P. I. P. Kalmus, J. Litt, M. C. Miller, D. B. Scott, H. J. Sherman, A. Astbury, and T. J. Walker, Phys. Rev. Letters 17, 789 (1966).

3. E. W. Anderson, E. J. Bleser, G. B. Collins, T. Fujii, J. Menes, F. Turkot, R. A. Carrigan, Jr., R. M. Edelstein, N. C. Hien, T. J. McMahon, and I. Nadelhaft, Phys. Rev. Letters 16, 855 (1966).

4. C. M. Ankenbrandt, A. R. Clyde, B. Cork, D. Keefe, L. T. Kerth, W. M. Layson, and W. A. Wenzel, Nuovo Cimento 35, 1052 (1965).

5. G. Cocconi, E. Lillethun, J. P. Scanlon, C. A. Stahlbrandt, C. C. Ting, J. Walters, and A. M. Wetherell, Phys. Letters 8, 134 (1964).

6. D. V. Bugg, A. J. Oxley, J. A. Zoll, J. G. Rushbrooke, V. E. Barnes, J. B. Kinson, W. P. Dodd, G. A. Doran, and L. Riddiford, Phys. Rev. 133, B1017 (1964).

7. G. G. Chadwick, G. B. Collins, P. J. Duke, T. Fujii, N. C. Hien, M. A. R. Kemp, and F. Turkot, Phys. Rev. 128, 1823 (1962).

8. G. Cocconi, A. N. Diddens, E. Lillethun, G. Manning, A. E. Taylor, T. G. Walker, and A. M. Wetherell, Phys. Rev. Letters 7, 450 (1961).

9. G. B. Chadwick, G. B. Collins, C. E. Swartz, A. Roberts, S. DeBenedetti, N. C. Hien, and P. J. Kuke, Phys. Rev. Letters 4, 611 (1960).

10. A. P. Colleraine and U. Nauenberg, Phys. Rev. 161, 1387 (1967).

11. G. Alexander, O. Benary, G. Czapek, B. Haber, N. Kidron, B. Reuter,

A. Shapira, E. Simopoulou, and G. Yekutieli, Phys. Rev. 154, 1284 (1967).

12. S. Coletti, J. Kidd, L. Mandelli, V. Pelosi, S. Ratti, V. Russo, L. Tallone, E. Zampieri, C. Caso, F. Conte, M. Dameri, C. Grosso, and G. Tomasini, Nuovo Cimento 49A, 479 (1967).

13. A. M. Eisner, E. L. Hart, R. I. Louttit, and T. W. Morris, Phys. Rev. 138, B670 (1965).

14. G. Alexander, O. Benary, B. Haber, N. Kidron, A. Shapira, G. Yekutieli, and E. Gotsman, Nuovo Cimento 40A, 839 (1965).

15. E. L. Hart, R. I. Louttit, D. Luers, T. W. Morris, W. J. Willis, S. S. Yamamoto, Phys. Rev. 126, 747 (1962).

16. W. J. Fickinger, E. Pickup, D. K. Robinson, and E. O. Salant, Phys. Rev. 125, 2082 (1962).

17. E. Pickup, D. K. Robinson, and E. O. Salant, Phys. Rev. 125, 2091 (1962).

18. G. A. Smith, H. Courant, E. C. Fowler, H. Kraybill, J. Sandweiss, and H. Taft, Phys. Rev. 123, 2160 (1961).

19. Robert Ronald Kinsey, "Zero Strangeness Resonance Production in 6 GeV/c Proton-Proton Collisions," (Ph.D. Thesis), University of California Lawrence Radiation Laboratory Report UCRL-17707, March 1968.

20. G. Wolf, Phys. Rev. Letters 19, 925 (1967).

21. G. Alexander, A. Shapira, E. Simopoulou, and G. Yekutieli, Nuovo Cimento 53A, 455 (Jan. 1968).

22. W. Chinowsky, R. R. Kinsey, S. L. Klein, M. Mandelkern, J. Schultz,

F. Martin, M. L. Perl, and T. H. Tan, Phys. Rev. 165, 1466 (1968).

23. E. Bierman, A. P. Colleraine, and V. Nauenberg, Phys. Rev. 147, 922 (1966).

24. W. M. Dunwoodie, H. K. Ticho, G. A. Smith, and A. B. Wicklund, UCLA-1031.

25. G. Ascoli, M. Firebaugh, E. L. Goldwasser, U. E. Kruse, and R. D. Sard, COO-1195-75.

26. T. Yao, Phys. Rev. 125, 1048 (1962).

27. A. R. Clyde (Ph.D. Thesis) UCRL 16275.

28. R. F. George, K. F. Riley, R. J. Tapper, D. V. Bugg, D. C. Salter, and G. H. Stafford, Phys. Rev. Letters 15, 214 (1965).

29. P. Nyborg, H. S. Song, W. Kernan, and R. H. Good, Jr., Phys. Rev. 140, B914 (1965).

30. The sample of events used for the analysis in this section only represent 80% of the final sample.

31. S. L. Glashow and A. H. Rosenfeld, Phys. Rev. Letters 10, 192 (1963).

32. A. Donnachie, R. G. Kirsopp, and C. Lovelace, Phys. Letters 26B, 161 (1968).

33. P. Bareyre, C. Bricman, and G. Villet, Phys. Rev. 165, 1730 (1968).

34. A. H. Rosenfeld, N. Barash-Schmidt, A. Barbaro-Galtieri, L. R. Price, M. Roos, P. Söding, W. J. Willis, and C. G. Wohl, UCRL-8030 Rev., and to be published in Rev. Mod. Phys. (1968).

35. F. Salzman and G. Salzman, Phys. Rev. 121, 1541 (1961).

36. L. Bertanza, P. L. Connolly, B. B. Culwick, F. R. Eisler, T. Morris, R. Palmer, A. Prodell, and N. P. Samios, Phys. Rev. Letters 8, 332

(1962); J. Keren, Phys. Rev. 133, B457 (1964); J. A. Anderson, Ph.D. thesis University of California Radiation Laboratory Report No. UCRL-10838 (unpublished); F. Eisler, R. Plano, A. Prodell, N. Samios, M. Schwartz, J. Steinberger, P. Bassi, V. Borelli, G. Puppi, G. Tanaka, P. Woloscjek, V. Zobolli, M. Conversi, P. Franzini, I. Mannelli, R. Santangelo, and V. Silvestrini, Phys. Rev. 108, 1353 (1957); O. I. Dahl, L. M. Hardy, R. I Hess, J. Kirz, D. H. Miller, and J. A. Schwartz, ibid. 163, 1430 (1967).

37. O. I. Dahl, L. M. Hardy, R. I. Hess, J. Kirz and D. H. Miller, Phys. Rev. 163, 1377 (1967).

38. S. Dagan, Z. Ming Ma, J. W. Chapman, L. R. Fortney, and E. C. Fowler, Phys. Rev. 161, 1384 (1967); S. S. Yamamoto, L. Bertanza, G. C. Moneti, D. C. Rahm, and I. O. Skillicorn, Phys. Rev. 134B, B383 (1964); D. Berley and N. Gelfand, Phys. Rev. 139B, B1097 (1965); J. Bartsch, et. al., Aachen, Hamburg, London, Munchen collaboration, Nuovo Cimento 43, A1010 (1966).

39. P. Schmidt (private communication).

40. This cross section is a preliminary value based on our current analysis of the $np\pi^+$ final state in 6 BeV/c pp interactions.